THE INTERPLAY BETWEEN THE CENTRAL ENGINE AND THE CIRCUMNUCLEAR ENVIRONMENT IN COMPTON-THIN AGN

by

Sulov Chalise

A dissertation submitted in partial fulfillment
of the requirements for the degree

of

Doctor of Philosophy

in

Physics

MONTANA STATE UNIVERSITY
Bozeman, Montana

July 2022

ACKNOWLEDGEMENTS

I would like to thank my parents, Bishnu and Usha, and brother, Saurav, for their love and support throughout my graduate studies. Further, I would like to thank my mentor, Dr. Anne M. Lohfink, for introducing me to the world of Astronomy, being patient, and providing me with all the necessary tools. I would also like to thank my other committee members, Dr. Amy Reines, Dr. David Nidever, Dr. Bennett Link, and Dr. Dana Longcope. Last but not least, my thanks go out to the Physics Department, especially Margaret Jarrett, for their tremendous help and unwavering support.

TABLE OF CONTENTS

TABLE OF CONTENTS – CONTINUED

TABLE OF CONTENTS – CONTINUED

LIST OF TABLES

LIST OF FIGURES

LIST OF FIGURES – CONTINUED

Figure Page

LIST OF FIGURES – CONTINUED

Figure Page

LIST OF FIGURES – CONTINUED

Figure Page

ABSTRACT

All massive galaxies harbor a supermassive black hole (SMBH) at their galactic center. If these SMBH are actively feeding then they are called Active galactic nuclei (AGN). Their accretion system contains a corona, an accretion disk and an axisymmetric dusty torus. The torus can be connected physically and dynamically to the circumnuclear disk of the galaxy which acts as a molecular gas reservoir for material to be accreted onto the SMBH. Further, AGN can emit radiation from radio upto the gamma rays. The AGN accretion disk emits photons mostly in the optical/UV band which are Compton up-scattered in the corona to generate X-rays. If present, a jet can produce additional high-energy and Synchrotron emission. In some AGN, a huge amount of material can be stripped away from the accretion disk creating an outflowing wind. These —radiation pressure, jet, wind etc.—inject energy back into the host galaxy, regulating the SMBH growth. There exist a complex interplay between the AGN feeding and feedback. Understanding this interaction between the central engine and its circumnuclear environment is vital in context of galaxy evolution. My work aims to study this interaction in low to moderately obscured (or Compton-thin) AGN using their broadband multi-epoch X-ray spectra plus other emission bands whenever appropriate. From the spectral analysis of broad-line radio galaxy 3C 109, I was able to constrain its high-energy cutoff for the first time. In another Seyfert galaxy Mrk 926, I was able to explore the origin of its soft excess, and found that a warm coronal origin was slightly preferred. Finally, I performed a joint multi-wavelength analysis with a physical torus model of a sample of Polar-scattered Seyfert 1 galaxies. I utilized their multi-epoch broadband X-ray spectra along with their infrared spectral/photometric data, and was able to constrain their torus properties. Despite being a sample of similar moderately-inclined Compton-thin AGN, I found a complex and varied distribution of gas and dust in their torus.

CHAPTER ONE

INTRODUCTION

Super massive black holes (SMBHs) are black holes with mass ranging between 10^6 and 10^{10} solar masses (Koss et al., 2017; Lauer et al., 2007). SMBH are expected to be present at the center of all massive galaxies (Kormendy & Richstone, 1995; Richstone et al., 1998) , and have also been found in some dwarf galaxies (Hickox et al., 2022; Seth et al., 2014) in the Local Universe. When the SMBHs are actively accreting matter, the nuclei of the host galaxies become highly luminous in wavelengths ranging from radio to γ-rays. These galaxies are known as 'active galaxies' and the nuclei as 'Active Galactic Nuclei' (AGN). Observed luminosity variability on time scales of years or even less implies that AGN are spatially compact (Fabian, 1999). AGN luminosities range from 10^{40} ergs s^{-1} for nearby galaxies to more than 10^{47} ergs s^{-1} for distant quasars (Merloni & Heinz, 2013). Given the high luminosity and relatively small size of AGN, we are certain that black hole accretion is the power source of AGN (Netzer, 2015). Thus, AGN are governed by high energy physics and extreme gravity which makes them intriguing sources to study.

Furthermore, a close interplay between the evolution of SMBHs and that of the host galaxies exists (Croton, 2006; Granato et al., 2004; Menci et al., 2008). Moreover, there is a correlation between the mass of the black holes and the properties (luminosity, stellar mass, velocity dispersion, the bulge rotational velocity, etc.) of their host galaxies (Gebhardt et al., 2000; Graham & Driver, 2007; Kormendy & Ho, 2013; Marconi & Hunt, 2003). About 10% of AGN are observed with ultra-luminous radio jets (Katgert et al., 1973). These synchrotron radio jets dig their way through the interstellar medium out of the host galaxy creating huge lobes. This may control the mass accretion rate, and the growth of SMBH and the galactic

bulge (Blandford et al., 2019). Thus, unraveling the AGN processes, such as its accretion and emission, will help us understand the relations between the SMBH and its host galaxy and their co-evolution.

1.1 The Unified Model of AGN

1.1.1 AGN classification

AGN have been historically classified based on their apparent observational properties, and might not necessarily reflect actual physical differences. As AGN can have detectable emission covering the whole electromagnetic spectrum, different observational traits observed in each spectral band can warrant a separate classification. For example, Padovani et al. (2017) reviewed the historical AGN types and classes with different morphological and spectral features, and found more than 50 distinct AGN types.

In the radio band, AGN are usually classified into Radio-loud (RL) and Radio-quiet (RQ) AGN based on the radio-loudness parameter R, which is the ratio between the radio flux at 5 GHz and the optical flux in the B band. Powerful RL and RQ quasars typically separate at values of R $\sim$ 10, while for lower luminosity AGN, the transition occurs at a much higher value (Chiaberge & Marconi, 2011; Sikora et al., 2007). Further, RL galaxies are characterized by extended radio emission and are differentiated into Fanaroff-Riley I and II based on the jet morphology and power (Fanaroff & Riley, 1974). RQ AGN with both broad lines and narrow lines in the optical/UV band are Seyfert 1 AGN whereas those with just narrow lines are Seyfert 2 AGN. Radio-loud equivalent of Seyfert 1 and Seyfert 2 are Broad Line Radio Galaxies (BLRGs) and Narrow Line Radio Galaxies (NLRGs) respectively. AGN whose non-thermal relativistic jet points at us are called Blazars and are characterized by rapid high amplitude variability from minutes to years and polarized emission in almost all band (optical, radio, X-rays). And there are a whole lot more AGN groups.

1.1.2 The basic AGN unification scheme

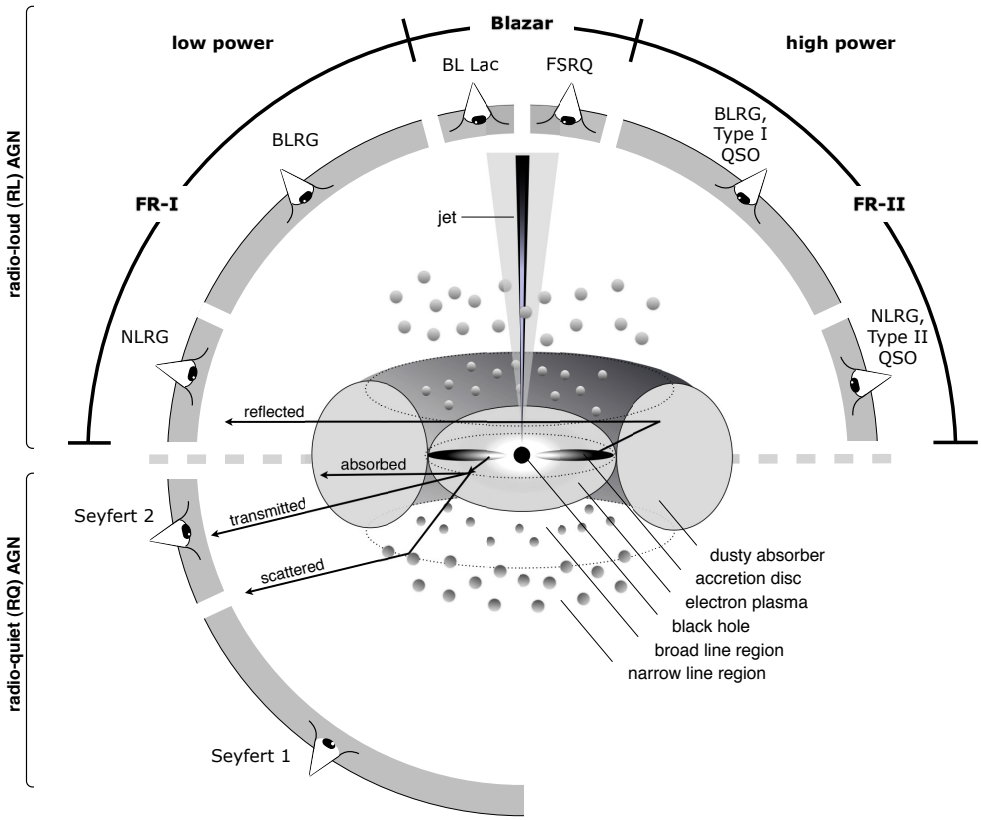

Figure 1.1: A schematic view of the basic AGN Unified model by Beckmann & Shrader (2012).

Despite this deluge of AGN classes, these differences have been shown to depend on only a small number of parameters, such as inclination (e.g. Netzer, 2015) and presence/absence of strong jets (e.g. Padovani, 2016). This led to the development of a simple unification model that could explain most of the distinct AGN classes. The basic unified model of AGN has become broadly accepted following the formalism and reviews by Antonucci (1993) and Urry & Padovani (1995). Here, the difference between AGN classes can be explained by an orientation effect where the obscuring torus affects the direct view of the AGN central engine.

In Figure 1.1, we show the artistic representation of the Unified model from Beckmann & Shrader (2012). Below, we briefly discuss several key components of an AGN within this basic picture:

- **Super massive black hole(SMBH):**

  SMBH is located at the center of an AGN. The accretion via the gravitational infall of matter from the circumnuclear environment onto this black hole powers the AGN central engine.

- **Accretion disk:**

  AGN accretion disk is usually modeled as an optically thick, geometrically thin structure formed from in-falling material which looses its angular momentum through friction within the disk. This results in a thermal black body emission, and the total radiation coming from the accretion disk can be interpreted as a multi-color black body emission.

- **Corona:**

  AGN corona is a compact high-temperature plasma near SMBH which is situated above the accretion disk. The relativistic electrons up-scatter the optical/ultraviolet photons from the accretion disk to high energies, primarily to the X-ray band, producing the bulk of the continuum X-ray emission.

- **Broad line region (BLR):**

  The Broad Line Region contains dust-free gaseous clouds close ($\sim$0.01–1 pc) to the actively accreting SMBH. The far UV continuum radiation originated in the accretion disk photo-ionizes these clouds creating emission lines, such as the Hydrogen Balmer lines and the lyman Series. These lines are Doppler broadened due to Keplerian bulk motions of the gas clouds moving at velocities $> 1000\,\mathrm{km\,s^{-1}}$.

- **Dusty torus:**

  A geometrically thick, axisymmetric dusty torus blocks the direct emission from the central engine of the AGN (accretion disk, BLR, corona) by reprocessing the X-ray, UV and optical photons, and re-emitting in the infrared wavelengths. It also collimates the emission resulting in a bi-conical ionization cone. This toroidal structure is different for different AGN with its size ranging from 0.1 to 10 pc.

- **Narrow line region (NLR):**

  The Narrow Line Region is a bi-conical structure of low-density ionized clouds emitting narrow permitted and forbidden emission lines. This region is located at around kpc scale with clouds moving at low velocities $< 1000\,\mathrm{km\,s^{-1}}$.

- **Relativistic jet:**

  About 10% of AGN are observed with collimated, energetic outflows of particles moving at relativistic velocities (Katgert et al., 1973). These relativistic jets are usually bi-directional, perpendicular to the accretion disk and can extend up to Mpc scales. They radiate non-thermal emission via Synchrotron and inverse-Compton scattering processes.

There are many studies in the literature that agrees with this basic unification model. Some of the strong supporting evidence are:

- Spectropolarimetric observations of several Seyfert 2 galaxies reveal the presence of broad permitted emission lines in polarized light [e.g.NGC 788 (Kay & Moran, 1998); NGC 1068 (Antonucci & Miller, 1985); NGC 424, NGC 591, NGC 2273, NGC 3081, and NGC 4507 (Moran et al., 2000)]. This is consistent with the view where Seyfert 2, like Seyfert 1, possess broad line regions but are obscured by a dense circumnuclear material.

- Using HST observation of [OIII] $\lambda 5007\AA$ emission , Schmitt et al. (2003) found that Seyfert 1 were likely to have halo-like NLRs, while Seyfert 2 NLR were more elongated. This is in agreement with the unified picture where the bi-conical NLR are observed more face-on in Seyfert 1s and more edge-on in Seyfert 2s.

- Studies have shown that the X-ray absorption column density in type-2 AGN are systematically higher than type-1 AGN (Awaki et al., 1991; Cappi et al., 2006). This is predicted by the unification model as the type-2 AGN are seen through the obscuring torus.

1.1.3 Modern perspective on the AGN unification

A smooth dusty torus which can block the AGN central engine based on its orientation is sufficient for the basic unified model but it clearly is a simplified approximation. Discovery of intermediate AGN groups, like Seyfert 1.5, with weaker BLR emission than Seyfert 1, cannot be explained solely by the smooth torus. Recent IR observations advocate the need for the torus to be clumpy and stabilized by frequent cloud-cloud collisions or by radiation pressure (Netzer, 2015). Further evidence of a clumpy torus has been found in recent years through infrared interferometric observations (López-Gonzaga et al., 2016; Tristram et al., 2007). Variability of the neutral X-ray absorption column, seen in AGN spectra on the timescale of days to years further supports the non-uniform nature of the torus (Ramos Almeida & Ricci, 2017). Further, the AGN observed to have gone through a classification change commonly referred to as the "changing-look AGN", can be explained by transiting dust clouds in the clumpy torus (Ricci et al., 2016).

Recent studies show the accretion rate to be one of the major factor in the observed AGN properties (Heckman & Best, 2014). If the accretion rate falls below a critical level, the standard AGN accretion disk can be replaced by an optically-thin radiatively inefficient accretion flow (Cao, 2005; Trump et al., 2011). Some narrow line type-2 AGN are found

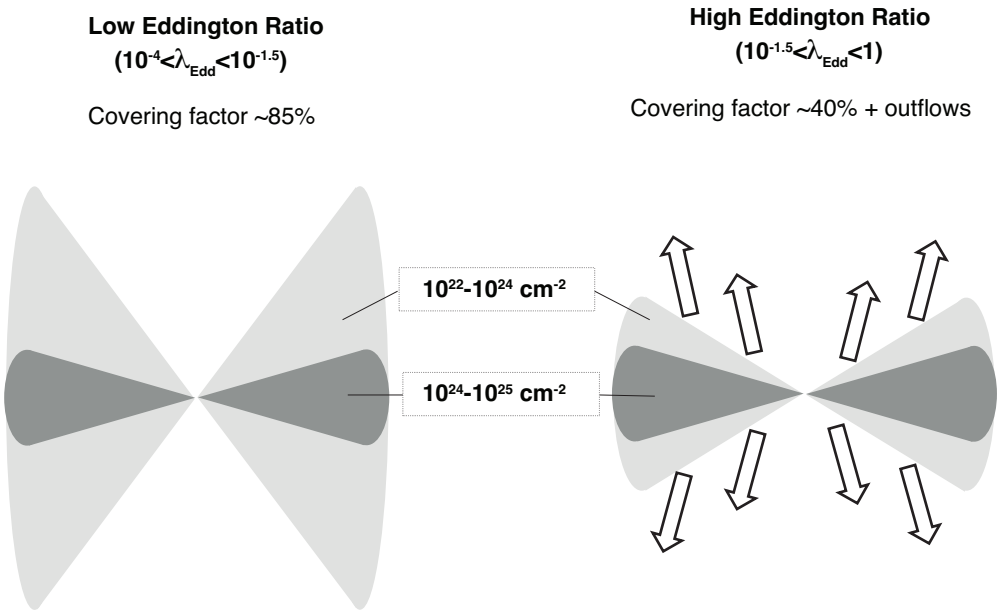

Figure 1.2: Schematic diagram showing the relation between the covering factor of the circumnuclear material and the Eddington ratio in the radiation-regulated feedback model. Figure from Ricci et al. (2017).

to be X-ray unabsorbed and could be explained as having accretion rate that is unable to sustain the BLR and torus (Elitzur & Ho, 2009).

Radiation-regulated unification model has been proposed in which the AGN accretion rate regulates the circumnuclear obscuration around the SMBH via AGN-driven outflows and radiative-driven feedback (Ricci et al., 2017). In this model, accretion rate is characterized by the Eddington ratio, the ratio of bolometric AGN luminosity to the Eddington luminosity which is the maximum theoretical luminosity of the central SMBH powered by spherical gas accretion. The fraction of sky covered by the obscuring material as seen from the SMBH is defined as the covering factor. In this scheme, the accretion can be cyclically triggered in a quiescent AGN. As material accumulates, the covering factor is high. The Eddington ratio

gradually increases until it becomes high enough to exert enough radiation pressure to expel most of the circumnuclear material and be quiescent again. This process is shown in Figure 1.2.

1.2 Studies of AGN using broadband X-rays

Studies of AGN have been done at every wavelength from radio to gamma-rays. X-rays are generated close, within few gravitational radii, of the SMBH. Moreover, the penetrative power of X-rays allows them to pass through large columns of obscuring materials. Thus, X-ray study of AGN is considered as the direct probe of the central engine.

The presence of a cold, neutral medium along the line of sight causes photoelectric absorption in the low energy X-rays (< 10 keV), which creates an absorption cutoff in the power-law spectrum. If the absorption column density is above 1×10^{24} cm^{-2}, it significantly suppresses the emission below 10 keV. These AGN are called Compton-thick AGN, and are difficult to perform broadband X-ray study. On the other hand, the Compton-thin AGN (column density between 10^{-22} and 10^{24} cm^{-2}) are really good sources to perform broadband X-ray study as they are relatively unobscured to study the intrinsic emission while showing some absorption features that can be used to infer their circumnuclear environment.

1.2.1 Components of a typical Compton-thin AGN

A typical Compton-thin AGN X-ray spectrum contains an strong underlying intrinsic X-ray continuum created via the Compton up-scattering of the optical/UV photons from the disk in the X-ray corona. This intrinsic spectrum depends on the properties of the corona and the seed photon spectrum (e.g. Titarchuk, 1994). However, in most cases it can be approximated well with a powerlaw continuum with a high-energy exponential cutoff.

The intrinsic X-ray continuum illuminates the accretion disk and the torus producing a characteristic X-ray reflection spectrum. This component is characterized by the presence

of a Compton hump, a broadband hump peaking at around 30 keV, and a fluorescent Iron Kα line (Netzer, 2015). The lower energy Compton hump rise is produced from the contest between absorption and Compton scattering of the X-ray continuum on the disk/torus. The Compton hump tail at higher energy is caused by Compton recoil and the high-energy cutoff of the continuum itself. The Fe-Kα line is prevalent in the reflection spectrum due to the abundance of iron which has high fluorescent yield (Fabian, 1999).

In significant fraction of Compton-thin AGN, soft X-ray emission in excess to that of the extrapolated hard X-ray continuum is observed below 2 keV and referred to as 'soft excess'. Its origin is still not completely understood, and is currently theorized to be either due to warm Comptonization or relativistic reflection from the accretion disk (Arnaud et al., 1985; Done et al., 2012; Walter & Fink, 1993).

In addition to the neutral absorption, the intrinsic AGN spectrum can further be modified by warm ionized absorption in the region close to SMBH. These warm absorbers can create a collection of absorption lines in the observed X-ray spectra. They can also travel at high velocities causing a broad absorption trough signatures (Tombesi et al., 2012).

All aforementioned components together create the total broadband X-ray spectrum of a typical Compton-thin AGN (see Figure 1.3). Constraining the physical parameter inferred from these components using physically-motivated models is a strong probe of the AGN central engine and its circumnuclear environment.

1.3 Outline of this Thesis

The focus of this thesis is to study the important feeding and feedback processes of Compton-thin AGN in the local universe using broadband X-ray spectroscopy often using supportive multiwavelength data. Study of the luminous but variable X-ray spectra of these AGN is further enhanced using a multi-epoch approach which can better constrain the relatively stable components. This work heavily relies on the broadband X-ray coverage

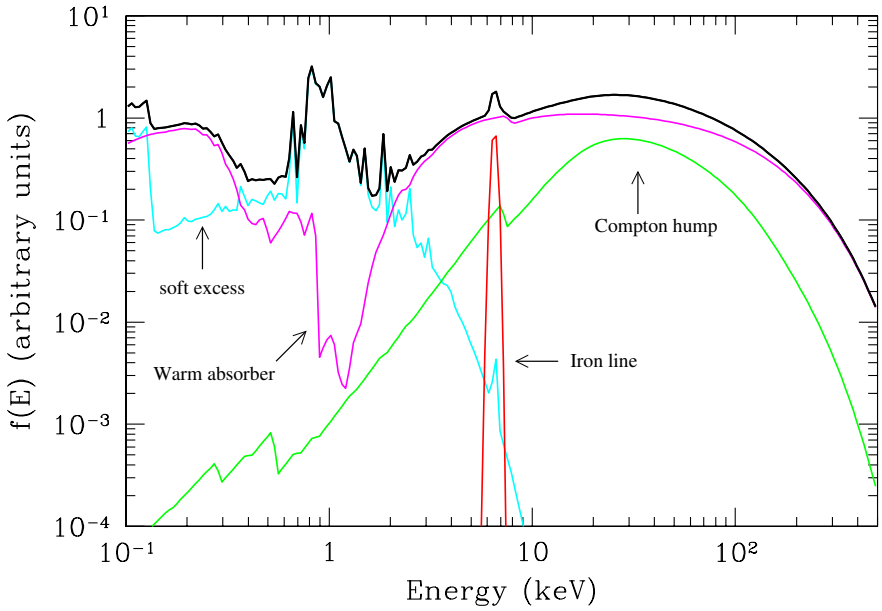

Figure 1.3: An example X-ray spectrum of a Compton-thin AGN is shown as black line. The underlying neutral Fe-Kα line (red), the Compton hump (green), the intrinsic continuum modified by warm absorber (magenta), and the soft excess (cyan) components are also shown. Figure from Risaliti & Elvis (2004).

provided by the combined efforts of *XMM-Newton* (covering the 0.3–10 keV band) and *NuSTAR* (covering the 3–79 keV band).

The first study, presented in Chapter 2, explores the broadband spectra of a broad-line radio galaxy 3C 109 using the joint 2017 *XMM-Newton*/*NuSTAR* observations for the first time. This study also incorporates an archival 2005 *XMM-Newton* observation. I performed a multi-epoch broadband spectral modeling in order to measure the high-energy cutoff. I also estimated the Eddington ratio using several methods. I discuss the disagreement between these estimates and question the existing black hole mass measurement.

In Chapter 3, I explore the origin of soft excess in the Seyfert 1 galaxy Mrk 926 using multi-epoch broadband X-ray spectra from *Suzaku* (2009), *XMM-Newton* and *NuSTAR* (2016), and *NuSTAR* and *Swift-XRT* (2021). I also discuss the detection of a possible radio jet in this source.

Finally, in Chapter 4, I study the circumnuclear environment of the 12 Polar-scattered Seyfert 1 galaxies using, often multi-epoch, archival broadband X-ray spectra alongside photometric and spectral data in the infrared. The data is modeled using a joint multi-wavelength clumpy torus model. I constrain both X-ray and IR torus parameters for these sources. I discuss the results in context of AGN unification models and past torus studies.

Chapter 5 provides an overview of the results presented in this thesis.

CHAPTER TWO

BROAD-BAND X-RAY OBSERVATION OF BROAD-LINE RADIO GALAXY 3C 109

2.1 Contribution of Authors and Co-Authors

Manuscript in Chapter 2

Author: Sulov Chalise

Contributions: Implemented study design. Wrote first draft of manuscript.

Author: Anne M. Lohfink

Contributions: Conceived the study design. Observation proposer. Provided feedback on manuscript drafts.

Author: Erin Kara

Contributions: Observation proposer. Provided feedback on manuscript drafts.

Author: Andrew C. Fabian

Contributions: Observation proposer. Provided feedback on manuscript drafts.

2.2 Manuscript Information

Sulov Chalise, Anne M. Lohfink, Erin Kara, Andrew C. Fabian

The Astrophysical Journal

Status of Manuscript:
____ Prepared for submission to a peer-reviewed journal
____ Officially submitted to a peer-reviewed journal
____ Accepted by a peer-reviewed journal
_X_ Published in a peer-reviewed journal

American Astronomical Society
July 2020,ApJ 897, 47
10.3847/1538-4357/ab94a2

2.3 Abstract

We present a study of the central engine in the broad-line radio galaxy 3C 109. To investigate the immediate surrounding of this accreting, supermassive black hole, we perform a multi-epoch broad-band spectral analysis of a joint *NuSTAR* /*XMM* observation (2017), an archival *XMM* observation (2005) and the 105-month averaged *Swift* -BAT data. We are able to clearly separate the spectrum into a primary continuum, neutral and ionized absorption, and a reflection component. The photon index of the primary continuum has changed since 2005 ($\Gamma = 1.61^{+0.02}_{-0.01} \rightarrow 1.54 \pm 0.02$), while other components remain unchanged, indicative of minimal geometric changes to the central engine. We constrain the high-energy cutoff of 3C 109 ($E_{cut} = 49^{+7}_{-5}$ keV) for the first time. The reflector is found to be ionized ($\log \xi = 2.3^{+0.1}_{-0.2}$) but no relativistic blurring is required by the data. SED analysis confirms the super-Eddington nature of 3C 109 initially ($\lambda_{Edd} > 2.09$). However, we do not find any evidence for strong reflection ($R = 0.18^{+0.04}_{-0.03}$) or a steep power law index, as expected from a super-Eddington source. This puts the existing virial mass estimate of 2 $\times 10^8 M_\odot$ into question. We explore additional ways of estimating the Eddington ratio, some of which we find to be inconsistent with our initial SED estimate. We obtain a new black hole mass estimate of 9.3 $\times 10^8 M_\odot$, which brings all Eddington ratio estimates into agreement and does not require 3C 109 to be super-Eddington.

2.4 Introduction

Active Galactic Nuclei (AGN) are powered by accretion onto the central supermassive black hole (SMBH). The accretion system is made up of several parts: a central set of relativistic electrons called the corona, an accretion disk and an axisymmetric dusty torus (Heckman & Best, 2014, and references therein). The AGN accretion disk emits mostly in the optical/UV band. The X-rays are generated in the AGN corona, which Compton up-

scatters the thermal accretion disk photons (Haardt & Maraschi, 1991). The relativistic jets, powered by the SMBH, seen in some AGN produce additional high-energy and synchrotron radiation Thus, AGN are observable from the radio up to γ-rays.

Although AGN are classified into several categories based on their observational properties, the AGN unification model explains most of this variation by a few physical differences such as inclination and luminosity (Urry, 2004). A major factor that dictates the AGN's observational traits, but is not explained by the unification model, is the presence or absence of relativistic particle jets. About 10% of AGN are observed with these jets that are ultra-luminous in the radio band (Katgert et al., 1973; Kellermann et al., 2016). These synchrotron radio jets inflate bubbles of relativistic plasma (Churazov et al., 2000) and dig their way through the interstellar medium out of the host galaxy creating huge lobes. This may result in the ejection or heating of the interstellar gas, which suppresses the SMBH accretion and ceases star formation (Fabian, 2012). Although it is safe to assume that some intrinsic properties of the AGN central engine will determine the presence of a strong jet component, the exact mechanism is still unknown. The black hole spin is considered to be a major factor in the jet strength (Blandford & Znajek, 1977). However, the discovery of many Seyferts with large measured spins but without a strong jet suggests some additional factor. Another hypothesis is that the jet production is governed by the Eddington-scaled low mass black hole accretion states (Blandford et al., 2019). The low-luminosity AGN that contain weak steady jets might be in the low/hard state,and the high-luminosity AGN might be in the very high/unstable state but cycle between soft sub-state and hard jet producing state (Meier, 2012). Thus, understanding the accretion-powered and X-ray-rich central engine is vital to unravel the AGN jet production mechanism.

In this context, X-ray studies of AGN can be considered a direct probe of the AGN's central engine since X-rays are created close to the SMBH and can penetrate large columns of obscuring material often present in AGN (Gandhi, 2005). In addition to the primary

X-ray continuum from the corona, a typical AGN X-ray spectrum also contains a reflection component generated from the reprocessing of the primary X-ray emission on the surface of the accretion disk or the torus. This X-ray reflection spectrum can reveal substantial information about the central engine of the AGN (Fabian et al., 1995; Gandhi, 2005) and has been used to constrain the spin of black holes (Parker et al., 2014; Reynolds, 2019), the radius of the inner-disk region (Ghosh et al., 2016) and the temperature of the corona (García et al., 2015; Lohfink et al., 2015). While soft X-rays can be obscured by neutral or ionized gas, reflection features in the hard X-rays such as the fluorescent Fe Kα line (Fabian et al., 1989) and the "Compton hump" feature around $10 - 25$ keV due to Compton reflection/scattering of X-rays from the disk or pc scale torus (Ross et al., 1999), can be used to study even highly-obscured AGN (Arévalo et al., 2014).

Most AGN whose central engines have been studied are non-jetted. Jetted AGN, in addition to being scarce, are sometimes oriented such that the jet emission overpowers their spectra. Due to the limited studies of jetted AGN, we cannot be sure whether there are any differences in the central engine between jetted and non-jetted AGN. Broad-line radio galaxies (BLRGs) are ideal objects to study in this context as they are oriented such that the central engine is directly observable but the jet is not in the direct line-of-sight. Although BLRGs share the presence of broad optical lines with radio-quiet type I AGN, BLRGs typically have harder power-laws, smaller Fe Kα equivalent widths and weaker reflection features (Ballantyne, 2007; Grandi et al., 2006; King et al., 2017; Lohfink et al., 2013; Sambruna et al., 2009). High quality broad-band X-ray studies of several BLRGs have been performed after the launch of the *NuSTAR* observatory (Harrison et al., 2013). Using two *NuSTAR* observations of BLRG 3C 382, Ballantyne et al. (2014) found the presence of Comptonizing corona with very weak reflection features, compared to what is usually found in Seyfert galaxies. Similarly, Comptonization parameters for the BLRG 3C 390.3 were constrained by Lohfink et al. (2015) using broad-band X-ray data. Using radio/X-ray

data, a link between the events in the jet emission and accretion disk has been studied in the BLRG 3C 111 (Chatterjee et al., 2011) and the BLRG 3C 120 (Lohfink et al., 2013; Rani & Stalin, 2018). Studying more BLRGs will provide valuable data points needed to study the difference between jetted and non-jetted central engines.

In this paper, we study the broad-band spectra of 3C 109, a luminous BLRG at $z = 0.306$. 3C 109 stands out as a BLRG as its Eddington ratio has been estimated to be super-Eddington, while other BLRGs have Eddington ratios of a few tens of per cent at maximum (Lohfink et al., 2015; Ursini et al., 2018). We aim to explore this atypical nature of 3C 109 in detail.

There have been several studies of 3C 109 in different emission bands. Its supermassive black hole mass has been estimated to be $\log(M/M\odot) \sim 8.3$ (McLure et al., 2006). Previous works on 3C 109 using *ASCA* and *VLBI* observations revealed the presence of an Fe Kα line, excess neutral absorption and a radio jet of $\sim$ 280 kpc scale. Using *VLBI* data the inclination of 3C 109's jet was constrained to $35^\circ < i < 56^\circ$ (Giovannini et al., 1994). Using *ASCA* data, Allen et al. (1997) found a broad Fe Kα line with an intrinsic FWHM $\sim 120,000$ km s^{-1}. Using *XMM* observations Miniutti et al. (2006) found 3C 109 to be accreting above the Eddington limit along with the presence of blurred ionized reflection and excess neutral and ionized absorption.

Here, we present the results of a joint *XMM* ($\sim$ 64 ks) and *NuSTAR* ($\sim$ 140 ks) observation. The sensitivity of *NuSTAR* in the hard X-rays allows us to study the reflection spectrum of 3C 109 in unprecedented detail. The partially simultaneous *XMM* data provide us with valuable soft X-ray coverage. We focus on the broadband spectral analysis of 3C 109, including the full reflection spectrum for the first time. This paper is structured as follows. In Section 2.5, we report on the observations and data reduction. In Section 2.6, we perform the short and long term spectral variability analysis. In Section 2.7, we present the analysis of the spectra. The results are discussed in Section 2.8.

Table 2.1: X-ray observations investigated in this paper.

Observatory (ObsID)	Start time	Net Exposure
NuSTAR (60301011002)	2017-08-20 01:56:09	61.4 ks
NuSTAR (60301011004)	2017-08-22 20:06:09	81.7 ks
XMM (0200910101)	2005-02-03 17:33:35	40.5 ks
XMM (0795600101)	2017-08-20 02:33:43	63.6 ks

Table 2.2: *XMM*-OM observations studied in this paper.

OM Band (ObsID)	Start time	Net Exposure
W1 (0200910101)	2005-02-03 17:33:35	39.2 ks
W1, V (0795600101)	2017-08-20 02:33:43	62.3 ks

2.5 Data Reduction

2.5.1 Overview

In this paper, we analyze the *NuSTAR* (Harrison et al., 2013) observations of 3C 109 along with a simultaneous *XMM* pointing. In addition to these unpublished observations, we also consider an archival *XMM* (Miniutti et al., 2006) observation and the 105-month averaged *Swift -BAT* spectrum (Oh et al., 2018). Table 2.5.1 provides an overview of the X-ray observations considered and Table 2.5.1 of the observations at other wavelengths.

2.5.2 XMM-Newton

In this work we consider the data from two *XMM* observations (Table 2.5.1). Data from both EPIC-pn and EPIC-MOS are considered. We have processed the *XMM* data using the *XMM-Newton* Scientific Analysis System (SAS version 15.0.0). The signal-to-noise of RGS was very low and no spectral information could be obtained. The EPIC data were first

screened and periods of high particle backgrounds rejected. The spectra were produced from the created event files using `evselect`. Responses were created with `arfgen` and `rmfgen`.

The OM photometry was obtained using `omichain` and `omdetect`. The OM data were only of good quality in the W1 and V filters, all other filter bands were too affected by imaging artifacts to yield reliable photometry. As 3C 109 is an elliptical galaxy, we assume that the galaxy contribution to the OM bands would be minimal.

2.5.3 NuSTAR

We produce cleaned event files using `nupipeline`. To reduce the times with high particle background but maximize exposure time, we study the background filtering reports provided by the *NuSTAR* team. To minimize the effect of the SAA and thereby the background noise, we select SAAMODE "optimized" and also exclude the "tentacle" region. From the cleaned event files we extract source spectra (70" circular region) and the background spectra (95" circular region). 3-25 keV light curves are also extracted with a 2 ks time resolution.

2.6 Spectral Variability

2.6.1 Short-term Flux Variability

We inspect the light curves (Fig 2.1) of the recent *NuSTAR* and *XMM-Newton* observations to assess the short-term spectral variability of 3C 109. By eye, no variation is present, and a constant provides an acceptable description of the light curves (*NuSTAR* : $\chi^2 = 125.2$ for 121 d.o.f. ; *XMM-Newton* : $\chi^2 = 22.8$ for 29 d.o.f.). Without the presence of any short-term flux variability, we only consider the observation-averaged spectra for the remainder of this work.

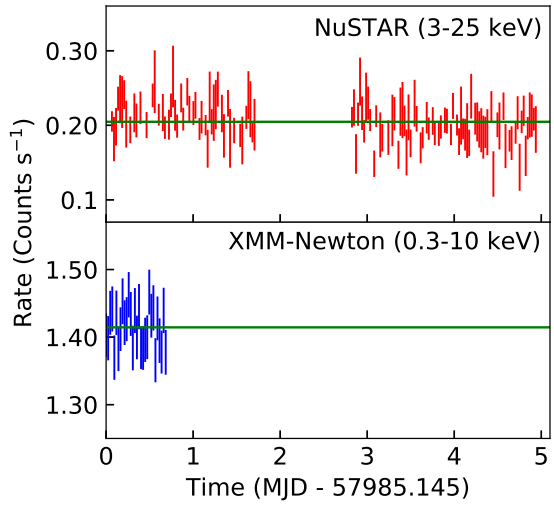

Figure 2.1: We show the background-subtracted *NuSTAR* (top) and *XMM*-Newton (bottom) light curves with 2 ks time resolution. A constant (green) is an acceptable fit for both light curves.

2.6.2 Long-term Flux Variability

We measure a flux of $(10.2 \pm 0.1) \times 10^{-13}\,\mathrm{erg\,cm^{-2}\,s^{-1}}$ in the 1-2 keV band using the *XMM EPIC-PN* observation and an absorbed power law model. Miniutti et al. (2006) have compiled the long-term evolution of 3C 109's flux in that energy band in Figure 6 of their paper. Figure 2.2 shows our new flux measurement along with those reported in Miniutti et al. (2006). Long-term X-ray variability is present with a 30% flux decrease with respect to the last pointed X-ray observation of the source in 2005 and 17% lower flux than the 39-year average.

2.7 Spectral Analysis

X-ray spectral analysis is a great tool to study an AGN central engine. To constrain 3C 109's central engine parameters, we perform a detailed analysis of the recent spectral *NuSTAR* and *XMM* data in this section. We, then, continue with a 'multi-epoch analysis' where we improve upon those constraints by including the archival *XMM* data (Miniutti

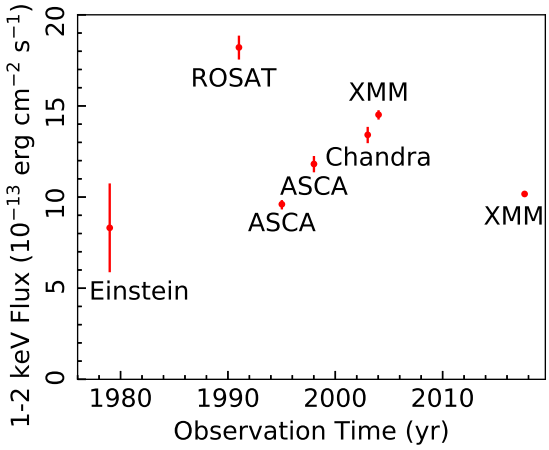

Figure 2.2: The historical X-ray flux of 3C 109 in the 1-2 keV band adopted from Miniutti et al. (2006). The telescope used to measure the flux is displayed along with each data point. The rightmost point is the recent flux value from *XMM* . We see a 30% flux decrease from the 2005 *XMM* observation.

et al., 2006) and 105-month averaged *Swift -BAT* data (Oh et al., 2018).

Throughout this work, the spectral modeling is performed using *XSPEC* 12.10.0c (Arnaud & A., 1996). We use the built-in χ^2 minimization technique to fit the data, which are binned to a minimum of 20 counts per bin. All errors were calculated at 90% confidence level. We always include a cross correlation constant in all of the subsequent model fits to account for any cross-calibration flux offsets among different detectors. Further, we include a galactic absorption component in all of our models to account for the ISM absorption from our galaxy. To describe the ISM absorption, we use the ISM absorption model `TBabs` (Wilms et al., 2000) and fix the column density value to the total galactic column density, $N_{\rm H} = 1.53 \times 10^{21}$ cm^{-2} obtained from the N$_{\rm H}$ Tool (Kalberla et al., 2005).

2.7.1 NuSTAR

As no short-term spectral variability was found (Section 2.6.1), an average spectra for each *NuSTAR* detector, FPMA and FPMB, are created from the two *NuSTAR* observations. The resulting spectra are analyzed in the energy range 3 - 70 keV. The data

above 70 keV for *NuSTAR* are discarded due to high background. Both averaged spectra are fitted simultaneously.

To get a first glimpse of the spectral shape before performing any complex modeling, we initially fit a simple power-law model as a rough description of the primary X-ray continuum. We obtain an acceptable fit with $\chi^2 = 1054.9$ for 899 d.o.f. Now, we check for the presence of a high-energy cutoff to the power-law. We find that if we use a power-law model with a cutoff, the fit improves significantly ($\Delta\chi^2$ improvement of 64.2 for 1 extra parameter). From a visual inspection of the ratio residuals of this fit around 5 keV (Fig 2.3,middle-top), we suspect the presence of an iron line. To model the probable iron line, we add a redshifted Gaussian line component to the cutoff power-law model. We fix the redshift to the known value for 3C 109, z= 0.306. We obtain a $\Delta\chi^2$ improvement of 17.1 for 3 extra parameters and a line at energy $6.47^{+0.19}_{-0.17}$ keV with line width of $0.24^{+0.30}_{-0.24}$ keV. The ratio residuals for this fit (Fig 2.3,middle-bottom) show that the inclusion of the Gaussian line has removed the line-like feature from the previous-fit ratio residuals (positive ratio residuals around 5 keV). With the detection of the high-energy cutoff and the iron line, we can confidently rule out a strong jet contribution in the X-ray band.

Although the previous model describes the averaged spectral data well, it is not a self-consistent model and the origin of the fitted line is unclear. Thus, we are motivated to use a self-consistent model that can naturally explain the line. We test the reflection model, `xillver` (Garcia et al., 2013), which explains the line as being caused by X-ray reflection of power-law photons off the accretion disk or other surrounding material. We assume a neutral reflector initially ($\log \xi = 0$). We fix the reflector inclination to 35°, which is the upper limit from the VLBI observation for the jet inclination (Giovannini et al., 1994). The power-law photon index (Γ), iron abundance ($\mathrm{Fe_{abund}}$), high-energy cutoff (E_{cut}) and reflection fraction (R) are free to vary. We obtain a good description of the spectra with $\chi^2 = 960.9$ for 895 d.o.f. and flat ratio (Fig 2.3,bottom). We find a power-law photon index of $1.61^{+0.12}_{-0.08}$, an iron

abundance of $2.1^{+2.0}_{-1.4}$, a high-energy cutoff of 55^{+27}_{-10} keV and a reflection fraction of 0.27 ± 0.06.

Allowing for an ionized reflector ($\log \xi > 0$) or relativistic blurring of the reflection using `relxill` (Garcia et al., 2014) does not lead to a statistically significant fit improvement.

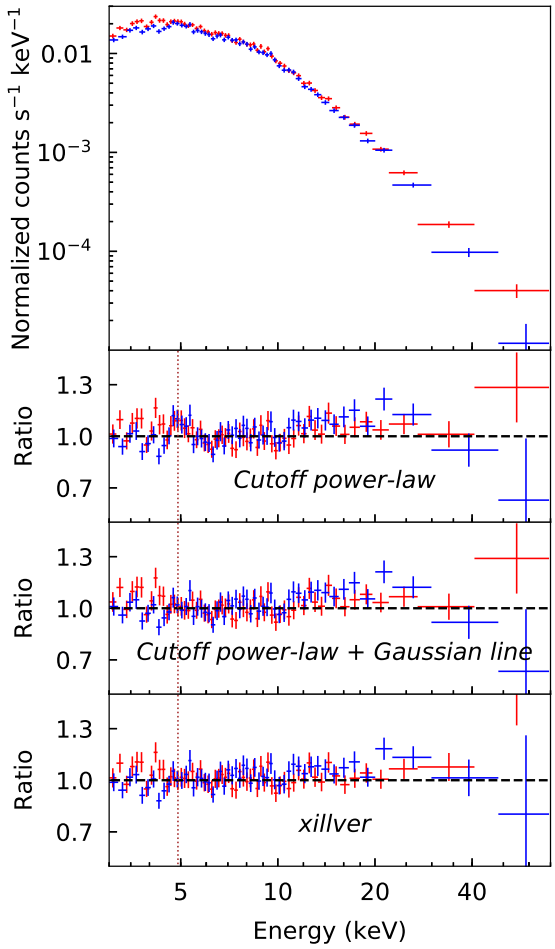

Figure 2.3: The counts spectrum (top) and the ratio residuals for the spectral modeling of the *NuSTAR* data are shown for both FPMA (red) and FPMB (blue). The middle-top panel shows the ratio residuals for a cutoff power-law model. The middle-bottom panel shows the ratio residuals for the cutoff power-law model with a redshifted gaussian line. The bottom panel shows the ratio residuals for the self-consistent reflection model, `xillver` . The dotted brown line marks the 6.4 keV rest frame energy.

2.7.2 XMM-Newton

After exploring the *NuSTAR* spectra, and clarifying the origin of the X-ray emission, we are ready to analyze the recent *XMM-Newton* spectra of 3C 109. Spectra from all three EPIC CCD detectors are fitted simultaneously. As these detectors are sensitive, calibrated, and match in the energy range 0.3 - 10 keV for our observations, we discard the data points outside this range. Just as we did during the *NuSTAR* analysis, we start again with a simple power-law model. This is a bad description of the data ($\chi^2 = 12765$ for 2061 d.o.f.) This could be indicative of unmodeled absorption as excess obscuration of 3C 109 along the line of sight modifies the spectrum below 10 keV. Absorption could therefore explain the bad fit of the *XMM* spectra but not the *NuSTAR* spectra for the same model.

To improve the fit, we add a neutral absorption component to the power-law model. This component is modeled by `zTBabs` with a free-to-vary column density (N_H) at the source's redshift in order to account for any intrinsic neutral absorption. This modification significantly improves the fit to $\chi^2 = 2304.2$ for 2059 d.o.f. The ratio residuals of this fit (Fig 2.4, middle-top) show an iron line-like feature around 5 keV, which corresponds to 6.4 keV in the source rest frame.

To explain the origin of the Fe Kα line, we use the self-consistent reflection model, `xillver` (Garcia et al., 2013), still retaining the `zTBabs` component. We assume a neutral reflector initially ($\log \xi = 0$). The inclination is again fixed at 35°. The power-law photon index (Γ), iron abundance and reflection fraction are free to vary. The high-energy cutoff cannot be constrained below 10 keV, so it is fixed at the best fit value of 55 keV obtained from the *NuSTAR* modeling. The fit improves to $\chi^2 = 2288.9$ for 2058 d.o.f. Allowing for an ionized reflector ($\log \xi > 0$), we obtain a $\Delta\chi^2$ improvement of 29.2 for 1 extra parameter. With the detection of ionized reflection, we can assume this reflector to be an accretion disk. The ratio residuals of this fit (Fig 2.4, middle-bottom) still show signs of extra unmodeled absorption around 0.5 keV. The extra absorption was also seen by Miniutti

et al. (2006) and was attributed to the presence of an intrinsic ionized absorber. To model the ionized absorption, we create a custom photoionized absorption table model using the `XSTAR2XSPEC` script, which uses the `xstar` (v2.54 ; Kallman & Bautista, 2001) code to produce an `xspec` -compatible, multiplicative tabulated model grid. The model is calculated assuming the material has a covering fraction of unity, a typical temperature of 10^6 K, a typical density of $10^{12}\,\mathrm{cm}^{-3}$, an ionizing luminosity of $3\times10^{45}\,\mathrm{ergs\,s}^{-1}$ (based on the observed flux), a turbulent velocity of $100\,\mathrm{km\,s}^{-1}$ and solar abundances. We also assumed a power-law spectrum with the photon index of 1.6 as illuminating flux. The resulting table model has two free parameters: the absorption column and the ionization parameter. The redshift of this absorber is fixed at the source redshift. We multiply this model component with the previous model, which leads to an improved fit with $\chi^2 = 2114.1$ for 2055 d.o.f. The ratio residuals of this fit (Fig 2.4,bottom) show no additional significant features. We obtain a power-law photon index of 1.55 $\pm$0.02, an iron abundance of $3.6^{+6.4}_{-1.7}$, an ionization parameter of $2.3^{+0.1}_{-0.2}$ erg cm s^{-1} and a reflection fraction of 0.19 ± 0.06. These values are comparable to the values found in Section 2.7.1 for the modeling of the *NuSTAR* dataset. We are able to constrain the neutral absorbing column to $3.14 \pm 0.9 \times 10^{21}$ cm^{-2}, and the ionized absorbing column to $7.0 \pm 1.5 \times 10^{21}$ cm^{-2} with ionization parameter of $1.02^{+0.07}_{-0.06}$ erg cm s^{-1}.

Allowing for relativistic blurring of the reflection using `relxill` (Garcia et al., 2014) does not lead to a statistically significant fit improvement.

2.7.3 Multi-epoch analysis

As AGN have inherently variable spectra, we cannot average two spectra taken at different epochs. In particular, we have already established the long-term variability of 3C 109 in Section 2.6.2. So, we cannot utilize the 2005 *XMM* observation to generate an averaged *XMM* spectra with better signal-to-noise. However, we can perform a multi-epoch analysis, which utilizes data from different epochs, to improve constraints on the physical

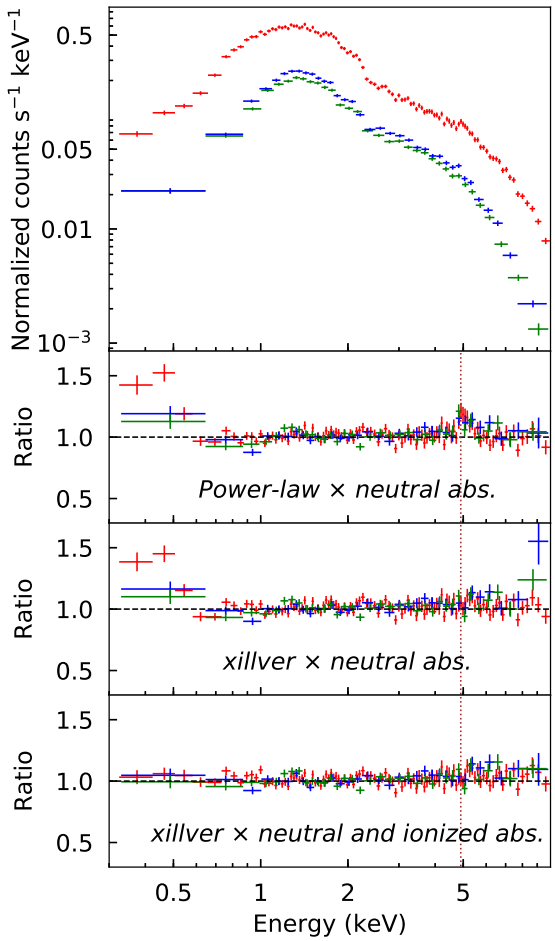

Figure 2.4: The counts spectrum (top) and the ratio residuals of the spectral modeling of the *XMM* data are shown for *EPIC-PN* (red), *MOS-1* (blue) and *MOS-2* (green). The middle-top panel shows the ratio residuals for a power-law model with intrinsic neutral absorption. The middle-bottom panel shows the ratio residuals for the self-consistent reflection model, `xillver` with intrinsic neutral absorption. The bottom panel shows the ratio residuals for `xillver` with intrinsic neutral and ionized absorption. The dotted brown line marks the 6.4 keV rest frame energy.

parameters expected to be non-variable between the epochs. Thus, we perform a multi-epoch analysis in which not only spectra from *NuSTAR* and *XMM* are fitted jointly but also spectra from different epochs are included.

The 3C 109 X-ray spectra included in this multi-epoch analysis are the recent *XMM-Newton* and *NuSTAR* spectra along with the archival 2005 *XMM-Newton* spectra

(Miniutti et al., 2006) and the *Swift -BAT* spectrum (Oh et al., 2018). The *Swift -BAT* spectrum covers the very hard X-rays, and has a high signal-to-noise ratio as it is a long-term average spectrum. All spectra are fitted together by linking the parameters expected to remain constant, on physical grounds.

We describe the spectra using the best fit model from the *XMM* analysis, ionized reflection along with intrinsic neutral and ionized absorption. The parameter states, fixed or variable, are identical to Section 2.7.2 except for the high-energy cutoff, which is free to vary due to the inclusion of hard X-ray data. All parameters are linked together among the different epochs except for the power-law photon index, reflection fraction and normalization. These parameters are linked between the recent *XMM-Newton* and *NuSTAR* spectrum. As *Swift -BAT* only consists of hard X-ray data, it cannot constrain the reflection fraction and the high-energy cutoff independently and thus it is linked with the recent *XMM-Newton* and *NuSTAR* data, in order to able to obtain meaningful constraints.

We find a neutral absorbing column of $3.38^{+0.6}_{-0.7} \times 10^{21}$ cm^{-2}, and an ionized absorbing column of $6.64^{+1.0}_{-0.9} \times 10^{21}$ cm^{-2} with ionization parameter of $1.05^{+0.07}_{-0.05}$ erg cm s^{-1}. These match the values obtained in Section 2.7.2. The power-law photon index appears to have changed between the two *XMM* observations ($\Gamma = 1.61^{+0.02}_{-0.01} \rightarrow 1.54 \pm 0.02$). The high-energy cutoff is constrained to 49^{+7}_{-5} keV, while the ionization of the reflector was found to be $2.3^{+0.1}_{-0.2}$ erg cm s^{-1}. The most-recent epoch parameter values are comparable to those of previous sections (2.7.1, 2.7.2) but with improved constraints. In Table 2.3, we report the best fit ($\chi^2 = 4669.7$ for 4589 d.o.f.) values for all parameters of significance for this description of the data. In Figure 2.5, we show the best-fit ratio residuals for *XMM* -PN (2017: brown, 2005: green), *XMM* -MOS1 (2017: cyan, 2005: red), *XMM* -MOS2 (2017: yellow, 2005: blue), *NuSTAR* -FPMA (magenta), *NuSTAR* -FPMB (orange) and the 105-month averaged *Swift* -BAT data (black). The model describes the data well, and allowing for relativistic blurring of the reflection using `relxill` (Garcia et al., 2014) does not lead

to a statistically significant fit improvement.

The results are in agreement to what is found if only the recent *XMM* and *NuSTAR* spectra are modeled together but with better constraints.

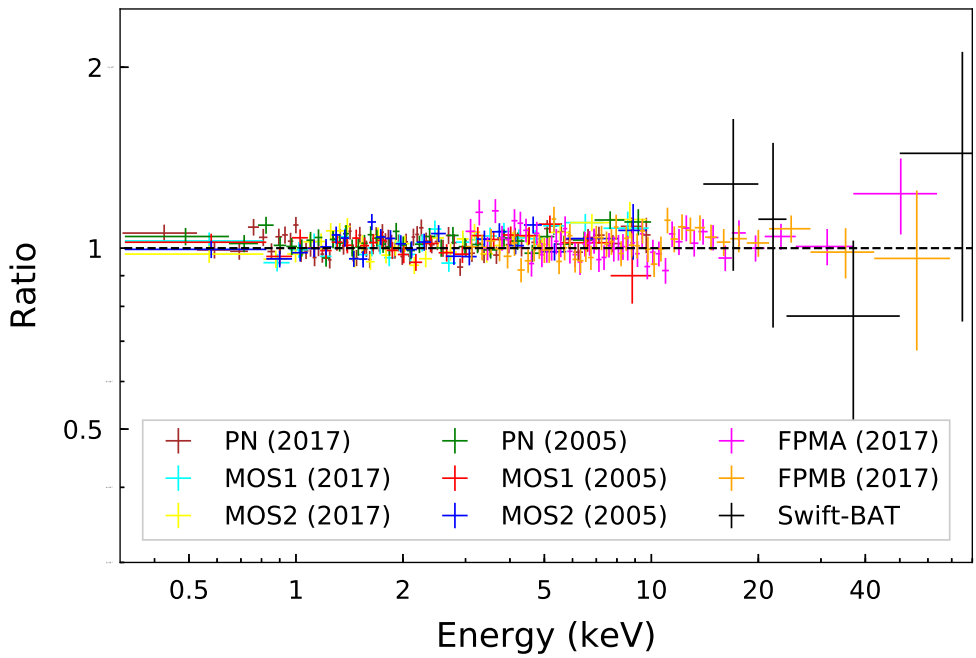

Figure 2.5: The plot shows the best-fit ratio residuals for *XMM*-PN (2017: brown, 2005: green),*XMM*-MOS1 (2017: cyan, 2005: red),*XMM*-MOS2 (2017: yellow, 2005: blue), *NuSTAR* -FPMA (magenta), *NuSTAR* -FPMB (orange) and the 105-month averaged *Swift*-BAT data (black).

2.8 Discussion

2.8.1 Summary

In this paper, we present the analysis of the recent *NuSTAR* and *XMM* observations of the broad-line radio galaxy 3C 109 taken in 2017. We found the new X-ray data to have no significant short-term variability, but determined that the 1-2 keV flux fluctuates on long timescales (years) as is expected for AGN (McHardy, 2010, and references therein). The 2-10 keV unabsorbed flux was found to be $5.99 \pm 0.04 \times 10^{-12}$ erg cm^{-2} s^{-1} based on

Table 2.3: Best fit parameter values of the multi-epoch Broad-band X-ray data.

Parameter	**Spectra***	**Value**
Neutral absorption column	All	$3.38^{+0.6}_{-0.7} \times 10^{21}\,\mathrm{cm}^{-2}$
Ionized absorption column	All	$6.64^{+1.0}_{-0.9} \times 10^{21}\,\mathrm{cm}^{-2}$
Ionized absorption ionization	All	$1.05^{+0.07}_{-0.05}\,\mathrm{erg\ cm\ s}^{-1}$
Power-law photon index	2017	1.54 ± 0.02
	2005	$1.61^{+0.02}_{-0.01}$
	B	$1.22^{+1.2}_{-0.2}$
Iron abundance	All	$4.0^{+3.7}_{-1.2}$
High-energy cutoff	All	49^{+7}_{-5} keV
Ionization	All	$2.3^{+0.1}_{-0.2}\,\mathrm{erg\ cm\ s}^{-1}$
Reflection fraction	2017+B	$0.18^{+0.04}_{-0.03}$
	2005	0.14 ± 0.05

* '2017' refers to recent *NuSTAR* and *XMM-Newton* spectra, '2005' refers to the archival *XMM-Newton* spectra and 'B' refers to the time-averaged Swift-BAT spectra. 'All' refers to all aforementioned spectra. For 'All', the parameter values are linked among all spectra whereas, for '2017+BAT' they are linked between '2017' and 'B'.

the *XMM* observation and the best fit model, corresponding to a 2-10 keV luminosity of $1.66 \pm 0.01 \times 10^{45}$ erg s^{-1} in the source's rest frame. The spectral analysis of the recent observations has revealed that the X-ray spectra are well characterized by a primary X-ray continuum from the corona and its reflection from an ionized reflector. It is likely that this

ionized reflector is the accretion disk. The observed soft X-ray spectrum is further modified by intrinsic neutral and ionized absorption. This result agrees with the previous *XMM* -based study by Miniutti et al. (2006), although we were unable to confirm evidence for a relativistic blurring of the reflection spectra using our model on the same observation. This discrepancy is likely due to a different model used, or an improvement on the *XMM* data calibration.

We also perform a multi-epoch analysis using the recent 3C 109 observations along with the available 2005 *XMM* observation and the 105-month averaged *Swift -BAT* spectra in order to obtain better constraints on the non-variable parameters. This also permits us to study the evolution of changeable AGN parameters within the full time-frame of the analysis. We find that there is a change of the photon index of the primary power-law continuum from $1.61^{+0.02}_{-0.01}$ to 1.54±0.02 between the 2005 *XMM* observation and the new 2017 observation, consistent with the softer-when-brighter behavior widely observed in AGN (McHardy et al., 1999; Sobolewska & Papadakis, 2009), while other parameters remain the same within errors. This might mean that 3C 109's central engine has not changed significantly since 2005 and the photon index variation can be explained solely by the changes to the corona.

2.8.2 Contribution of the jet

3C 109 is a FR II radio galaxy with two symmetric lobes with hot spots and core emission (Giovannini et al., 1994). The core component of the jet emission can provide a flux contribution to the observed spectrum of 3C 109. If this contribution is significant, spectral modeling must account for a jet component.

As 3C 109 is lobe-dominated, the majority of jet emission stems from the lobes. The size of 3C 109's jet is 110 arcsec with a projected linear size of $\sim$ 280 kpc (Giovannini et al., 1994). So, the core, the northern lobe and the southern lobe of the jet are well separated. X-ray and optical/UV observations of 3C 109 only include the contribution from the weak

jet core but not from the luminous lobes, as those are easily resolved.

In Section 2.7.1, we already ruled out a strong jet contribution to the X-ray band (i.e. coronal emission). However, we must check the jet contribution to 3C 109's accretion disk spectrum in the optical/UV to be able to model it.

In order to estimate this jet flux contribution, we study the SED of 3C109. Figure 2.6 shows the archival flux measurements in the radio-optical band from the NASA/IPAC Extragalactic Database (NED) as black points. At radio frequencies, the measurements suggest the presence of a strong radio-jet. However, these are the total radio flux (core+lobes) measurements. As an FR II radio galaxy, 3C 109's jet has a well separated core, and only the core radio flux could be confused with the accretion disk emission. Thus, we plot the radio core flux (red points) as obtained by Antonucci & Barvainis (1988), based on observations where the core and lobes were resolved. Also, Chini et al. (1989) performed observation of 3C 109 at 1300 micron (green point), and found that this 1300 micron flux measurement lies well below the extrapolation of the radio core spectrum using the core radio flux measurements from Antonucci & Barvainis (1988). They further noted that the 1300 micron flux measurement can be seen as an upper-limit of the high frequency spectrum of 3C 109's radio core. This suggests that the radio core spectrum diminishes rapidly towards shorter wavelengths and makes a basically negligible flux contribution to the optical-X-ray band. These observations are some time in the past and one may wonder about the applicability of those results to our much more recent data. Ekers et al. (1983) showed that the 5 GHz radio core varies in the flux range 180–400 mJy from observations in the period 1974–1980. Subsequent 5 GHz radio core flux measurements have also been within that range. Although, there is evidence of some variability, this variability is not strong enough to alter our results in any way.

To give an overview of the energy budget of 3C109, we also include higher frequency data (2017 *XMM* -OM: magenta ; 2017 *XMM* -PN: red ; 2017 *NuSTAR* -FPMA: blue ; 105-

month averaged *Swift* -BAT data: purple). All optical and UV fluxes shown are corrected for extinction from the Milky-Way, whereas all X-ray fluxes are corrected for both intrinsic and Milky-Way X-ray absorption. 3C 109 is not detected in the γ-ray, and only its upper limit is shown in Figure 2.6 (gold). The non-detection of 3C 109 in the γ-ray regime is consistent with a weak jet core (Kataoka et al., 2011).

Hence, we can assume the X-ray and optical/UV emission in 3C 109 is dominated by corona and accretion disk physics.

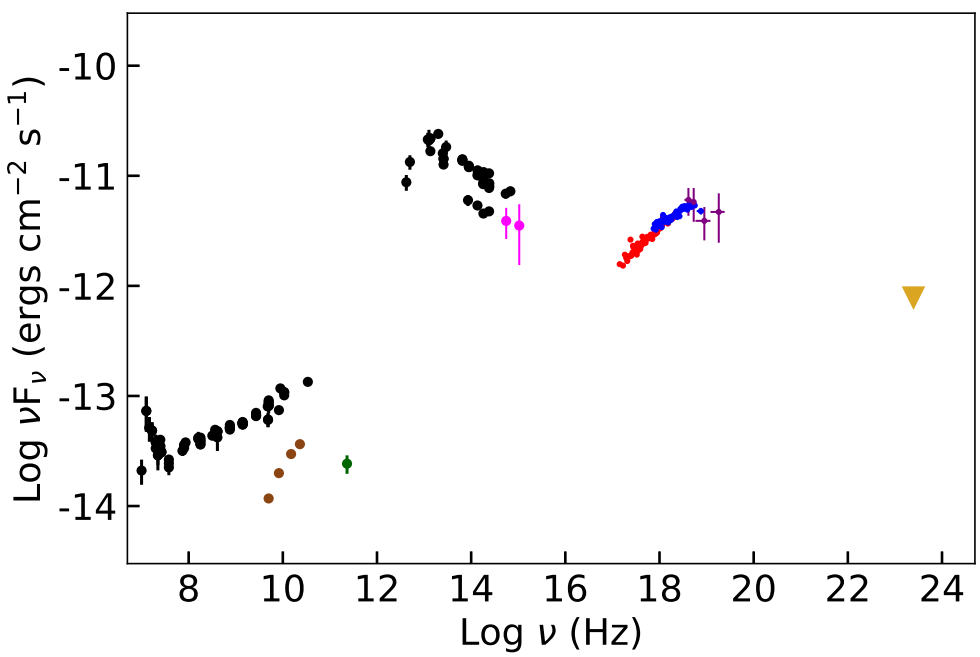

Figure 2.6: 3C 109 SED: The archival radio-optical flux measurements from the NASA/IPAC Extragalactic Database (NED) are shown in black. Brown points are the archival radio core flux from Antonucci & Barvainis (1988). The green point is the flux measurement at 1300 microns from Chini et al. (1989). We plot the 2017 *XMM* -OM flux (magenta). All the optical-UV flux are Milky-Way extinction corrected. We also plot the 2017 *XMM* -PN (red), *NuSTAR* -FPMA (blue) along with the 105-month averaged *Swift* -BAT data (purple), all of which are absorption-corrected.

2.8.3 The lack of evidence of strong relativistic blurring

Ballantyne (2007) concludes that the three necessary criteria for the production of

powerful radio jets are: a rapidly spinning black hole, an inner accretion flow with a large H/r and and a favorable magnetic field geometry. A recent review paper by Reynolds (2019) confirms this. A consequence of the first criterion is the expected presence of strong relativistic blurring of the reflection spectra and ionized reflection. Even though 3C 109 possesses a powerful radio jet, we find its spectra do not require the presence of relativistic blurring for the best fit model. This could be indicative of the lack of significant relativistic blurring effects of the reflection spectra. This lack may be explained by a truncated accretion disk, as it is predicted by the jet cycle model thought to operate in broad-line radio galaxies (Lohfink et al., 2013; Marscher et al., 2002). Modeling the recent data from Section 2.7.1 and 2.7.2 together with the relativistic reflection model, `relxill` (Garcia et al., 2014), we obtain a lower limit of 59 ISCO for the inner radius of the reflector assuming a maximally rotating black hole ($\chi^2 = 3087.6$ for 2952 d.o.f.) However, the presence of a highly truncated accretion disk is at odds with our finding of a significantly ionized accretion disk with log ξ $= 2.3^{+0.1}_{-0.2}$.

An alternative theory in which the corona is at a significant height from the accretion disk might explain this conundrum. This fits well with the idea that the AGN corona is the base of the particle jet, which can form at several tens of gravitational radii above the disk (King et al., 2017; Markoff & Nowak, 2004; Markoff et al., 2005). This height of the corona will minimize the relativistic effects near the ISCO while allowing the disk to be ionized. Modeling the multi-epoch data from Section 2.7.3 with the relativistic reflection model for a lamp-post geometry, `relxilllp` (Garcia et al., 2014), we obtain a lower limit of 336 gravitational radii for the coronal height assuming a maximally rotating black hole. We note that this model is a worse fit than the best-fit model ($\chi^2 = 4711.5$ for 4585 d.o.f.) Further, the high value of the required height of the corona makes this theory a likely explanation for the lack of evidence of strong relativistic blurring.

Another possible explanation for the absence of evidence of strong relativistic reflection

is the presence of a corona in which the plasma is outflowing away from the disk. The outflow at mildly relativistic speeds causes aberration, reducing the X-ray emission towards the disk (Beloborodov, 1999) and thus resulting in a reduced irradiation of the disk near the ISCO.

2.8.4 The UV/X-ray Spectral Energy Distribution

In Figure 2.7, we construct the UV/X-ray spectral energy distribution (SED) of 3C 109 using the recent *XMM* -PN (red), *XMM* -OM (magenta), *NuSTAR* -FPMA (blue), along with the 105-month averaged *Swift* -BAT data (purple). We exclude the archival *XMM* -OM data as it has single data point in the W1 band, but we note that the observed archival W1 flux is 46% higher than the recent W1 flux. The X-ray data and the best-fit X-ray model from Section 2.7.3 (green line) plotted in Figure 2.7 are corrected for both galactic and intrinsic absorption. The recent *XMM* -OM (magenta) data is corrected for galactic extinction using reddening E(B-V) of 0.57. (Schlegel et al., 1998).

In Figure 2.7, we also plot the accretion disk spectral model, `diskpn` (Gierliński et al., 1999), using a typical maximum disk temperature of 10 eV and an inner disk radius of 6 $R_g(= GM/c^2)$. This is shown as a black line in Figure 2.8.4. As we can clearly see, the *XMM* -OM (magenta) data do not match the slope of this disk spectrum. Assuming that it is in fact the disk emission, this indicates further extinction of the *XMM* -OM data.

Using infrared spectrophotometry, Rudy et al. (1999) noticed that 3C 109's infrared spectrum had significantly higher spectral index ($\alpha \sim 1.5$) than expected ($\alpha = -0.8$) from an accretion disk spectra. They use an accretion disk spectral model similar to ours, and calculate 3C 109's in-situ reddening E(B-V) of 0.77. If we correct our *XMM* -OM (magenta) data for an in-situ reddening, E(B-V) of 0.77 reported by Rudy et al. (1999), we find that these updated flux values (orange) also do not match an accretion disk spectrum. If we assume an in-situ reddening E(B-V) of 0.32, however, the resulting flux points (brown) do match an accretion disk spectrum. Given the time since the data analyzed in Rudy

et al. (1999) was taken, a change in reddening would not be unusual. We assume this new reddening to be true, and normalize the theoretical accretion disk spectrum such that it passes through the new flux points (brown).

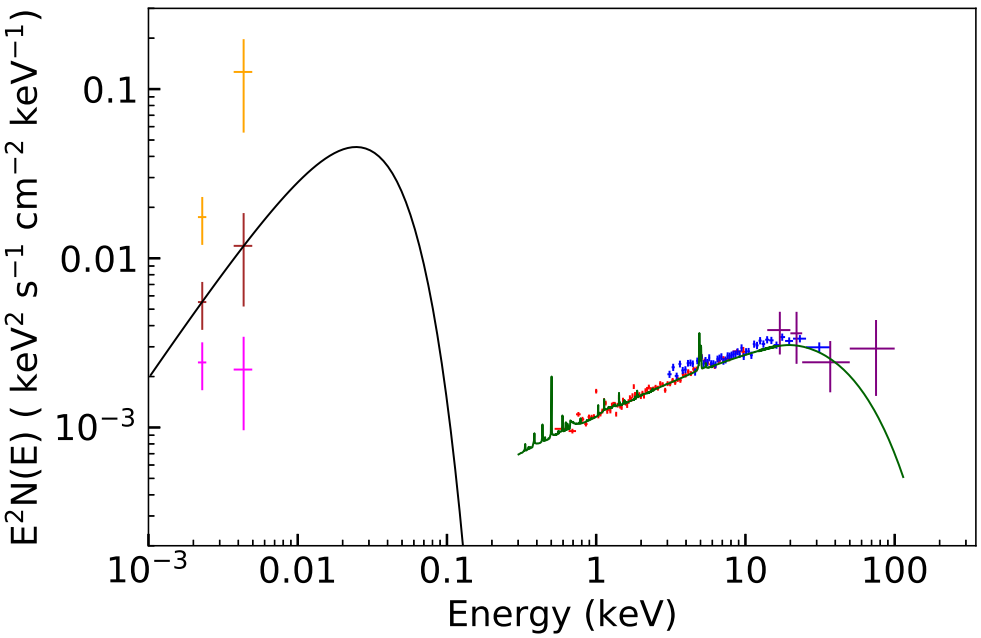

Figure 2.7: 3C 109 UV/X-ray SED: We plot the recent *XMM* -PN (red), *NuSTAR* -FPMA (blue) along with the 105-month averaged *Swift* -BAT data (purple). All data are absorption-corrected. We also plot the Milky-Way extinction corrected *XMM* -OM data (magenta) along with the source extinction correction using the previous E(B-V) value of 0.77 (orange) and the updated E(B-V) value of 0.32 (brown). The solid green line represents the unabsorbed X-ray reflection model and the solid black line represents the disk blackbody model assuming a maximum disk temperature of 10 eV.

Additionally, we can relate the optical/UV accretion disk emission to the coronal X-ray emission using the spectral index, which is defined as $\alpha_{\rm ox} = \log(L_{2\,\rm keV}/L_{2500\text{Å}})/\log(\nu_{2\,\rm keV}/\nu_{2500\text{Å}})$, where $L_{2\,\rm keV}$ and $L_{2500\text{Å}}$ are the monochromatic luminosities 2 keV and 2500 Å respectively (Avni & Tananbaum, 1982). For 3C 109, we find $\alpha_{\rm ox}$ to be 1.33 ± 0.08. We have shown in Section 2.8.2, 3C 109 does not have a significant jet contribution to its optical and X-ray spectrum, and thus should have comparable $\alpha_{\rm ox}$ to its radio-quiet counterparts. Using a sample of 545 X-ray selected radio-quiet type 1 AGN, Lusso et al.

(2010) found the mean $\alpha_{\rm ox}$ of 1.37 $\pm$ 0.01. The 3C 109 $\alpha_{\rm ox}$ is only slightly deviated from this mean value. Also, this $\alpha_{\rm ox}$ agrees with the average $\alpha_{\rm ox}$ = 1.44$\pm$ 0.13, Green et al. (1995) obtained from the radio-loud sources from *ROSAT* observations of The Large Bright Quasar Survey. For the radio-quiet sources of the same sample, they found $\alpha_{\rm ox}$ of 1.57 $\pm$ 0.15. However, this study does not account for any contribution of jet to the optical and X-ray band, and should be interpreted with caution. Using γ-ray emission from 18 BLRGs, Kataoka et al. (2011) showed that for these BLRGs the non-thermal (jet) component can contribute a few percent up to 35 percent of the observed SED. So, without properly accounting for jet contribution, the $\alpha_{\rm ox}$ mean for a sample of radio-loud AGN is unreliable.

2.8.5 Super-Eddington outlier or faulty SMBH mass estimate?

Using the best-fit SED model from Section 2.8.4, we find the lower limit on the 3C 109's bolometric luminosity to be 5.2×10^{46} erg s^{-1}. Utilizing the black hole mass of $\log(M/M_{\odot})$ = 8.3 $\pm$ 0.4 from an Hβ virial mass estimation (McLure et al., 2006), we find a lower limit on the Eddington ratio of 2.09. Similarly, using a bolometric correction of 20 (Vasudevan & Fabian, 2007), we find a bolometric luminosity estimate of $L_{bol} \sim 3.32 \times 10^{46}$ erg s^{-1} from the 2-10 keV luminosity corresponding to an Eddington ratio of $1.32^{+2.0}_{-0.8}$. Both of these Eddington ratio estimates appear to agree with the super-Eddington nature of 3C 109 as reported by Miniutti et al. (2006).

Although observed to have a seemingly super-Eddington luminosity, 3C 109 lacks other characteristics of super-Eddington AGN. Super-Eddington sources usually exhibit softer power-law spectral indexes ($\Gamma > 2.5$), strong reflection and often possess strong outflows (Laurent & Titarchuk, 2011; Zubovas & King, 2012). As 3C 109 lacks all three of the expected features, we question its super-Eddington nature.

We note that both Eddington ratio estimates depend on the SMBH mass estimate. Additionally, the estimate from the SED modeling is also dependent on the accretion disk

maximum temperature, which we have fixed to a value of 10 eV. Thus, we seek an additional way of estimating the Eddington ratio independent of the black hole mass.

Using a sample of 92 bright, soft X-ray selected AGN, Grupe et al. (2010) found a correlation between $\alpha_{\rm ox}$ and Eddington ratio (λ_{Edd}) given by the relation,

$$\alpha_{\rm ox} = (0.11 \pm 0.02) \log \lambda_{Edd} + (1.39 \pm 0.02) \tag{2.1}$$

Using our $\alpha_{\rm ox}$ value of 1.33 $\pm$0.08, we find an Eddington ratio of $0.28^{+1.43}_{-0.06}$. Additionally, we note that as the radio-loud AGN have smaller $\alpha_{\rm ox}$ values than radio-quiet AGN, this Eddington ratio could be an overestimate.

In order to compare these three Eddington ratio estimates in relation to the parameters they depend on, we turn to a theoretical estimate. Assuming a non-rotating black hole with a thin accretion disk, Eddington ratio and the maximum accretion disk temperature in Kelvin, $\mathrm{T_{max}}$, are related as

$$\lambda_{Edd} \approx 0.583 \times \left(\frac{1.8}{f_{col}}\right)^4 \times 10^7 \mathrm{M_8} \times \left(k\mathrm{T_{max}}\right)^4 \tag{2.2}$$

(Gierliński & Done, 2004) where, f_{col} is the color temperature correction, $\mathrm{M_8}$ is the black hole mass in units of 10^8 $\mathrm{M_\odot}$ and k is the Boltzmann constant in units of keV/Kelvin. Here, we use a color temperature correction of 1.8, a suitable value for accretion close to the Eddington limit (Shimura & Takahara, 1995). In Figure 2.8, we plot the theoretical Eddington ratio estimate using Equation 2.2 for a range of maximum accretion disk temperature for the originally observed 3C 109 mass of 2×10^8 $\mathrm{M_\odot}$ as a black dashed line. We also include the expected Eddington ratio for a maximum accretion disk temperature of 10 eV. It is shown as a black 'square' and annotated as $\lambda_{Edd,thindisk}$. Its errorbars originate from the SMBH mass uncertainty.

The observational Eddington ratio estimates are shown as well in Figure 2.8. The

Eddington ratio estimate using the lower limit on the bolometric luminosity from the SED fitting is shown using a black 'circle' and annotated as $\lambda_{Edd,SED,M_8=2}$. Also, the Eddington ratio estimate using the bolometric correction factor of 20 on the 2-10 keV luminosity is shown using a black 'diamond' and annotated as $\lambda_{Edd,bolo}$. Again the uncertainty originates from the SMBH mass estimation. Finally, the Eddington ratio estimate using the Equation 2.1 is shown using a green 'plus' and annotated as $\lambda_{Edd,corr}$. Its errors are those of Equation 2.1.

As we can clearly see in Figure 2.8, the mass and temperature independent Eddington ratio estimate using Equation 2.2 does not agree with the Eddington ratio estimate using the lower limit on the bolometric luminosity from the SED fitting. Also, they both do not agree with the theoretical Eddington ratio estimate for a SMBH mass of 2×10^8 $M_\odot$ and maximum accretion disk temperature of 10 eV. Hence, we search for a new maximum accretion disk temperature and SMBH mass, which will unite all the Eddington ratio estimates.

We begin by finding the SMBH mass that will make the Eddington ratio estimate using the bolometric correction factor of 20 equal to the mass and temperature independent Eddington ratio estimate derived from Equation 2.1. This mass is 9.3×10^8 $M_\odot$ and is our new SMBH mass estimate. Now, we plot the theoretical Eddington ratio estimate for a range of maximum disk temperatures for this new mass, M_8=9.3, as a blue dashed line. We now find the maximum disk temperature that equates this new theoretical Eddington ratio estimate to the mass and temperature independent Eddington ratio estimate using Equation 2.1, i.e. find the $T_{\rm max}$ where the $\lambda_{Edd,corr}$ measurement meets the blue line. This maximum disk temperature is 8.5 eV and is our new maximum disk temperature estimate. Now, using these new estimates, we find a new lower limit on the Eddington ratio from the SED fitting, which is shown using a blue 'circle' and annotated as $\lambda_{Edd,SED,M_8=9.3}$.

Thus, if we assume a SMBH mass of 9.3×10^8 $M_\odot$ and a maximum disk temperature of 8.5 eV for 3C 109, all of the Eddington ratio estimates agree with a value of 0.28. If

correct, 3C 109 would not be super-Eddington, consistent with the lack of the expected super-Eddington features in the spectrum. We caution that this new mass estimate has several assumptions/simplifications associated with it, which affect its reliability. Hence, an updated 3C 109 mass estimate using more accurate and less error prone techniques, such as reverberation mapping, is needed before we can classify 3C 109 as a sub-Eddington AGN with absolute certainty.

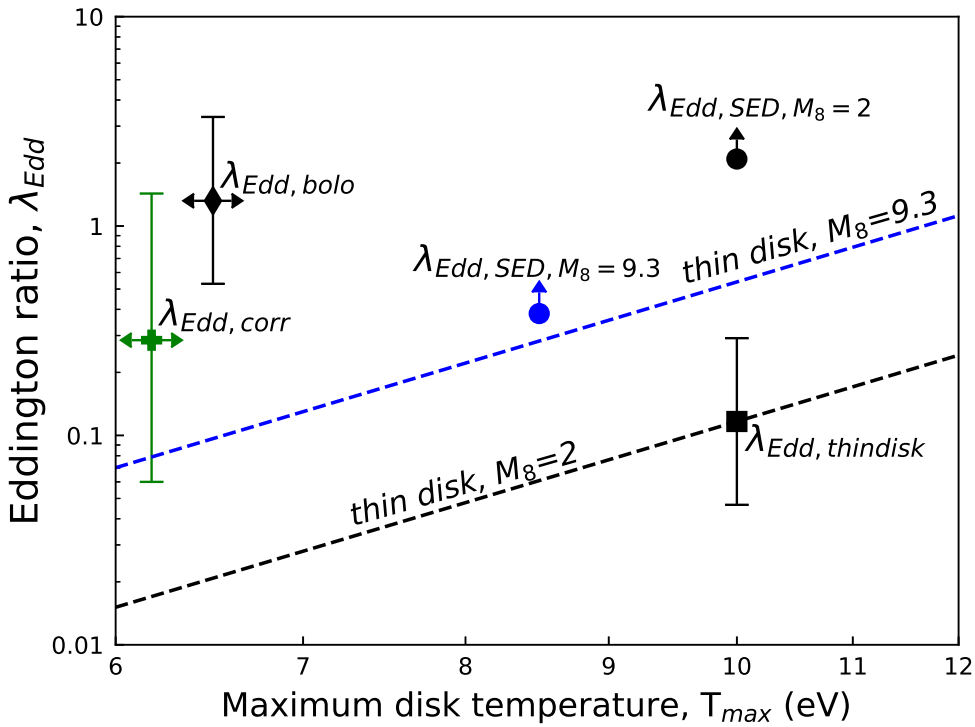

Figure 2.8: Eddington ratio vs Maximum disk temperature. The dashed lines are the theoretical prediction for a thin accretion disk using Equation 2.2 for SMBH mass of M_8=2 (black) and M_8=9.3 (blue). Eddington ratio estimate for a thin accretion disk assuming M_8=2 and T_{max}=10 eV, $\lambda_{Edd,thindisk}$, is shown using a black 'square'. The Eddington ratio estimate using the correlation from Equation 2.1, $\lambda_{Edd,corr}$, is shown using a green 'plus'. The Eddington ratio estimate using the bolometric correction factor of 20 on the 2-10 keV luminosity of 3C 109 with SMBH mass of 2×10^8 $M_\odot$, $\lambda_{Edd,bolo}$, is shown using a black 'diamond'. The Eddington ratio lower limit from the SED fitting is shown using a 'circle'. The black circle assumes a SMBH mass of 2×10^8 $M_\odot$ and a maximum disk temperature of 10 eV, while the blue circle assumes a SMBH mass of 9.3×10^8 $M_\odot$ and a maximum disk temperature of 8.5 eV.

2.8.6 Low temperature corona

Ricci et al. (2017) found a median high-energy cutoff energy of 381 ± 16 keV for 731 non-blazar AGN from a sample of 836 *Swift* /BAT objects with soft X-ray observations. Meanwhile, the best-fit high-energy cutoff of 3C 109 is only 49^{+7}_{-5} keV (Table 2.3) which is much lower than average non-blazar AGN value. To put this in physical context, we can approximate the electron temperature of every optically-thin plasma to be half of the high-energy cutoff (Petrucci et al., 2001). Thus, 3C 109 coronal electron temperature is approximately 25 ± 3 keV. This low electron temperature can be explained by the strong radiation fields expected from a super-Eddington disk, which cools the corona via Compton cooling (Kara et al., 2017). However, this explanation is contingent on 3C 109 being super-Eddington.

Alternatively, the presence of hybrid plasma consisting of both thermal and non-thermal particles can also explain the observed low cutoff energy (Fabian et al., 2017). The coronae harboring hybrid plasma are compact and highly magnetized. The compactness of an AGN corona can be quantified as a dimensionless radiative compactness parameter (Fabian et al., 2015):

$$\ell = \frac{\mathrm{L} \cdot \sigma_{\mathrm{T}}}{\mathrm{R} \cdot m_e c^3} \tag{2.3}$$

where, L is the luminosity, R is the radius, σ_{T} the Thomson cross section and m_e the mass of the electron. This radiative compactness will modulate the electron-positron pair production which in turn will regulate the coronal temperature (Fabian et al., 2015). For 3C 109, we do not have a coronal size estimate. Thus, we assume a spherical corona, 10 gravitational radii in size which is a conservative assumption as pointed out by Fabian et al. (2015). Using the mass of 2×10^8 $\mathrm{M}_\odot$, we get R= 2.9×10^{14}cm. From the 0.1-200 keV unabsorbed X-ray continuum luminosity ($6.0\pm0.2\times10^{45}$ ergs/s) calculated from the joint 2017 *XMM* -

NuSTAR fit, we find $\ell = 550 \pm 10$ accounting just the uncertainty in luminosity. This value is higher than the usual range between 10 and 100 (Fabian et al., 2015). Coupled with the low coronal temperature, it is evident from Figure 1 of Fabian et al. (2017) which presents the Electron temperature – compactness distribution along with the runaway pair production boundaries, the thermal pair-production as a dominating cooling mechanism for 3C 109 is questionable. Although 3C 109 lies on the allowed region of this plot, it is not clear what stabilizes this thermal coronae lying well below the pair production limit. Fabian et al. (2017) also show that even a small fraction of non-thermal particles in compact corona leads to lower equilibrium temperatures. A nonthermal fraction between 0.23 and 0.29 yields a stable corona (Figure 3 (left panel) of Fabian et al. (2017)). Thus, a hybridized corona can also explain the low coronal temperature of 3C 109. But, sensitive hard X-ray observation is needed to confirm this hypothesis (Fabian et al., 2017).

Although, if we assume the new SMBH mass estimate from section 2.8.5, we find ℓ of 118 ± 10 from Equation 2.3. This new value is still well below the pair production limit. Thus retaining the possibility of hybridized plasma.

Acknowledgments

We thank the anonymous referee for his/her valuable suggestions and comments. This work was supported under NASA Contract No. 80NSSC17K0615, and made use of data from the NuSTAR mission, a project led by the California Institute of Technology, managed by the Jet Propulsion Laboratory, and funded by the National Aeronautics and Space Administration. This research has also made use of the NASA/IPAC Extragalactic Database (NED), which is funded by the National Aeronautics and Space Administration and operated by the California Institute of Technology."

CHAPTER THREE

BROADBAND SPECTRAL ANALYSIS OF MRK 926 USING MULTI-EPOCH X-RAY OBSERVATIONS

3.1 Contribution of Authors and Co-Authors

Manuscript in following chapter

Author: S. Chalise

Contributions: Implemented study design. Wrote first draft of manuscript.

Author: A. M. Lohfink

Contributions: Conceived the study design. Observation proposer. Provided feedback on manuscript drafts.

Author: J. Chauhan

Contributions: Help on the radio section. Provided feedback on manuscript drafts.

Author: T. D. Russell

Contributions: Help on the radio section. Provided feedback on manuscript drafts.

Author: D. J. K. Buisson

Contributions: Observation proposer. Provided feedback on manuscript drafts.

Author: L. Mallick

Contributions: Help on the X-ray reflection. Provided feedback on manuscript drafts.

3.2 Manuscript Information

S. Chalise, A. M. Lohfink, J. Chauhan, T. D. Russell, D. J. K. Buisson, L. Mallick

Monthly Notices of the Royal Astronomical Society

Status of Manuscript:
____ Prepared for submission to a peer-reviewed journal
_X_ Officially submitted to a peer-reviewed journal
____ Accepted by a peer-reviewed journal
____ Published in a peer-reviewed journal

Oxford University Press
June 07, 2022

3.3 Abstract

The X-ray spectra of some active galactic nuclei (AGN) show a soft X-ray excess, emission in excess to the extrapolated primary X-ray continuum below 2 keV. Recent studies have shown that this soft excess can be described well as originating from either a relativistic ionized reflection, the extreme blurring of the reprocessed emission from the innermost region of the accretion disk, or Comptonization from an optically thick and warm region called the 'warm corona', in which electron scattering is the dominant source of opacity. To constrain the origin of the soft excess in the Seyfert 1 galaxy Mrk 926, we carry out an multi-epoch X-ray spectral study using observations from *Suzaku* (2009), *XMM-Newton* and *NuSTAR* (2016), and *NuSTAR* and *Swift-XRT* (2021). The broadband X-ray spectra of Mrk 926 contains: a thermally Comptonized primary continuum, a variable soft excess, and distant reflection. We find that in Mrk 926 as in so many sources, it is difficult to make a definite statement as to what is causing the observed soft excess. A warm coronal-like component is slightly preferred by the data but a reflection origin is also possible. Using archival radio data, we detect an optically-thin radio component in our broadband study of Mrk 926. While this component is consistent with an optically-thin radio jet, future multi-wavelength observations including high spatial resolution radio observations at multiple frequencies are required to probe the origin of the radio emission in more detail.

3.4 Introduction

Active galactic nuclei (AGN) are powered by accretion onto the supermassive black hole (SMBH) at the galactic center of their host galaxies. They are highly energetic, and common X-ray sources in the universe. X-ray emission from AGN, produced at the innermost region, is a great probe to study the physical processes in the extreme gravity regime. A subgroup of AGN, the Seyfert 1 galaxies, are particularly useful, in an observational sense, due to the

relatively unobscured view of their central engine.

All Seyfert 1 X-ray spectra share key similarities. Their primary X-ray emission can be approximated as a cut-off powerlaw, and is consistent with being produced via thermal Comptonization of optical-UV photons from the accretion disk. This thermal Comptonization occurs in a compact region called the hot corona (Haardt & Maraschi, 1991; Haardt et al., 1994). A part of this primary emission can be reprocessed by interacting with different regions of the accretion disk or the dusty torus, generating a 'reflection' spectrum. Reflection from distant matter generates a neutral Fe Kα fluorescent emission line (George & Fabian, 1991; Matt et al., 1991) at 6.4 keV. If the reflection is from an area closer to the SMBH, Doppler shift and gravitational redshift broadens the fluorescent line profile (Fabian et al., 1989) and more complex line emission is produced as the material is ionized. The reflection spectrum is also accompanied by the "Compton hump" feature around 20–30 keV due to Compton scattering of the primary continuum from the disk or parsec (pc) scale torus (Ross et al., 1999).

In more than 50 % of Seyfert 1 galaxies, soft X-ray emission in excess to that of the extrapolated hard X-ray continuum is observed below 2 keV and referred to as 'soft excess'. Its origin is still not completely understood, and is currently theorized to be either due to warm Comptonization or relativistic reflection from the accretion disk (Arnaud et al., 1985; Done et al., 2012; Walter & Fink, 1993; Winter et al., 2012). The emitted X-rays can also be obscured by the gas and dust present in the line-of-sight, imparting absorption features. All these components make up a typical Seyfert X-ray spectrum. We can study the AGN phenomenon by analyzing this spectrum using physically motivated models.

A group of nearby Seyfert 1 galaxies that show little to no X-ray absorption are the so-called "bare Seyferts". Their study is free from the uncertainties introduced from the complex modeling of the absorption providing a clear measurement of the central region. Mrk 926, also known as MCG-2-58-22, is a local (z=0.047) X-ray luminous "bare" AGN

classified in the optical as a Seyfert 1.5 galaxy. The lack of extended structures in the radio observations of Mrk 926 (VLBA, 8 GHz) with a high temperature sub-pc scale core supports its "bare" classification (Mundell et al., 2000). We usually expect cold and diffuse radio emissions from dusty obscurers. Also, Mrk 926's 2–10 keV X-ray flux is known to vary on a timescale of months to years (Choi et al., 2002, 2001). AGN variability can provide an additional probe into the scale and structure of the innermost region. Thus, a clear view of a variable central engine makes Mrk 926 an interesting X-ray source.

Mrk 926 has been observed previously with many X-ray observatories such as *ROSAT* , *ASCA* , *XMM* , and *BeppoSAX* (Bianchi et al., 2004; Choi et al., 2001; Weaver et al., 1995, etc.). Those observations have revealed the presence of a variable soft excess (Ghosh & Soundararajaperumal, 1992), a variable Fe K line profile (Weaver et al., 2001), and a Compton hump (Bianchi et al., 2004) atop the primary continuum. This was also confirmed by the analysis of a 140 ks *Suzaku* observation (Rivers et al., 2011), which found a primary power-law continuum, a soft excess and placed tight constraints on the strength and nature of the reflection features. The authors also found no significant evidence for broadening of the Fe line expected from the inner accretion disk reflection (Rivers et al., 2011). The same *Suzaku* and the 2016 joint *XMM -NuSTAR* observations were studied by Laha & Ghosh (2021), where the authors found the vanishing of Compton-hump between 2009 and 2016 observations with similar primary continuum. The authors proposed a scenario of a dynamic torus structure as an explanation (Laha & Ghosh, 2021).

A recent velocity-resolved reverberation mapping of Mrk 926 was carried out by Kollatschny et al. (2022) with a detailed spectroscopic and photometric variability study of its very broad emission lines (FWHM $\gg 4000\,\mathrm{km\,s^{-1}}$). They found a drastic decrease of the optical continuum luminosity (50% in 2.5 months) suggesting high variability. The inclination angle of the line emitting region was found to be $\sim$50°. The black hole mass was derived to be $1.1(\pm 0.2) \times 10^8 \mathrm{M}_\odot$, indicating a low Eddington ratio (3-8%). Interestingly,

they also found additional fast-response outer emission components, the Balmer satellites, which originate in a different, spatially distinct region such as a small-scale central radio jet.

There are still several open questions regarding Mrk 926's X-ray spectrum, mentioned in the following text. Using archival *ROSAT* and *ASCA* data, Choi et al. (2001) found a broad iron line centered at ~ 6.3 keV. This is not unexpected from a bare nucleus as we have a clear view of the innermost emission regions where the relativistic broadening of the iron line happens. However, other studies such as Rivers et al. (2011) (140 ks *Suzaku* broadband data) and Bianchi et al. (2004) (simultaneous $\sim$ 7 ks *XMM* and *BeppoSAX* broadband data) did not find a broadened line. Therefore, a pertinent question is whether the broad iron line is a transient phenomenon in Mrk 926 or is its strength variable and is sometimes overwhelmed by the rest of the emission? If the iron line is variable, what is causing these changes? There is historical evidence of strong soft X-ray variability in Mrk 926 (Ghosh & Soundararajaperumal, 1992). The origin of the soft excess, and the physical process responsible for this variability is still unknown. In this study of Mrk 926, we make an effort to answer these open questions.

In this paper, we report the results from a 2009 *Suzaku* observation, a 2016 overlapping *XMM* and *NuSTAR* campaign, and a 2021 *NuSTAR* and *Swift -XRT* observation of Mrk 926. We analyze these multi-epoch spectra and shed more light on the physical processes that govern the central engine of this AGN. The next section tabulates the new observations and describes the data reduction. We then perform a detailed spectral analysis in Section 3.6. We subsequently discuss the results and their relevance for our understanding of Mrk 926 and other Seyfert-like AGN in Section 3.7. Finally, we summarize our findings in Section 3.8.

Table 3.1: The details of Mrk 926 X-ray observations used in this work.

Satellite	**ObsID**	**Date**	**Net Exposure**	**Epoch**
Suzaku	704032010	2009-12-02	139 ks	1
XMM-Newton	0790640101	2016-11-21	59 ks	2
NuSTAR	60201042002	2016-11-21	106 ks	2
	60761009002	2021-07-04	17 ks	3
Swift-XRT	00089294001	2021-07-04	2 ks	3

3.5 Observations and data reduction

3.5.1 Overview

In this paper, we analyze the broadband X-ray spectra of Mrk 926 observed in three different epochs (Laha & Ghosh, 2021; Rivers et al., 2011, this work). The first epoch is the 2009 *Suzaku* observation, the second epoch is the joint 2016 *XMM -NuSTAR* observation, and the third epoch is the 2021 *NuSTAR* (Harrison et al., 2013) observation with a *Swift* -XRT pointing. The details of these epochs are provided in table 3.1.

3.5.2 *Suzaku*

The observation was performed by the XIS 0/1/3 CCD cameras and the Hard X-ray Detector (HXD) Positive Intrinsic Negative (PIN) silicone diodes. Our data reduction method is similar to Rivers et al. (2011), which also studied this observation. We generated the cleaned event files with the *Suzaku* calibration database released on 2018 October 10. The source spectrum was selected from a circular region of 170 arcsec radius, while the background was from a circular source-free region of 125 arcsec. The ARFs and RMFs were generated using `xisarfgen` and `xisrmfgen` tasks, respectively. The HXD-PIN data were reduced with `aepipeline` task. We utilized the "tuned" background event files to

produce the non X-ray background spectra of HXD-PIN, to which the simulated cosmic X-ray background spectrum was added.

3.5.3 *XMM-Newton*

The *XMM-Newton* Observation data files (ODF) were processed using the *XMM-Newton* Science Analysis System (XMM-SAS v20.0). The MOS detector, operated in small window mode, is fully covered by the source photons and the selection of a source-free background region is not feasible. We thus focus our analysis on the EPIC-PN. The EPIC-PN data were first screened and periods of high particle backgrounds rejected. The spectra and light curves were created from the cleaned event files using `evselect`. We select an annular source region of 40 arcsec outer radius and 8 arcsec inner radius in order to mitigate mild pile-up. We also select a circular background region of 60 arcsec. Responses were created with `arfgen` and `rmfgen` tools. In `arfgen`, we apply the empirical correction of the EPIC effective area with the parameter `applyabsfluxcorr=yes`. This correction is essential to rectify the spectral shape mismatch seen with the simultaneous *NuSTAR* observation.

3.5.4 *NuSTAR*

The *NuSTAR* data from both detectors, FPMA and FPMB, were reduced using the standard pipeline (`NUPIPELINE`) of the *NuSTAR* Data Analysis Software (`NUSTARDAS` v2.1.1). Calibration files from *NuSTAR* `CALDB` v20210202 were used. We utilized the background filtering reports provided by the *NuSTAR* team to reduce the effect of high particle background and produce cleaned event files. We selected SAAMODE "optimized" and exclude the "tentacle" region minimizing the effect of the South Atlantic Anomaly (SAA) and optimizing exposure time and background level. We then extracted the spectra and light curves from a circular source region of 40 arcsec and a circular background region of 100 arcsec close to the source.

3.5.5 *Swift-XRT*

The *Swift -XRT* spectra were obtained using the *Swift -XRT* data products generator (Evans et al., 2009) supplied by the UK Swift Science Data Centre at the University of Leicester.

3.6 Spectral analysis

In section 3.5, we generated the multi-epoch X-ray spectra of Mrk 926 using *Suzaku* (2009), joint *XMM -NuSTAR* (2016) and joint *NuSTAR -Swift* (2021) observations. We bin them such that the detector resolution is over-sampled by a factor of 3, ensuring the minimum signal to noise ratio of 10, except for the *Swift* -XRT spectra which were binned to a minimum of 20 counts per bin. We use the energy range of 0.85–1.7 keV, 2.3–10.0 keV for XIS; 13.0–45.0 keV for PIN; 0.3–10.0 keV for PN; 3.0–75.0 keV for FPM; 0.3–10.0 keV for XRT. The resulting spectra are plotted in the top subplot of Figure 3.1 with further binning for clarity. We carry out the spectral analysis and model fitting with *XSPEC* 12.11.1 (Arnaud & A., 1996) using the chi-square minimization technique; all uncertainties are reported at 90% confidence.

In addition, our models always include: a cross correlation constant that accounts for any cross-calibration flux offsets among the different spectra in the same epoch; a galactic absorption component that accounts for the ISM absorption from our galaxy using the ISM absorption model `TBabs` (Wilms et al., 2000) with a column density ($N_{\rm H} = 2.86 \times 10^{20}$ cm^{-2}) obtained from the $\rm N_H$ Tool (Kalberla et al., 2005) using the latest HI4PI data. The cross-calibration constant for *Suzaku* -PIN is fixed at 1.16 which is the expected value for XIS-nominal pointing.

A power-law spectrum is a rough description of an AGN primary continuum in the X-ray band. Therefore to explore the additional X-ray components, We initially fit a power-law

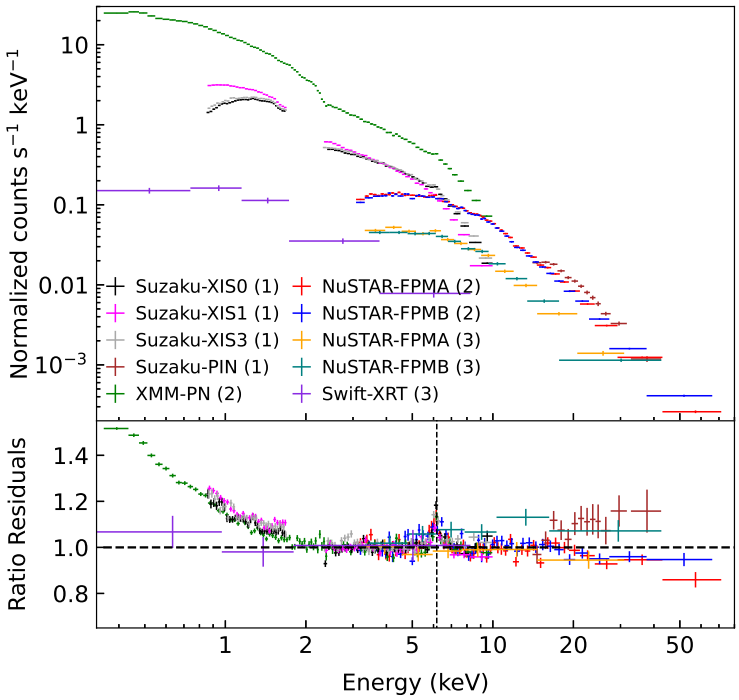

Figure 3.1: **Top:** All counts spectra for *Suzaku*, *XMM*, *NuSTAR* and *Swift-XRT* are shown; the spectra have been binned further for plotting. The number in brackets denote their respective epoch. **Bottom:** The ratio residuals after fitting the spectra with a power-law in the range of 3.0–5.0 keV. The dashed line indicates the neutral Fe-Kα energy.

to each epoch in the energy range 3–5 keV, where the spectra are likely dominated by the primary continuum. We then apply this model, without fitting, to the full energy range and search for residual features (Figure 3.1, bottom). The three epochs show variations in both low and hard end of the X-ray spectrum.

We notice smoothly-rising positive residuals towards the soft energies (<2 keV) indicative of a soft excess for Epoch 1 and 2. This could also be present in Epoch 3 but simply not resolved by *Swift-XRT*. We also observe a line-like feature at the neutral Fe-Kα energy. At higher energies (>15 keV), Epoch 2 shows a clear excess. These features can be associated with an X-ray reflection spectrum, which are the reprocessed hard X-ray photons from the hot corona after being backscattered off the AGN accretion disk or a distant reflector. This

reflection spectrum contains two main features: the 6.4 keV Fe-Kα line along with a bump-like feature that usually peaks around 25 keV. If this reflection occurs close to the black hole, these features can be relativistically smeared. In some cases, this relativistic reflection can explain the observed soft-excess (García et al., 2019). Thus, we check if the reflection scenario can adequately explain the broadband multi-epoch spectra of Mrk 926.

3.6.1 Dual reflection

AGNs are observed to be intrinsically variable in short timescales of a week or less. So in each epoch, we let the primary continuum to be different. However, we assume a stable reflecting medium between epochs as their variability timescale is generally much larger.

We model the primary continuum using the thermal Comptonization model `Nthcomp` (Życki et al., 1999). The powerlaw photon index (Γ) and its normalization is allowed to vary among different epochs. The disk-blackbody seed photon temperature ($\mathtt{kT}_{bb}$) is not sensitive to the fit and is fixed at 0.05 keV. The electron temperature (`kTe`) is a free parameter linked among epochs. For reflection off this primary continuum, we use `xillverCp` (Garcia et al., 2013) for the distant reflection from the outer disk and torus, and `relxillCp` (Garcia et al., 2014) for relativistic reflection. The reflection fraction for both are negative (reflection spectrum only) and variable among epochs while the Power-law photon index (Γ), normalization and Electron temperature (`kTe`) are linked to the primary continuum of the respective epoch. The inclination angle (`incl`) of both reflectors is linked and only allowed to vary between the range of 45°–55°. This inclination angle range was determined by Kollatschny et al. (2022) using high-cadence spectroscopic variability campaign of Mrk 926 in the optical band. The ionization parameter (`logxi`) of the distant reflector is fixed at 0 while it is a free parameter for the relativistic reflector. The iron abundance ($\mathtt{A}_{\mathtt{fe}}$) for both reflectors are free but not allowed to vary among epochs. For the relativistic reflection: the inner ($\mathtt{R}_{\mathtt{in}}$) and outer ($\mathtt{R}_{\mathtt{out}}$) radius of the accretion disk are fixed

at the innermost stable circular orbit (ISCO) and 400 R_g (gravitational radii) respectively; the emissivity index up to 15 gravitational radii is a variable parameter among epochs while the emissivity index beyond that is a free parameter linked among epochs; the spin of the black hole (`a`) is fixed at the maximum value of 0.998.

Due to the limited photon counts, we find some reflector parameters to be unconstrained for Epoch 3. Thus, we link all `relxillCp` parameters except the reflection fraction from Epoch 3 to Epoch 1. The fit for this dual reflection scenario is satisfactory with a chi-square of 1582 for 1143 degrees of freedom. We constrained the electron temperature (`kTe`) to > 284 keV; the iron abundance of the distant reflector to $5.0^{+2.3}_{-0.3}$ times the solar value; the iron abundance of the relativistic reflector to 1.6±0.4 times the solar value; the ionization parameter (`logxi`) to 2.70±0.02. The detailed parameter values of the fit are shown in Table 3.2. We note that the ratio residuals plot of this fit (Figure 3.2, top) shows that it cannot explain the data above 30 keV perfectly.

3.6.2 Warm corona

The soft-excess can also be modeled as a Comptonized emission from a separate component, often thought to be a warm and optically thick region called a warm corona (Petrucci et al., 2018). We investigate if such a warm corona-like component instead of a relativistic reflection can fit the multi-epoch spectra.

We retain the same model structure for the primary continuum and its distant reflection, and replace the relativistic reflection with a warm corona. We model the warm corona using the thermal Comptonization model `Nthcomp` (Życki et al., 1999). The Power-law photon index (Γ), the electron temperature (`kTe`) and the normalization for warm corona is allowed to vary among different epochs. The disk-blackbody seed photon temperature ($\mathtt{kT}_{bb}$) is fixed at 0.05 keV. Similar to Section 3.6.1, we find the warm coronal parameters to be unconstrained for Epoch 3. Thus, we link all except the normalization parameter from

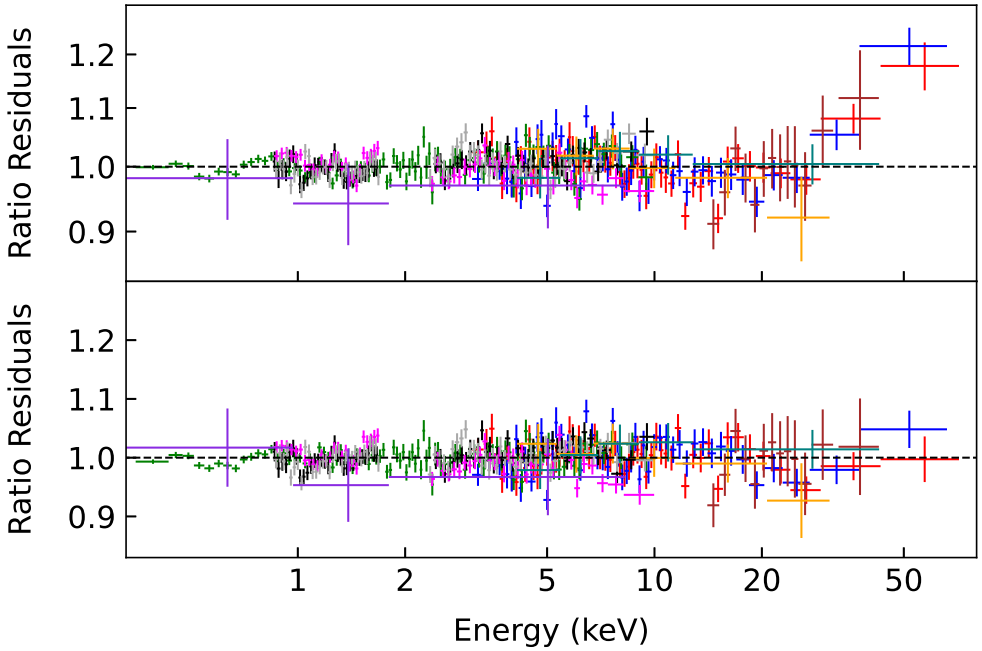

Figure 3.2: The top panel shows the ratio residuals for the dual reflection model fit in Section 3.6.1; the bottom panel shows the ratio residuals for the warm corona model fit in Section 3.6.2. The colors represent the same spectra as Figure 3.1.

Epoch 3 to Epoch 1. This model fits data well with a chi-square of 1479 for 1139 degrees of freedom. We constrained the electron temperature of the hot corona to 39±9 keV; the iron abundance of the non-relativistic reflector to > 8.4 times the solar value. The detailed parameter values of the fit are shown in Table 3.3. The ratio residuals plot of this fit (Figure 3.2, bottom) shows that this model explains the data above 30 keV better than the dual reflection scenario. We note that this fit is slightly better with the inclusion of additional narrow Gaussian lines in the *XMM* spectra, but for simplicity these were omitted as the results are unaffected.

3.6.3 Mrk 926 at Lower Frequencies

Using the Karl G. Jansky Very Large Array (VLA) observations at 4.8 GHz with arcsec resolution, Ulvestad & Wilson (1984) found Mrk 926 to be a relatively powerful radio source

Table 3.2: Spectral parameters for the dual reflection model (Section 3.6.1) containing the primary continuum, distant reflection and relativistic reflection fitted to the multi-epoch data. L1 denotes that the parameter is linked to the respective Epoch 1 parameter whereas f means the parameter is fixed at the given value.

Model	**Parameter description**	**Symbol (Units)**	**Epoch 1**	**Epoch 2**	**Epoch 3**
Primary Continuum (nthcomp)	Photon Index	Γ	1.83±0.06	1.88±0.05	1.73±0.04
	Electron Temperature	`kTe` (keV)	>284	L1	L1
	Normalization	`norm` (10^{-3})	14.1±0.2	12.2±0.2	4.8±0.3
Distant Reflection (xillverCp)	Iron Abundance	`Afe` (solar)	$5.0^{+2.3}_{-0.3}$	L1	L1
	Ionization parameter	`logxi` (ergs $\mathrm{cm}^{-}2\,\mathrm{s}^{-1}$)	0^f	L1	L1
	Inclination	`incl` (°)	53±2	L1	L1
	Reflection fraction	`refl_frac` (-10^{-3})	3.0±0.4	5.5±0.6	7.4±3.5
Relativistic Reflection (relxillCp)	Inner emissivity index	`Index1`	4.5±0.3	>9.8	L1
	Outer emissivity index	`Index2`	>4.0	L1	L1
	Inner-outer break	`Rbr` (gravitational radii)	15^f	L1	L1
	Spin of the black hole	`a`	0.998^f	L1	L1
	Inner radius	`Rin` (ISCO)	1^f	L1	L1
	Outer radius	`Rout` (gravitational radii)	400^f	L1	L1
	Ionization parameter	`logxi` (erg $\mathrm{cm}^{-2}\,\mathrm{s}^{-1}$)	2.70±0.02	L1	L1
	Iron Abundance	`Afe` (solar)	1.6±0.4	L1	L1
	Reflection fraction	`refl_frac` (-10^{-3})	6.1±0.5	8.4±0.3	>6.4

Table 3.3: Spectral parameters for the warm corona model (Section 3.6.2) the primary continuum, distant reflection and a warm corona fitted to the multi-epoch data. L1 denotes that the parameter is linked to the respective Epoch 1 parameter whereas f means the parameter is fixed at the given value.

Model	**Parameter description**	**Symbol (Units)**	**Epoch 1**	**Epoch 2**	**Epoch 3**
Primary Continuum (nthcomp)	Photon Index	Γ	1.69±0.01	1.77±0.01	1.70±0.02
	Electron Temperature	`kTe` (keV)	39±9	L1	L1
	Normalization	`norm` (10^{-3})	12.7±0.5	13.1±0.1	4.8±0.2
Distant Reflection (xillverCp)	Iron Abundance	`Afe` (solar)	>8.4	L1	L1
	Ionization parameter	`logxi` ($\mathrm{ergs\,cm^{-}2\,s^{-1}}$)	0^f	L1	L1
	Inclination	`incl` (°)	<55	L1	L1
	Reflection fraction	`refl_frac` (-10^{-3})	2.6±0.4	2.3±0.4	4.6±2.2
Warm Corona (nthcomp)	Photon Index	Γ	2.84±0.1	2.63±0.1	L1
	Electron Temperature	`kTe` (keV)	>0.85	0.23±0.02	L1
	Normalization	`norm` (10^{-3})	4.3±0.6	1.5±0.2	<0.16

for a type 1 Seyfert with an unresolved core. Mundell et al. (2000) studied the high angular resolution (∼2 mas) radio continuum observations of Mrk 926 using the Very Long Baseline Array (VLBA) at 8.4 GHz. They found the core to be unresolved with brightness temperature in excess of 10^8 K and size less than 1 pc. They found the radio core to be consistent with a non-thermal synchrotron self-absorption region without a Doppler boost. Mrk 926 was also monitored at 22 GHz with 1 arcsec resolution by the VLA (Smith et al., 2020). Using these past radio observations at arcsec or sub-arcsec resolution and additional archival flux measurements at other bands from Far-IR up to X-rays, we study the nature of the self-absorbed synchrotron core.

We use the online Spectral SED builder tool[1] to generate an spectral energy distribution (SED) using archival flux measurements of Mrk 926. The SED is shown in Figure 3.3. We find the radio SED to be consistent with a power-law with a steep spectral slope ($F_\nu \propto \nu^{-0.54}$) which is indicative of an optically-thin component (Eckart et al., 1986).

In the optical reverberation mapping of Mrk 926 (Kollatschny et al., 2022), a Balmer satellite component, consistent with the presence of a compact jet, was found. A compact jet is continually-accelerated along the jet, where we detect single synchrotron spectra from different distances along the jet resulting in a flat to slightly inverted radio spectrum at GHz frequencies (Blandford & Königl, 1979; Panessa et al., 2019). The flat/inverted radio spectrum will break at some higher frequency ν_b, either at the particle acceleration region in a shocked zone or the base of the jet, into a steep spectrum (Blandford & Königl, 1979; Koljonen et al., 2015).

There could be an underlying compact jet in Mrk 926 with the break frequency present at MHz or higher frequencies. This jet structure, if present, could be identified at higher spatial resolutions. However, with the available archival data, we cannot postulate the origin

[1]The SED builder is an online tool dedicated to multi-frequency data visualization, together with fitting routines useful for extracting refined scientific products. Provided by the Space Science Data Center (SSDC): http://www.ssdc.asi.it

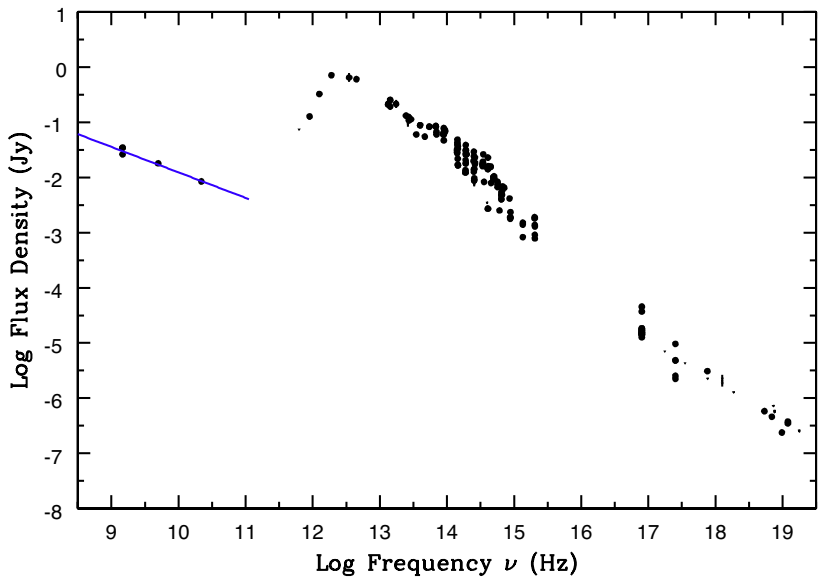

Figure 3.3: The SED generated by the online SED builder tool[1] for Mrk 926 using archival flux measurements. The blue line is a power-law fit to the arcsec or higher resolution radio data.

of this radio emission. A future multi-wavelength observing campaign of Mrk 926 including higher spatial resolution radio observations at multiple frequencies is highly desired to study it in detail. This will allow us to perform a full SED modeling including the disk, host-galaxy etc. without the complications from variability, and resolve this structure.

3.7 Discussion

3.7.1 Comparison with results from previous X-ray studies

Historically, Mrk 926 has been observed to show flux variations on longer timescales (months and years). Using data from various X-ray satellites covering more than 20 years (1977–1999), Choi et al. (2002) reported the X-ray continuum flux variations in Mrk 926. We update their observed 2-10 keV X-ray flux variations plot (see Figure 3.4). We find that Mrk 926 still shows significant continuum variability.

Additionally, Mrk 926 also shows variations in its iron line profile (Bianchi et al., 2004;

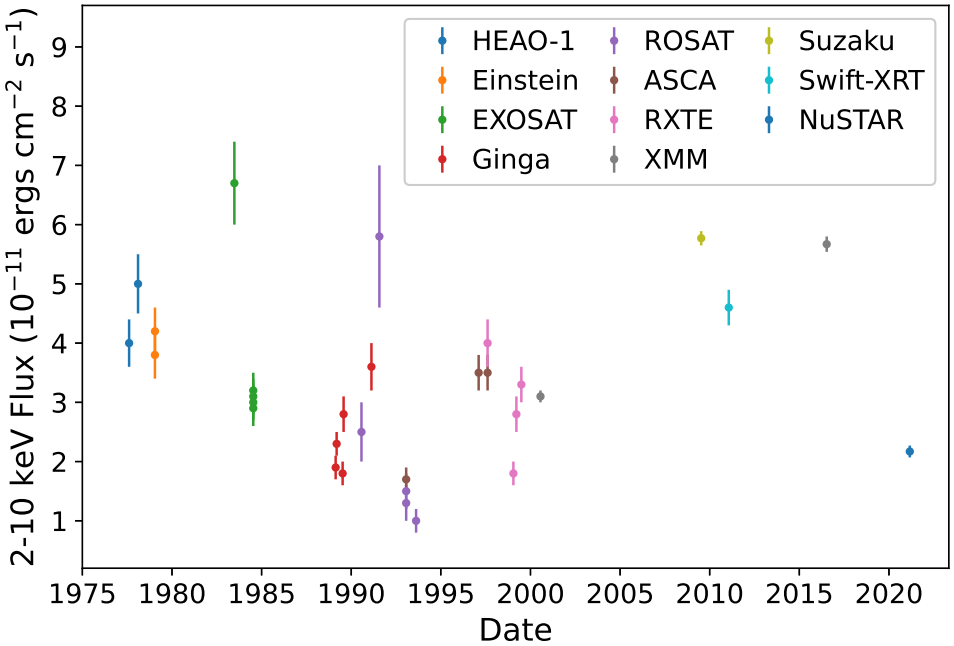

Figure 3.4: Historic 2–10 keV flux variation plot adapted from Choi et al. (2002) and updated with recent values.

Weaver et al., 2001). Choi et al. (2001), using ROSAT and ASCA archival data, found the line profile dominated by a broad component. Bianchi et al. (2004), using a ∼7 ks *XMM* and a simultaneous BeppoSAX observation, found the presence of a Fe Kα and a Fe XXVI line. Meanwhile Rivers et al. (2011), using Suzaku observation, found the need for Fe Kα, Kβ, and an Fe K shell absorption edge to explain the observed line profile, and concluded that a broad component, if present, must be weak.

The 2009 *Suzaku* observation (Epoch 1) were described by Rivers et al. (2011) using a torus model and an additional power-law component for soft excess. The torus was found to have subsolar iron abundance with a column density, $\log(N_H)$ of 24.55±0.15 while the inclination angle and the covering factor was fixed to 30° and 0.5 respectively. The same observation was used by Noda et al. (2013) to study the nature of soft excess in Mrk 926 using intensity-correlated spectral analysis. They found that the thermal Comptonization

interpretation can explain the broadband *Suzaku* data including the soft excess, while the relativistic reflection interpretation was failed to explain it. This is in agreement with our results in Section 3.6.1 and 3.6.2.

The 2009 *Suzaku* and 2016 *XMM -NuSTAR* observations (Epoch 1 and 2) were studied by Laha & Ghosh (2021). They modeled the soft excess with just the relativistic reflection and found that between two epochs: the primary continuum is constant both in photon index and luminosity; the soft excess flux decreases by a factor of 2; the Compton hump vanishes; the narrow Fe-kα line becomes marginally broad and its flux doubles. They argue since the primary continuum does not change but the Compton hump vanishes between two epochs, the reprocessing medium must be changing. They speculate that this could be explained by a dynamic torus where the equatorial toroidal disk produces the narrow Fe-kα emission while the outflowing component generates the variable Compton hump.

To explore this hypothesis, we replace `xillverCp` with a torus reprocessor model `borus12` (Baloković et al., 2018) in our multi-epoch analysis. Assuming either a stable or a variable torus structure between epochs, we find minimal changes to the fit and still see a small $> 30\,\mathrm{keV}$ excess in the dual reflection scenario. For the warm corona scenario, we can get a fit similar to our best fit with a stable torus reprocessor. Additionally, recent simulations show that the outflowing component of the torus can change the equivalent width of some X-ray fluorescent lines but does not significantly influence the X-ray spectra (McKaig et al., 2022). Thus, we deem the scenario presented in Laha & Ghosh (2021) to be unlikely considering the warm corona/dual reflection model with a distant reflector, either torus or an accretion disk can describe the multi-epoch broadband X-ray spectra of Mrk 926 without requiring significant changes to the reprocessor between epochs.

3.7.2 Soft excess Origin

Recent studies debate two possible origins of AGN soft excess: the relativistic ionized reflection of the continuum from the inner accretion disk, and the Comptonization of the accretion disk photons in an optically thick, warm corona (e.g. García et al., 2019; Petrucci et al., 2013).

There are many AGN for which the relativistic reflection origin of soft excess works well (e.g. Jiang et al., 2019; Mallick et al., 2018; Middei et al., 2020). In this scenario, the extreme gravitational blurring blends the rich forest of fluorescent emission lines produced by the reprocessing of X-ray photons in the innermost regions of accretion disk creating a smooth soft excess. However, this scenario requires extreme parameters, such as maximum black hole spin, a very low and compact hot corona, and a very high density for the inner accretion disk (García et al., 2019). From Section 3.6, we find that the relativistic reflection struggles to describe the broadband X-ray spectra of Mrk 926 well above 30 keV. This could either mean that the soft excess in Mrk 926 is not due to the relativistic reflection alone or that our simplistic reflection modeling still has shortcomings.

Testing the warm coronal origin of soft excess in a sample of 22 unabsorbed radio-quiet AGN with combined 100 observations, Petrucci et al. (2018) found it to be a good description to more than 90% of the sample with the warm coronal temperature in the range $\sim 0.1 - 1\,\mathrm{keV}$, and the optical depth in $\sim 10 - 40$ range. However, at these temperatures and optical depth, the atomic opacities is likely to dominate over the Thomson opacities and create strong absorption features instead of a smooth soft excess (García et al., 2019). This would also lead to rapid cooling of the warm corona, requiring a well-tuned heating process that constantly offsets this (Ballantyne, 2020; Ballantyne & Xiang, 2020). Petrucci et al. (2020) studied the radiative equilibrium and emission of a warm corona in the presence of an internal heating source and found that if this corona is covering a large part of a weakly dissipative accretion disk, it can generate emission matching the observed soft-excess. One

such source of internal heating could be the presence of magnetized accretion flow.

From Section 3.6, we find that the warm corona model can model the broadband X-ray spectra of Mrk 926 in all three epochs well at all energies. Thus, it is certainly a possibility for the soft excess origin in this source. To make a strong statement about the nature of the soft excess in this source, high quality data covering the 50-100 keV range would be needed. Finally, we note that since we are unable to constrain the nature of radio emitter at high frequencies, we cannot fully exclude any flux contribution at soft X-rays.

3.8 Summary

We present results of a broadband X-ray study of Mrk 926 using the 2009 *Suzaku* (Epoch 1), 2016 *XMM -NuSTAR* (Epoch 2), and 2021 *NuSTAR -Swift -XRT* (Epoch 3) observations. Our findings can be summarized as follows:

1. Mrk 926 is a variable AGN. The unabsorbed 2-10 keV luminosity of Mrk 926 is $2.9\pm0.1 \times 10^{44}\,\mathrm{erg\,s^{-1}}$ (Epoch 1 and 2) and $1.1\pm0.1 \times 10^{44}\,\mathrm{erg\,s^{-1}}$ (Epoch 3).

2. We found the broadband spectra of Mrk 926 show a primary continuum, a soft excess and distant reflection. If the soft excess is modeled using relativistic reflection, we find some residuals above 30 keV. We find no such residuals if we describe soft excess as a thermally Comptonized emission from a optically-thick warm corona.

3. An optical Balmer satellite component was found in previous study of Mrk 926 which suggests the presence of a compact jet. The signature of a compact jet in radio band is the presence of a flat/inverted spectrum that breaks at some higher frequency to a steep spectrum. We found a steep radio spectrum in the archival SED of Mrk 926. Thus, the archival radio data cannot confirm the presence of a compact jet.

Future multi-wavelength observing campaign including a high spatial resolution radio observation is highly desired to study the origin of this radio emitter in the 'bare' Seyfert Mrk 926.

Acknowledgements

This work made use of data from the NuSTAR mission, a project led by the California Institute of Technology, managed by the Jet Propulsion Laboratory, and funded by the National Aeronautics and Space Administration. This research has also made use of the NASA/IPAC Extragalactic Database (NED), which is funded by the National Aeronautics and Space Administration and operated by the California Institute of Technology. We would like to thank Javier García and Andy Fabian for helpful discussions.

Data Availability

All the data used in this article are publicly available from ESA *XMM-Newton* Science Archive (XSA; http://nxsa.esac.esa.int/) and NASA High Energy Astrophysics Science Archive Research Center (HEASARC; https://heasarc.gsfc.nasa.gov/). The reduced data products used in this work may be shared on reasonable request to the authors.

CHAPTER FOUR

A MULTI-WAVELENGTH STUDY OF THE OBSCURING STRUCTURE OF THE POLAR-SCATTERED SEYFERT 1 GALAXIES

4.1 Contribution of Authors and Co-Authors

Manuscript in following chapter

Author: S. Chalise

Contributions: Conceived the study design. Implemented study design. Wrote first draft of manuscript.

Author: A. M. Lohfink

Contributions: Conceived the study design. Observation proposer. Provided feedback on manuscript drafts.

Author: A. Tanimoto

Contributions: Provider/Creator of the analytic model XCLUMPY.

Author: E. Carmichael

Contributions: Help on the infrared data reduction. Provided feedback on manuscript drafts.

4.2 Manuscript Information

S. Chalise, A. M. Lohfink, A. Tanimoto, E. Carmichael

Monthly Notices of the Royal Astronomical Society

Status of Manuscript:
_X_ Prepared for submission to a peer-reviewed journal
____ Officially submitted to a peer-reviewed journal
____ Accepted by a peer-reviewed journal
____ Published in a peer-reviewed journal

Oxford University Press

4.3 Abstract

Despite being a vital structure in the context of galactic evolution, the supermassive black hole environment, including the clumpy torus, is not well understood. The penetrative X-rays from the central engine and the infrared dust emission can map these complex structures. Polar-scattered Seyfert 1 galaxies (PSS) are moderately inclined AGN with 12 known sources and a lot of archival data. Our study investigates their torus structure using, often multi-epoch, broadband X-ray spectra along with the available infrared spectral and photometric data with a multi-wavelength torus model. We find that this multiwavelength approach provides better constraints than studies limited to either X-ray or IR, and is able to break degeneracies in parameter space. We do not find a clear link that can describe/predict the IR torus structure from the X-ray parameters, and vice versa. We also find the covering factor of the PSS tori does not follow the predictions of the radiation-regulated unification scheme. The results suggest a complex and varied distribution of gas and dust in Seyfert tori.

4.4 Introduction

The circumnuclear dusty gas structure surrounding an accreting supermassive black hole (SMBH) also referred to as the "torus" is a key part of any AGN unification model. This torus feeds material onto the SMBH from the host galaxy facilitating their coevolution (Heckman & Best, 2014), thus making them a vital structure in the context of galactic evolution. The torus can be directly probed either in X-rays, which trace the intercepting gas and dust over a wide range of temperature, or in the infrared which provides information on the warm/hot dust. Recent observations, especially in the infrared, advocate the need for the torus to be clumpy and stabilized by frequent cloud-cloud collisions or by radiation pressure (Netzer, 2015). Variability of the neutral X-ray absorption column, seen in AGN spectra on the

timescale of days to years further supports the non-uniform nature of the torus (Markowitz et al., 2014; Ramos Almeida et al., 2009). Despite promising recent developments, our understanding of the SMBH surrounding is still limited.

X-ray observations of AGN are a great way to study the AGN surrounding because the primary X-ray continuum interacts and therefore is modified by the circumnuclear material. The primary X-ray photons are absorbed along the line-of-sight (LOS) and are reflected off the accretion disk and torus. The resulting torus reflection spectrum contains the information on the torus structure (Fabian, 1996; Liu et al., 2016). As an example, the reflection strength and shape along with the structure of the Fe kα line strongly depend on the angular width of the torus and the global column density of the torus (Buchner et al., 2019; Ikeda et al., 2009). Also, photoelectric absorption features of the reflection component constrain the overall torus geometry and inclination angle (Baloković et al., 2018; Liu & Li, 2014; Tanimoto et al., 2019).

Torus properties like the covering factor and LOS column density have been constrained in several Seyfert 2 galaxies (e.g NGC 4388 Kamraj et al., 2017). Marchesi et al. (2019), found a potential inverse trend between torus covering factor and 2-10 keV luminosity using 35 candidate Compton-thick AGN (Hydrogen column density, $N_H \geq 10^{24}$ cm^{-2}). Tanimoto et al. (2020) studied the broadband X-ray spectra of 10 obscured AGN and found that the torus angular width obtained from infrared spectra were systematically larger than those obtained from their analysis of X-ray data. This discrepancy was attributed to the contribution of dusty polar outflows to the infrared flux. A similar study that also included some unobscured AGN was done by Ogawa et al. (2021) which confirmed the results by Tanimoto et al. (2020) and provided an updated unified picture of AGN structure including a dusty torus, dusty polar outflows, and dust-free gas, where the inclination determines the X-ray and optical classifications and observed torus properties in the X-ray and infrared bands. However increasing the sample size of less obscured AGN ($N_H < 10^{23}$ cm^{-2}) is vital in order to remove a possible bias towards obscured AGN and test whether the relation

between Eddington ratio (the AGN luminosity normalized by the black hole mass) and torus covering factor extends to less obscured sources. Only detailed studies of tori throughout the entire parameter-space of Seyfert galaxies can lead to a complete unifying picture for all AGN. This is challenging as the reflection features in less obscured AGN are diluted by the strong primary continuum.

However, a subgroup of Seyferts, the Polar-scattered Seyfert 1 galaxies (PSS), in which the line-of-sight passes through the torus edge are good targets to study less obscured AGN tori as their peculiar orientation means they show strong torus features in their spectra while being less obscured than a Seyfert 2. PSS (<10% of all Seyferts (Smith et al., 2004) are thought to be a link between Seyfert 1 and 2 galaxies. Although their optical spectrum is similar to Seyfert 1, their optical polarization spectrum is that of a Seyfert 2. This is due to the equatorial-scattered component being obscured by the torus while the polar-scattered component remains unchanged. Additionally, X-ray absorption is prevalent among PSS which can be partly attributed to the torus clouds. But being moderately inclined local Seyferts, PSS sources also show a pattern of complex absorption structures from ionized clouds called warm absorbers which impart their signatures on the soft X-ray spectrum (Laha et al., 2014; Reynolds & Fabian, 1995). Knowing the location, properties and dynamics of these warm absorbers can further elucidate the structure of the SMBH environment. For example, several theoretical models have been proposed that describe the broad-line region and the torus as one continuous structure (e.g. disk wind model: Elitzur & Ho, 2009). Using coordinated X-ray observations of a PSS, NGC 3227, Turner et al. (2018) found consistent outflow velocities for its three zone warm absorber, supporting the view that all three absorbers despite being at different distances from the nucleus are a part of the same complex cloud structure. Similar results were found by Miniutti et al. (2014) and have confirmed the clumpy nature of the torus and dynamic absorbing structures in another PSS (ESO 323-G77) using multi-epoch X-ray spectra. Thus, PSS are the ideal sources to study

Table 4.1: Basic Information of our Sample with archival black hole mass estimates.

Source	**RA**	**Dec**	**Redshift**	$\log \mathbf{M_{BH}}(\mathbf{M_\odot})$
NGC 3227	155.877	+19.865	0.004	6.68±0.10 (De Rosa et al., 2018)
NGC 4593	189.914	-5.344	0.009	6.98±0.10 (Denney et al., 2006)
Mrk 766	184.610	+29.813	0.013	6.02±0.33 (Giacchè et al., 2014)
Fairall 51	281.225	-62.365	0.014	6.84±0.30 (Wang & Zhang, 2007)
ESO 323-G077	196.609	-40.415	0.015	7.39±0.30 (Wang & Zhang, 2007)
Mrk 1239	148.080	-1.612	0.020	6.11±0.30 (Greene et al., 2006)
Was 45	181.180	+31.177	0.025	7.05±0.30 (Liu et al., 2019)
Mrk 704	139.608	+16.305	0.029	7.55±0.10 (De Rosa et al., 2018)
Mrk 1218	129.545	+24.895	0.029	6.90±0.30 (Liu et al., 2019)
Mrk 231	194.060	+56.874	0.042	8.18±0.30 (Yan et al., 2015)
IRAS 15091-2107	227.999	-21.317	0.045	7.00±0.30 (Ohta et al., 2007)
Mrk 376	108.563	+45.699	0.056	8.17±0.10 (Kamraj et al., 2018)

the whole circumnuclear structure in less-obscured ($N_H \sim 10^{21-23}$ cm^{-2}) AGN.

To be able to learn more about the clumpy torus and associated circumnuclear environment of sources with lower obscurations, we study the most complete sample of PSS found using spectropolarimetric observations by Smith et al. (2004). These sources and their basic properties are tabulated in Table 4.1. In this paper, we test the clumpy torus scenario in this PSS sample in both X-rays and the infrared using a joint multi-wavelength torus model and present our findings.

4.5 Observations and Data Reduction

For the study of the circumnuclear obscuring structure of these 12 Polar-scattered Seyfert 1 galaxies, we analyze their available X-ray and infrared spectra. Most of these spectra are archival but several are presented here for the first time. We searched for all available *XMM-Newton* (Section 4.5.1.1), *NuSTAR* (Section 4.5.1.2), *Suzaku* (Section 4.5.1.3), and Spitzer (Section 4.5.2.1) data. We also utilized the sources' *Swift* /XRT (Section 4.5.1.4) spectra, especially when no other soft X-ray data were available. We include Wise (Section 4.5.2.3) and Herschel (Section 4.5.2.2) photometric data in order to remove possible non-AGN contamination from the host-galaxy. Finally, if the source was not observed by Herschel, we utilized AKARI (Section 4.5.2.4) photometry.

Although we tried to utilize all available data, we had to exclude some observational epochs. For example, we exclude some of the *XMM* and *NuSTAR* observations of NGC 3227 and Mrk 766 due to high variability and complex occulation events respectively which could not be resolved without significant increase in complexity of the multi-epoch model. All the observations used in this paper is tabluated in Table 4.2. We now describe the data reduction process used for each satellite.

4.5.1 X-ray

4.5.1.1 *XMM-Newton* The X-ray spectra of *XMM*-Newton cover the energy range from 0.3-10 keV. To obtain spectra, the *XMM-Newton* Observation data files (ODF) were processed using the *XMM-Newton* Science Analysis System (XMM-SAS v18.0). We use only the EPIC-PN data as the MOS data were not available for all observations. The EPIC-PN data were first screened and periods of high particle backgrounds rejected. We also checked for pile-up using `epatplot` and found none. The spectra were created from the cleaned event files using `evselect`. We select a circular source region of 30 arcsec radius. We also select

a circular source-free background region between 45 and 80 arcsec radius depending on the detector image. Responses were created with `arfgen` and `rmfgen` tools.

4.5.1.2 *NuSTAR* The *NuSTAR* data from both detectors, FPMA and FPMB, were reduced using the standard pipeline (`NUPIPELINE`) of the *NuSTAR* Data Analysis Software (`NUSTARDASv1.8.0`). Calibration files from *NuSTAR* `CALDB v20210202` were used. We utilized the background filtering reports provided by the *NuSTAR* team to reduce the effect of high particle background and produce cleaned event files. We selected SAAMODE "optimized" and exclude the "tentacle" region minimizing the effect of the SAA and optimizing exposure time and background level. We then extracted the spectra from a circular source region of 40 arcsec and a circular background region between 80 to 100 arcsec radius close to the source. The resulting spectra cover the energy range from 3.0-78.0 keV or until the energy where the source becomes too faint to be detected above the background.

4.5.1.3 *Suzaku* We generated the cleaned event files for both the soft X-ray XIS detector and the hard X-ray HXD detector with the *Suzaku* calibration database released on 2018 October 10. The source spectrum was selected from a circular region of 170 arcsec radius, while the background was from a circular source-free region between 120 to 170 arcsec excluding regions of nearby sources. The ARFs and RMFs were generated using `xisarfgen` and `xisrmfgen` tasks, respectively. The HXD-PIN data were reduced with `aepipeline` task. We utilized the "tuned" background event files to produce the non X-ray background spectra of HXD-PIN, to which the simulated cosmic X-ray background spectrum was added.

4.5.1.4 *Swift* The *Swift* /XRT soft X-ray spectra were generated by using the UK Swift Science Data Centre Website (Tyler et al., 2006), which builds usable spectra using `HEASOFT v6.29` (Nasa High Energy Astrophysics Science Archive Research Center (Heasarc), 2014). We do not utilize BAT spectra in this work as significantly higher quality hard X-ray spectra

are available.

4.5.2 Infrared

4.5.2.1 Spitzer The *Spitzer* Infrared Spectrograph (IRS) observations can contain low and high resolution spectra at mid-infrared wavelengths (from 5 – 40 microns). If both high and low resolutions are present, we use both. The *Spitzer* spectra were extracted from the Combined Atlas of Sources with *Spitzer* -IRS Spectra (CASSIS Lebouteiller et al., 2015). From this publicly available CASSIS spectral database, we downloaded the available spectra generated using their optimal extraction method.

4.5.2.2 Herschel The *Herschel* -PACS photometry for the blue (70 micron) and red (160 micron) bands was extracted from the "*Herschel* high level images" products of the NASA/IPAC Infrared Science Archive (IRSA) database using the method described in Bernhard et al. (2021). The *Herschel* -SPIRE data was ignored as it was only available for few sources in our sample and is not essential for analysis.

4.5.2.3 Wise The *Wise* photometry (3.4, 4.6, 12 and 22 micron bands) was obtained from the All-*Wise* catalogue (Wright et al., 2010) in NASA/IPAC Infrared Science Archive (IRSA) database.

4.5.2.4 AKARI The *AKARI* photometry was also obtained from the NASA/IPAC Infrared Science Archive (IRSA) database.

Table 4.2: Details of the utilized observational spectra including the Observation ID and the net exposure in kilo-seconds of the specific X-ray/Infrared detector is shown.

Source	***Satellite (Detector)***	***ObsID***	***Net Exposure (ks)***
NGC 3227	XMM-Newton (PN)	0101040301	29.7
		0400270101	93.6
		0782520201	50.8
		0782520501	48.4
		0782520601	59.6
		0844341401	34.9
	NuSTAR (FPMA/B)	60202002002	48.9/49.2
		60202002008	40.2/40.1
		60202002010	39.9/40.1
		60202002014	44.7/44.4
		80502609004	26.9/27.0
	Suzaku (XIS/HXD)	703022010	47.5/47.9
		703022020	40.1/46.4
		703022030	43.9/46.6
		703022040	52.3/43.4
		703022050	69.2/37.2
		703022060	46.0/36.5
	Spitzer	4934656	
NGC 4593	XMM-Newton (PN)	0109970101	8.3
		0059830101	53.3
		0740920201	16
		0740920301	11.8

Table 4.2 continued from previous page

NGC 4593	XMM-Newton (PN)	0740920401	17.2
		0740920501	15.1
		0740920601	19.9
		0784740101	98.5
	NuSTAR (FPMA/B)	60001149002	22.2/22.1
		60001149004	20.6/20.9
		60001149006	20.2/20.1
		60001149008	22.1/22.4
		60001149010	21.1/21.1
	Suzaku (XIS/HXD)	702040010	99.4/100.7
		709014010	22.0/22.7
		709014020	27.1/28.6
		709014030	29.9/-
		709014040	106.4/-
		709014050	112.7/-
	Spitzer	4853504	
Mrk 766	XMM-Newton (PN)	0096020101	36.2
		0304030301	68.9
		0304030401	65.8
		0304030501	64.6
		0304030601	60.6
		0304030701	20.1
		0763790401	19.5
	NuSTAR (FPMA/B)	60001048002	89.1/88.7

Table 4.2 continued from previous page

Mrk 766	NuSTAR (FPMA/B)	60101022002	20.3/20.3
	Suzaku (XIS/HXD)	701035010	87.1/88.8
		701035020	39.7/47.2
	Spitzer	14448896	
Fairall 51	XMM-Newton (PN)	0300240401	1.7
		0300240901	1.5
	NuSTAR (FPMA/B)	60402014002	62.5/62.3
		60402014004	29.2/29.1
		60402014006	29.0/28.2
	Suzaku (XIS/HXD)	708046010	23.9/23.4
		708046020	22.8/21.9
		708046030	21.8/32.9
		708046040	23.4/34.3
	Spitzer	26489088	
ESO 323-G077	XMM-Newton (PN)	0300240501	20.6
		0694170101	94.5
	NuSTAR (FPMA/B)	60202021002	38.3/38.2
		60202021004	41.4/41.4
		60202021006	42.6/42.0
		60202021008	42.2/42.2
		60202021010	37.6/37.9
	Swift-XRT	00081842001	1.9
		00081842002	1.9
		00035598007	1.4

Table 4.2 continued from previous page

ESO 323-G077	Swift-XRT	00081842006	1.6
	Spitzer	18942720	
Mrk 1239	NuSTAR (FPMA/B)	60360006002	20.9/20.8
	Suzaku (XIS/HXD)	702031010	50.1/-
	Spitzer	14450176	
Was 45	XMM-Newton (PN)	0601780601	20.4
	NuSTAR (FPMA/B)	60601035002	76.6/76.0
	Spitzer	10870272	
Mrk 704	XMM-Newton (PN)	0300240101	14.8
		0502091601	66.3
	NuSTAR (FPMA/B)	60061090002	21.5/21.5
	Spitzer	17954560	
Mrk 1218	XMM-Newton (PN)	0302260201	6.6
		0302260401	4.5
	NuSTAR (FPMA/B)	60601034002	72.4/71.8
	Swift-XRT	00089161001	2.6
	Spitzer	10869760	
Mrk 231	XMM-Newton (PN)	0081340201	17.2
		0770580401	18.8
		0770580501	20.9
	NuSTAR (FPMA/B)	60002025002	40.4/40.2
		60002025004	28.0/27.8
		90102001002	31.0/31.1
		90102001004	27.1/27.1

Table 4.2 continued from previous page

Mrk 231	NuSTAR (FPMA/B)	90102001006	30.1/30.0
		80302608002	80.0/80.1
	Suzaku (XIS/HXD)	706037010	15.7/-
	Spitzer	22157312	
IRAS 15091-2107	XMM-Newton (PN)	0300240201	5.6
	NuSTAR (FPMA/B)	60061262002	21.1/20.8
	Suzaku (XIS/HXD)	706010010	69.9/75.9
	Spitzer	17956096	
Mrk 376	NuSTAR (FPMA/B)	60160288002	23.5/23.7
	Swift-XRT	00081006001	2.7
		00081006002	3.6

4.6 Model Description

In this study, we test the clumpy torus scenario on our sample of Polar-scattered Seyfert 1 galaxies. In this section, we describe the spectral models and components used to adequately explain the observed broadband X-ray and infrared data.

4.6.1 Clumpy Torus

There are overwhelming evidence that the dust in AGN tori is distributed in compact, dense clumps rather than a homogeneous distribution (Markowitz et al., 2014; Ramos Almeida et al., 2009). The torus is considered clumpy when the mean free path between clumps greatly exceeds the clump size (Nenkova et al., 2008b).

Nenkova et al. (2008a,b) constructed an infrared clumpy torus model which has been successfully applied to the infrared spectral energy distributions of many AGN (Lira et al.,

2013; Ramos Almeida et al., 2014). Adopting the same geometry, Tanimoto et al. (2019) constructed an X-ray clumpy torus model, which also has been used to describe the X-ray spectra of many local AGN (Tanimoto et al., 2020, 2022). We will use these two models, CLUMPY and XCLUMPY, as their identical geometry allows a direct comparison of the results obtained from the infrared and X-ray spectral modeling.

Both models assume a torus made up of many clumps distributed in a powerlaw distribution in the radial direction, and in a normal distribution in the elevation direction. The IR model traces the spatial distribution of the dust whereas the X-ray model traces both dust and gas. Despite a similar torus geometry, the parameters shaping the spectra in these two wavebands are markedly different. The IR flux traces emission from the entire torus whereas in X-rays, primarily the line-of-sight emission is captured.

A cartoon representing the basic geometry of the clumpy torus is shown in Figure 4.1, important geometrical parameters are also indicated in the sketch. The X-ray torus model (`XCLUMPY`) has three main modeling parameters: $\mathtt{N_{H,Eq}}$, the total hydrogen column density along the equatorial plane; σ, the torus angular width; and `i`, the inclination angle. Similarly, the infrared torus model (`CLUMPY`) has six major parameters: $\mathtt{N_0}$, the number of dust clumps along the equatorial plane; `Y`, the ratio of the outer radius ($\mathtt{R_{out}}$) to the inner radius ($\mathtt{R_{in}}$); `q`, the index of the radial density profile (e.g. a steep index indicates that the clumps are concentrated near the inner edge of the torus) ; $\tau_{\mathtt{V}}$, the optical depth of the individual clumps ; σ, the torus angular width; and `i`, the inclination angle.

4.6.2 Additional X-ray Components

The emission from AGN is complex and its primary spectrum is not just altered by the structure. Therefore, apart from the emission due to the reprocessing of primary X-ray continuum by the torus, the X-ray spectra of PSS can contain several additional components which are discussed below.

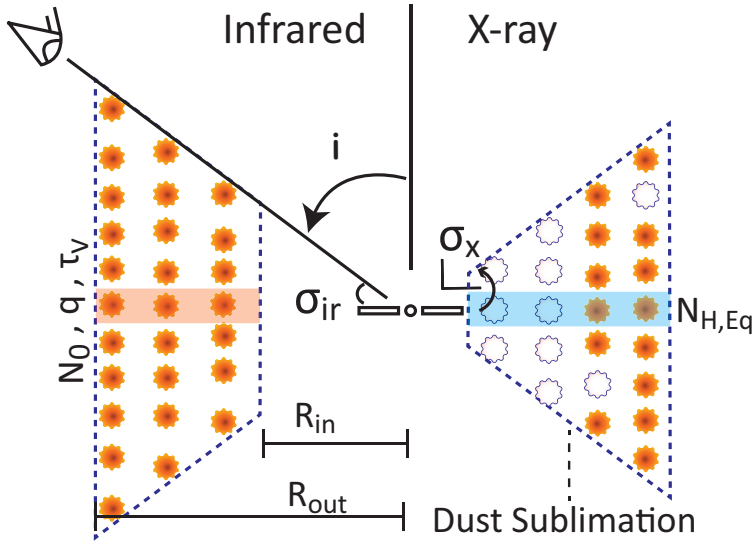

Figure 4.1: The basic clumpy torus geometry from Nenkova et al. (2008b) with the colored clumps denoting dust and the clear clumps denoting gas. The left half shows the infrared whereas the right half shows the X-ray view of the same Clumpy structure and their respective parameters. The shaded region denotes the equatorial plane. The dust sublimation radius beyond which dust can exist is also marked.

4.6.2.1 Soft Excess In many AGN, soft X-ray emission in excess to that of the extrapolated primary X-ray continuum is observed below 2 keV and referred to as 'soft excess' (see e.g. Bianchi et al., 2009; Petrucci et al., 2018). The exact nature of this soft excess unknown but one popular theory associates with Comptonized emission from a warm corona on the surface of the accretion disk (Magdziarz et al., 1998; Petrucci et al., 2013; Ursini et al., 2018). Therefore, if present, we approximate this Comptonized component with a steep powerlaw. If this simple approximation is insufficient, we model it using the publicly available thermal Comptonization model `compTT` (Titarchuk, 1994).

4.6.2.2 Absorption The primary continuum can be absorbed by the line-of-sight dust or gas clouds that are part of the broad line region. To model this ionized absorption, we create a custom photoionized absorption table model using the `xstar` (v2.54 ; Kallman & Bautista, 2001) code to produce a multiplicative tabulated model grid. The model is

calculated assuming the material as fully covering with a typical temperature of 10^6 K, a typical density of $10^{12}\,\mathrm{cm}^{-3}$, an ionizing luminosity of $10^{45}\,\mathrm{ergs\,s}^{-1}$, a turbulent velocity of $100\,\mathrm{km\,s}^{-1}$ and solar abundances. We also assumed a power-law spectrum with the photon index of 2.0 as illuminating flux. The resulting table model has three free parameters: the absorption column, the ionization parameter, and the redshift. Additionally, if a partial covering absorber is required, we use the publicly available `zxipcf` model (Reeves et al., 2008).

4.6.2.3 Emission In addition to absorption emision components can often be found. These can often be associated with photoionized material out of our line-of-sight. To model this emission, we create a custom photoionized emission table model using the `xstar` (v2.54 ; Kallman & Bautista, 2001) code with the same assumptions as in Section 4.6.2.2. However, if the spectra suggest that photoionized emission does not describe the observed emission features, we use the publicly available collisional ionization model `APEC` (Foster et al., 2012).

4.6.2.4 Relativistic reflection If the primary continuum backscatters off the innermost accretion disk, the X-ray spectra can additionally show the presence of a relativistic reflection component, usually causing a relativistically broadened iron line (Fabian et al., 1989; George & Fabian, 1991). If present, we use the publicly available `relxill` (Garcia et al., 2013) model to describe this feature. The `relxill` model assumes that the incident emission is a cut-off powerlaw and that the radial strength of illumination can be described by a broken power-law profile.

In Table 4.3, we show which sources required which additional X-ray components for our sample. The presence of the component is denoted by a check mark, and if more than one instance of the component is present, the number of additional instances are represented by the number of asterisks. Additional components were only included if they significantly

improved the description of the spectra.

Source	**Soft Excess**	**Absorption**	**Emission**	**Relativistic Reflection**
NGC 3227	✓	✓***	×	×
NGC 4593	✓*	✓	✓*	×
Mrk 766	×	✓**	×	✓
Fairall 51	×	✓	×	✓
ESO 323 G77	×	✓*	✓	×
Mrk 1239	×	×	✓	×
Was 45	✓	✓	×	×
Mrk 704	✓	✓**	✓	✓
Mrk 1218	×	✓*	×	×
Mrk 231	×	✓	✓	×
IRAS 15091-2107	×	✓	×	×
Mrk 376	✓	×	×	×

Table 4.3: The Addtional X-ray components list. For each source, the presence of a component is denoted by ✓. If more than one instance of the component is present, each additional instance is marked by *. Absence of a component is noted by a ×.

4.6.3 Additional Infrared Components

The average redshift of the PSS sample is 0.03. In order to resolve the IR emission of the parsec scale torus of these AGN, we need data from next-generation detectors with sub-arcsec angular resolution or better. Our infrared data includes averaged emission up to the kpc scale around the torus. Thus in addition to the torus emission, our infrared SEDs can show the contamination from the AGN polar outflow and features from the host galaxy

which we will need to model.

The nuclear hot dust from the inner regions of the torus can emit in the Near-IR band (Mor et al., 2009). However, this band in low redshift galaxies is dominated by old stellar populations that share nearly identical SEDs that peak at ∼1 micron and drop quickly following a Rayleigh-Jeans tail toward the mid-IR (Lyu & Rieke, 2018). We utilize a stellar emission template calculated by Lyu & Rieke (2018) to model this component.

Studies have shown that the polar dust in the ∼100 pc scale between the torus and the Narrow-line region can have a significant contribution in the mid-IR (Hönig et al., 2012). Fortunately, this polar dust emission at relatively low optical depth ($\tau_V < 5$) peaks at ∼25.6 micron, and has SED shape that stays the same around this wavelength (Lyu & Rieke, 2018). We utilize a polar dust template from Lyu & Rieke (2018) to model this component.

Prominent emission from polycyclic aromatic hydrocarbon (PAH; Puget et al., 1985) due to photodissociation regions illuminated by UV-bright stars can be found in the mid-IR spectra of star-forming galaxies (Smith et al., 2007). These appear as broad emission line features, centered at 3.3, 6.2, 7.7, 8.6, 11.2, and 12.7 microns. Also, the cold dust outside the torus generates continuum emission whose shape is governed by the dust temperature. From the 55 SEDs of star-forming galaxies, Bernhard et al. (2021) built a set of 7 galaxy dust templates assuming a range of dust temperatures (20 K – 45 K) along with a universal PAH template. We utilize this PAH template and one of the galaxy dust templates for each source in our analysis.

4.7 Spectral Modeling

Spectral modeling is carried out in the `XSPEC v12.11.1` software package (Arnaud & A., 1996) using the chi-square minimization unless otherwise stated. The X-ray spectra obtained from the data as described in Section 4.5.1 are already `XSPEC`-compatible. The infrared spectra and photometric data (see Section 4.5.2) are converted to an `XSPEC`-compatible

format using the `flx2xsp` routine. Further, the infrared CLUMPY model SED library and other templates are converted into `XSPEC`-compatible additive table model using `flx2tab` routine. Both `flx2xsp` and `flx2tab` are a part of `FTOOLS`[1].

The X-ray spectra are binned such that the detector resolution is over-sampled by a factor of 3 and enforcing a minimum signal to noise ratio of 5. Only the *Swift* -XRT spectra were binned to a minimum of 20 counts per bin. We use the energy range of 0.7–1.5 keV, 2.4–10.0 keV for *Suzaku*-XIS; 15.0–60.0 keV for *Suzaku*-PIN; 0.3–10.0 keV for *XMM*-PN; 3.0–79.0 keV for *NuSTAR*; 0.2–10.0 keV for *Swift*-XRT.

The *Spitzer* -IRS spectra have much higher resolution than the CLUMPY model grid. Thus, we bin the *Spitzer* spectra to match the wavelength grid of CLUMPY model as the model cannot capture features at higher resolution. This rebinning is performed after manually removing the mid-infrared atomic fine-structure emission lines of galactic origin as their modeling is beyond the scope of this study. This kind of rebinning is not required for the rest of the infrared data.

4.7.1 X-ray modeling

We fit all X-ray data from Table 4.2 for each source using an X-ray model that includes a primary emission component, reprocessing of this primary emission from the AGN central engine by a clumpy torus, and other required X-ray components as described in Section 4.6.2. If the X-ray observations are separated by more than ∼1 day, they are considered to be a different epoch.

Mrk 376 is an exception to this as it has little archival X-ray data and the existing data is of relatively poor quality. Due to this lack of data, we assume the Swift-XRT data that is separated by about 10 days from the rest of the data to be still part of the same epoch as the difference in the spectra is negligible. Since Mrk 376 is not observed by *Spitzer* , we cannot

[1] http://heasarc.gsfc.nasa.gov/ftools

directly model its infrared torus parameters and thus remove it from the infrared and joint analysis done in the subsequent Section 4.7.2 and 4.7.3.

For our modeling, we model the different epochs together, assuming that the primary continuum may change between epochs. The first X-ray spectrum for each source as shown in Table 4.2 is considered the reference spectrum. The detailed X-ray model for each epoch of a source is expressed in the `XSPEC` terminology as follows:

$$\overbrace{\texttt{TBabs}}^{\text{Galactic } N_{\mathrm{H}}} \times \Big(\overbrace{\texttt{zphabs} \times \texttt{cabs} \times \texttt{zcutoffpl} \times \texttt{WA}}^{\text{Absorbed primary component}} + \underbrace{\texttt{atable}\{\texttt{xclumpy\_R.fits}\} + \texttt{atable}\{\texttt{xclumpy\_L.fits}\}}_{\text{Clumpy torus repocessor}} + \underbrace{\texttt{const} \times \texttt{zcutoffpl}}_{\text{Scattered component}} + \underbrace{\texttt{Additional Emission}}_{\text{Additional X-ray Emission Components}} \Big) \quad (4.1)$$

The first component is the galactic absorption component that accounts for the ISM absorption from our galaxy using the ISM absorption model `TBabs` (Wilms et al., 2000) with a fixed column density for each source as obtained from the online $\mathrm{N_H}$ Tool (Collaboration et al., 2016; Kalberla et al., 2005).

The second component is the absorbed primary continuum. For each epoch, we model an X-ray primary continuum using a redshifted cut-off powerlaw (`zcutoffpl`) assuming different photon indexes (Γ) and normalizations, while keeping the cutoff energy fixed at a typical value of $\mathtt{E}_{\mathrm{cut}}$ = 370 keV (Ricci et al., 2018). This primary continuum component is modified by photoelectric absorption and Compton scattering as the line-of-sight passes through the torus. These effects are modeled using the models `zphabs` and `cabs` respectively. The line-of-sight column density through the clumpy torus can be self-consistently determined in XCLUMPY using the equation Tanimoto et al. (2019):

$$N_{\mathrm{H}}^{\mathrm{LOS}} = N_{\mathrm{H}}^{\mathrm{Equ}} \exp\Big(- \frac{(\mathrm{i} - 90^{\circ})^2}{\sigma_{\mathrm{x}}^2} \Big)$$

Throughout our modeling, we assume a fixed torus structure for every source, so the line-of-sight column density is the same across all epochs. We note that there could be possible line-of-sight variations between epochs which is usually tackled using an epoch-variable multiplicative factor. However, we have ignored observations that show high variability and occulation events in our data selection. Also, as we have a warm absorber (`WA`) modifying the primary component in each source as seen in Table 4.3 it would be difficult to also allow for line-of-sight column density variations. Thus, we ignore the possibility mild-variation in the line-of-sight column density.

The third component is the emission from the clumpy torus. It contains two additive tables with `xclumpy_R.fits` and `xclumpy_L.fits` describing the reflection continuum and the fluorescent lines from the torus. Both tables have the same six parameters: $\mathrm{N_H^{Equ}}$,σ_{x},$\mathtt{i}$,Γ,$\mathtt{E}_{\mathrm{cut}}$ and normalization. We link Γ,$\mathtt{E}_{\mathrm{cut}}$ and normalization to the intrinsic continuum of the respective epoch. The other three main torus parameters are linked among all epochs.

The fourth component models the unabsorbed but scattered component, where `const` is the scattering fraction ($\mathtt{f}_{scat}$). We link the `zcutoffpl` parameters to those of the primary continuum.

The fifth component represents the required additional soft excess and/or emission and/or relativistic reflection to get an acceptable fit with reduced chi-squared below 1.25. The additional components added for each source can be found on Table 4.3. We further include a cross correlation constant in our modeling, which accounts for any cross-calibration flux offsets to be 1 for a detector (always *XMM-Newton* PN if present, or else *NuSTAR* FPMA) per epoch, while for others, they are free to vary between 0.9 and 1.1. The only exception is *Suzaku* -PIN, for which it is fixed at 1.16, the expected value for XIS-nominal pointing.

After finding a best fit multi-epoch X-ray model for all sources using the chi-squared

minimization with reduced chi-squared if 1.25 or better, we conduct a robust error analysis using Goodman & Weare's Affine Invariant Markov chain Monte Carlo (MCMC) Ensemble sampler (Foreman-Mackey et al., 2013) implemented in `XSPEC` by Sanders (2018). We generated a chain of total length of 3×10^6 using 300 walkers after burning the previous 6×10^5 steps. Torus parameters obtained for all sources is shown in Figure 4.2. All errors are calculated with a 90% confidence level.

We find that the equatorial column density of the torus for all sources except Mrk 766 to be $> 10^{24}$ cm^{-2} with the sample average of 4.3×10^{24} cm^{-2}. Also, the average torus angular width and inclination of the sample are found to be 35.8° and 34.2° respectively. These values are compatible with the PSS geometry where the line-of-sight is grazing the torus edge.

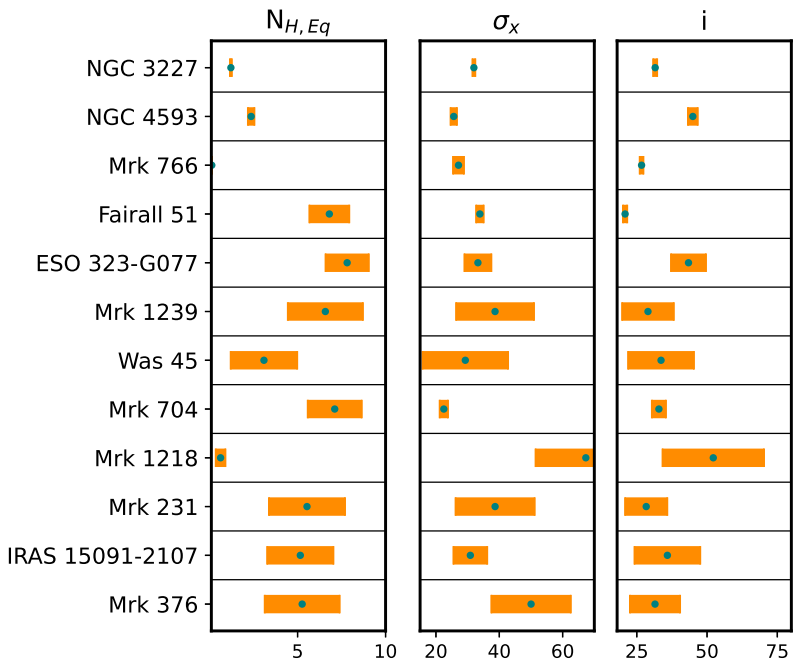

Figure 4.2: The results from the MCMC analysis of the broadband X-ray spectral analysis of our sample. Each column shows the result of the parameter marked on top. The errors are shown at 90% confidence level.

4.7.2 Infrared spectral modeling

We model all infrared data for each source jointly using an IR model that includes a reddened clumpy torus emission with additional IR components to model any flux contamination from other regions as outlined in Section 4.6.3.

We perform the IR SED fitting of the sources using the IR model expressed in the XSPEC terminology as follows:

$$\begin{aligned}\big(\texttt{zdust}_{\text{mw}} \times \texttt{zdust}_{\text{intr.}} \times \texttt{atable}\{\texttt{clumpy.fits}\}\big) + \\ \texttt{atable}\{\texttt{oldstar.fits}\} + \texttt{atable}\{\texttt{galaxy.fits}\} + \\ \texttt{atable}\{\texttt{PAH.fits}\} + \texttt{atable}\{\texttt{Polar.fits}\}\end{aligned} \quad (4.2)$$

Here the $\texttt{zdust}_{\text{mw}}$ models the foreground extinction which is fixed at the estimates from the Galactic dust reddening map from Schlafly & Finkbeiner (2011) ; the $\texttt{zdust}_{\text{intr.}}$ models the intrinsic extinction of the source ; atable{clumpy.fits} is the Clumpy torus model as an XSPEC-compatible additive component; atable{oldstar.fits}, atable{galaxy.fits}, atable{PAH.fits}, and atable{Polar.fits} are the stellar, galaxy dust, PAH, and polar dust emission templates respectively (see Section 4.6.3 for more details on each of them) as an XSPEC-compatible additive model.

We fit all of the infrared data for each source as one SED with all the components from Model 4.2 present. The fit obtained after the χ^2 minimization is used as a starting point for a robust error analysis using Goodman & Weare's Affine Invariant Markov chain Monte Carlo (MCMC) Ensemble sampler (Foreman-Mackey et al., 2013) implemented in XSPEC by Sanders (2018). We generated a chain of total length of 2×10^6 using 100 walkers after burning the previous 5×10^5 steps. Torus parameters obtained for all sources is shown in Figure 4.3. All errors were calculated with a 90% confidence level.

We find that the $\texttt{N}_0$, $\texttt{Y}$, $\texttt{q}$, σ_{ir} and $\tau_{\texttt{V}}$ cover the whole parameter space, and no clear trends

in the sample are seen. Importantly, the inclination (i) of the sample is closer to edge-on in most sources, which is incompatible with the PSS geometry where the line-of-sight is only grazing the torus edge. This means the results from the infrared-only study of the PSS torus are likely problematic. Without external constraints on inclination,degeneracies among the parameters in the SED fitting prevent us from obtaining a clear picture.

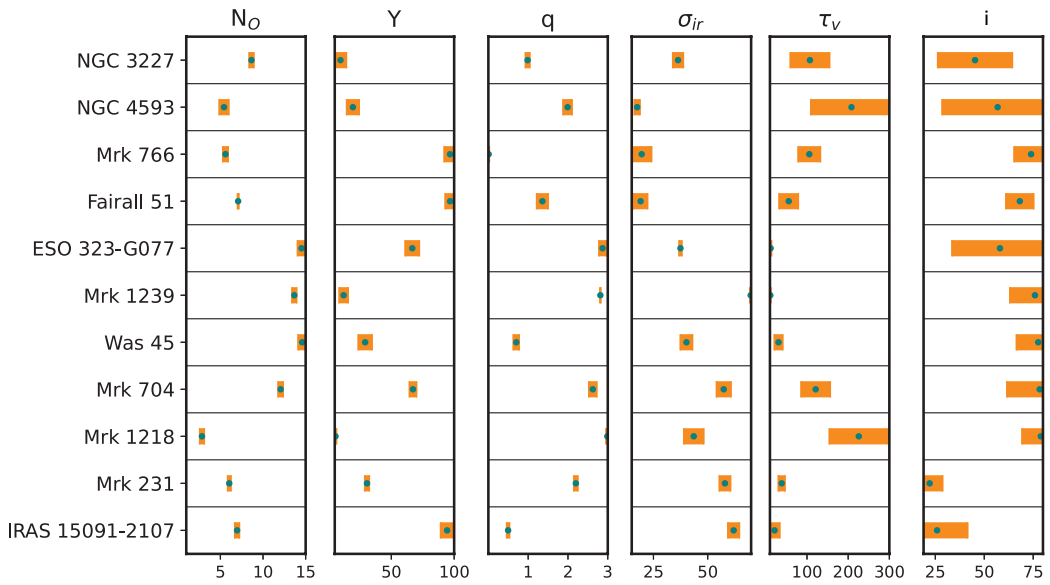

Figure 4.3: The results from the MCMC analysis of the IR SED analysis of our sample. Each column shows the result of the parameter marked on top. The errors are shown at 90% confidence level.

4.7.3 Joint spectral fitting

In section 4.7.1 and 4.7.2, we described the results from separate X-ray and IR modeling of the available data of the PSS sample. We find the standalone X-ray results to be consistent with the expected geometry of the sample, whereas the standalone infrared fit yielded extreme inclinations inconsistent with expectations. In this section, we perform joint X-ray/IR modeling with the aim of obtaining better constraints on the multi-wavelength torus parameters.

There are two common torus parameters shared by both X-ray and IR models: inclination and torus angular width. However, studies have shown that the torus angular widths obtained from the infrared spectra to be systematically larger that those obtained from the X-ray spectra for the same AGN (Ogawa et al., 2021; Tanimoto et al., 2020). Thus, we refrain from linking the torus angular width to investigate this further.

Before we perform a joint multi-wavelength spectral modeling for all sources, we test the method in just Mrk 704 to see if the resulting description is better than the individual fits and this joint modeling is justified. We combine both X-ray and IR spectral models of Mrk 704 as obtained from section 4.7.1 and 4.7.2 into one. This was done by just adding the model 4.1 and 4.2. All initial parameter values are same as their best fit value obtained previously. Next, the infrared inclination was linked to the X-ray inclination, and a new fit was obtained via χ^2 minimization. The fit obtained after the χ^2 minimization is used as a starting point for a robust error analysis using Goodman & Weare's Affine Invariant Markov chain Monte Carlo (MCMC) Ensemble sampler (Foreman-Mackey et al., 2013) implemented in `XSPEC` by Sanders (2018). We generated a chain of total length of 4×10^6 using 400 walkers after burning the previous 4×10^5 steps. Figure 4.4 shows the X-ray (Orange) vs IR (Green) vs Joint (Blue) torus parameters contours (1 σ and 2 σ) of Mrk 704. We can clearly see the new inclination is similar to the more reasonable X-ray value, and most of the infrared torus parameters have shifted to a new value with often a better constraint. Further, the constraints on the X-ray torus parameters also have been mildly improved. Thus, we conclude that the joint multi-wavelength spectral fitting is justified, and perform a similar fit to all remaining sources.

The improved multi-wavelength torus parameters are shown in Figure 4.3. All errors were calculated at a 90% confidence level. The X-ray torus parameters are consistent with the expected geometry of a Polar-scattered Seyfert-1 galaxy with low/moderate σ_x and `i`. Most sources show Compton-thick obscuration ($N_H^{Equ} > 10^{24}$ cm^{-2}) at the torus equator. The

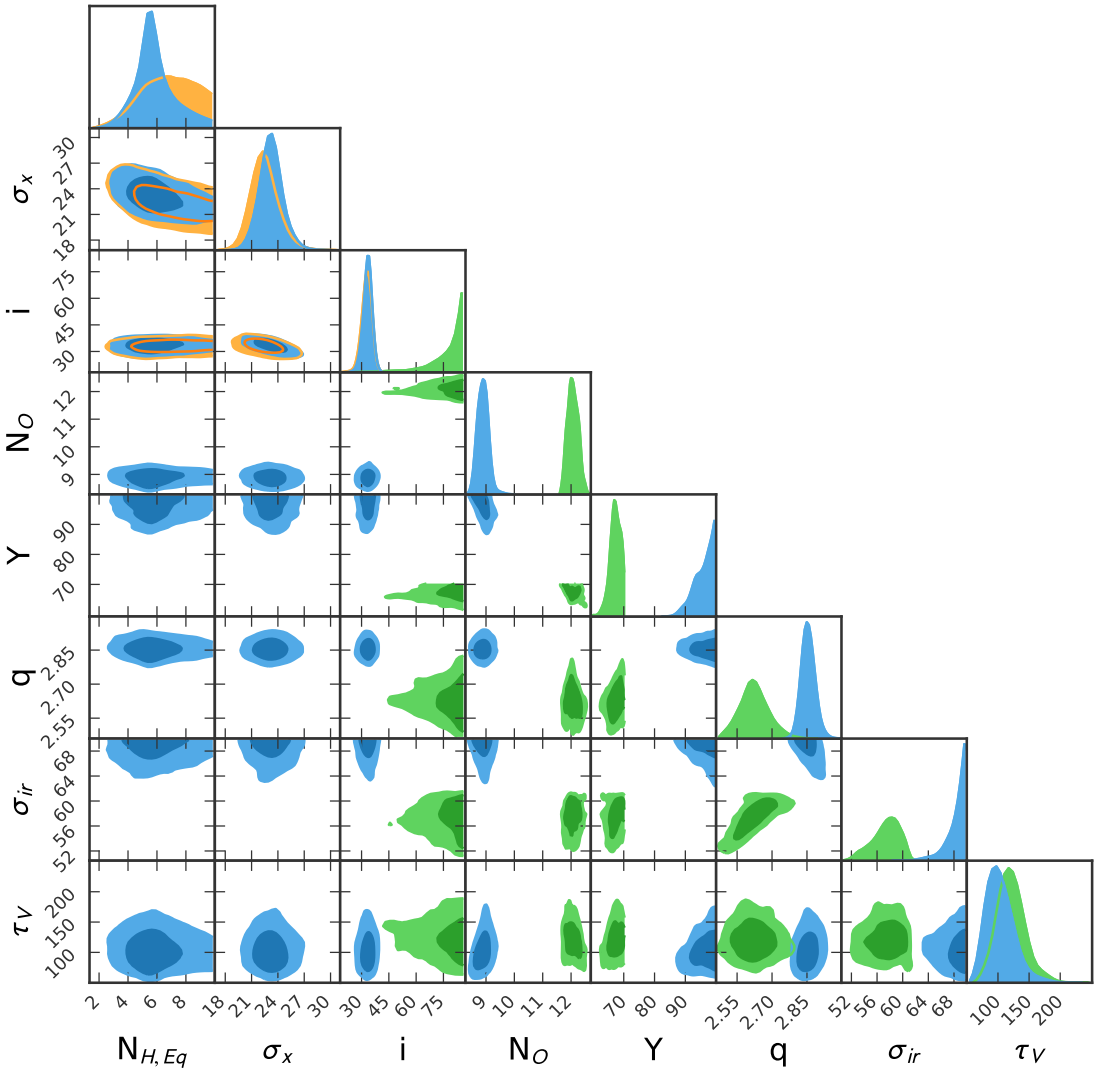

Figure 4.4: The X-ray (Orange) vs IR (Green) vs Joint (Blue) torus parameters contours (1 σ and 2 σ) of Mrk 704.

single cloud optical depth (τ_V) is below 100 for most sources with the average of the sample being 70. The rest of the IR torus parameters of the sample span the whole parameter space. No additional similarities or clear trends are found among the torus parameters.

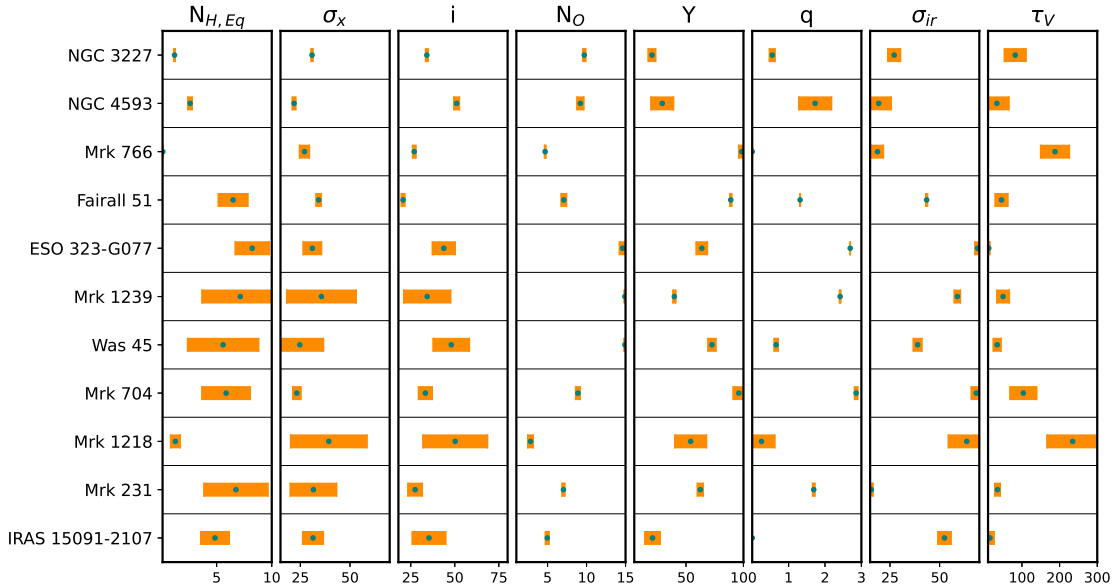

Figure 4.5: The results from the MCMC analysis of the joint X-ray/IR data of our sample. Each column shows the result of the parameter marked on top. The errors are shown at 90% confidence level.

4.8 Results and Discussion

In Section 4.7.3, we presented the joint X-ray/IR spectral modeling results of a sample of Polar-scattered Seyfert 1 galaxies using a multi-wavelength clumpy torus model. Here, we discuss the implications of our findings.

4.8.1 Inferred torus structure from the X-rays and IR

The X-ray and IR study of the clumpy torus measure different components of the total circumnuclear torus. IR traces the dusty component of the torus, whereas X-ray traces both the innermost dusty structure and the dust-free gas located before and beyond the dust sublimation radius, the nearest region where dust can exist. Thus, the torus structure inferred from the X-ray and IR parameters do not necessarily have to agree.

If the distribution of dusty clumps and the gas around the torus edge is similar for all

Seyferts, or at least the PSS sources, we expect the torus angular width inferred from X-rays and IR to correlate with each other in some way. In Figure 4.6, we plot the torus angular width as inferred from X-ray vs IR. We find no clear correlation between them. The σ_x parameter is constrained between 20° and 38 °, whereas the σ_{ir} parameter spans the whole parameter space.

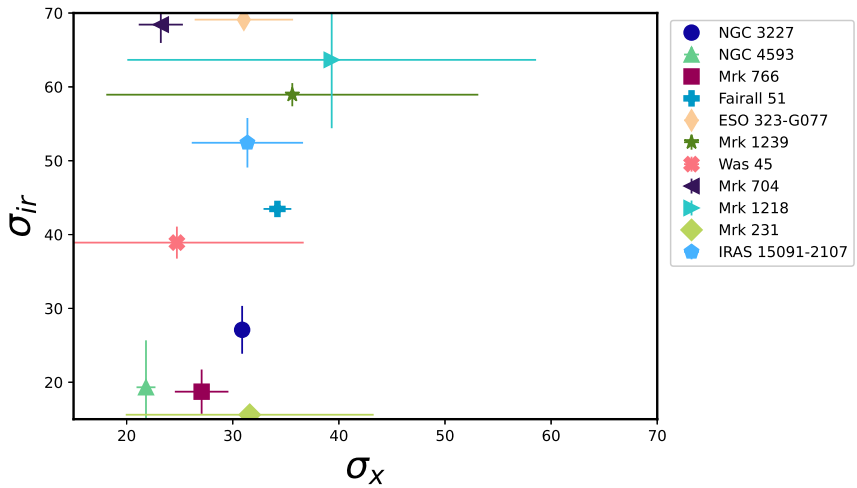

Figure 4.6: The X-ray torus angular width ($\sigma_{\rm x}$) vs the IR torus angular width ($\sigma_{\rm ir}$) from the joint multi-wavelength analysis is plotted. The legend is shown on the right.

Similarly, if the distribution of dusty clumps and the gas in the equatorial plane of the PSS tori is similar, we expect the total hydrogen column density along the equatorial plane ($\mathtt{N_{H,Eq}}$) and the overall optical depth along the torus equatorial plane which simply is the multiplication of total number of clouds and the optical depth of each cloud ($\mathtt{N_0}\times\tau_V$), to correlate with each other. In Figure 4.7, we plot the X-ray column density vs total IR optical depth in the torus equatorial plane. Here too, we find no clear correlation between them.

Both of these findings suggest that the distribution of the gas and dust in the clumpy tori of PSS sources is not the same. However without additional information about the molecular gas distribution of these tori, we can only speculate on the origin of this variation.

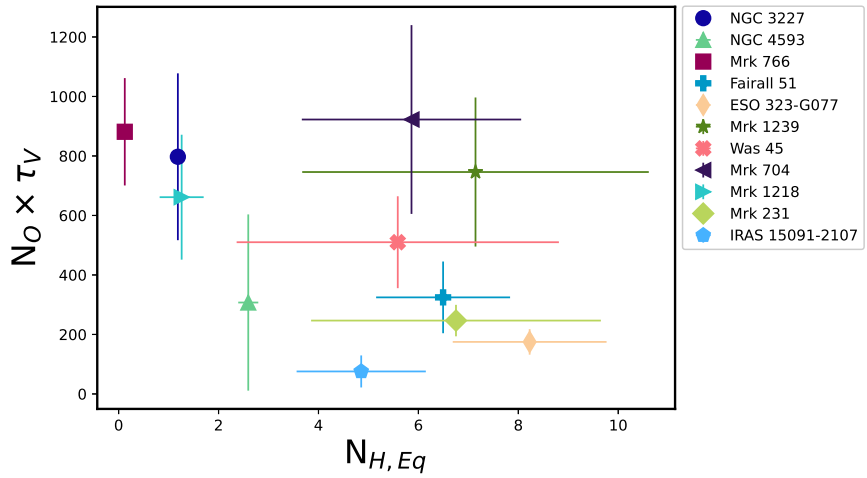

Figure 4.7: The equatorial X-ray column density ($\mathtt{N_{H,Eq}}$) vs total equatorial IR optical depth ($\mathtt{N_0} \times \tau_V$) from the joint multi-wavelength analysis is plotted. The legend is shown on the right.

4.8.2 Torus covering factor versus the Eddington ratio

The fraction of sky covered by obscuring material of the torus around an accreting SMBH is defined as the covering factor. It is considered a key parameter that regulates the AGN feeding and feedback processes García-Bernete et al. (2019); Ramos Almeida et al. (2009). Using a systematic multi-wavelength survey of hard X-ray-selected black holes from the *Swift* -Bat 70-month catalog, Ricci et al. (2017) showed that the covering factor of the Compton-thin obscured sources (10^{22} cm^{-2} $\leq$ N$_{\rm H}$< 10^{24} cm^{-2}) exhibits a sharp decline at an Eddington ratio of $\log \lambda_{\rm Edd} \gtrsim -1.5$. Here, the Eddington ratio is the mass-normalized accretion rate ($\lambda_{\rm Edd}$ = Bolometric Luminosity/Eddington Luminosity). Their results imply that the torus structure of an AGN is mostly driven by the Eddington ratio. This picture is referred to as the radiation-regulated unification model of AGN. We check whether the torus covering factor from our sample is consistent with this model.

The covering factor can be estimated from the `XCLUMPY` torus parameters as (Ogawa

et al., 2021):

$$\text{Covering factor} = \sin\left(\sigma_{\rm x}\sqrt{\ln\left(\frac{\rm N_H^{Equ}}{10^{24}\,{\rm cm}^{-2}}\right)}\right) \tag{4.3}$$

The Eddington luminosity is given by $\rm L_{Edd} = 1.26 \times 10^{38}\ \log M_{BH}(M_\odot)\,erg\,s^{-1}$. Also, the average 2-10 keV luminosity is converted to the bolometric luminosity with a correction factor of 20 (Vasudevan & Fabian, 2007). The ratio of bolometric luminosity to the Eddington luminosity gives us the Eddington ratio, $\log \lambda_{\rm Edd}$.

In Figure 4.8, we plot the Eddington ratio versus the torus covering factor. We notice that even though all of our sources are Compton-thin along the line-of-sight, almost half of the PSS sources do not follow the over-plotted trend from Ricci et al. (2017). This suggests that for significant portion of our sample, even at high Eddington ratio, the radiation pressure does not get high enough to blow away the obscuring material. A similar disagreement with the radiation-regulated unification model at higher Eddington ratio AGN was recently reported by Tanimoto et al. (2022).

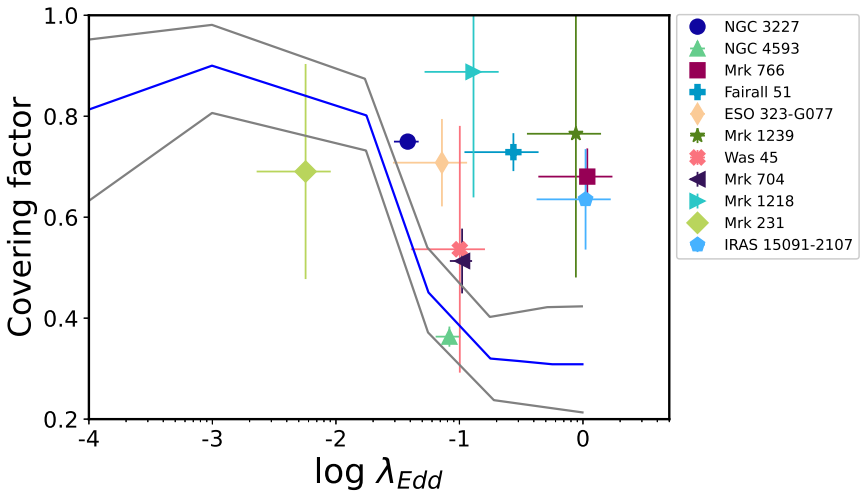

Figure 4.8: The log of Eddington ratio ($\log \lambda_{\rm Edd}$) vs the torus covering factor for the PSS sources from the joint multi-wavelength analysis is plotted. The legend is shown on the right. The relation between for Compton-thin sources obtained by Ricci et al. (2017) is over-plotted.

4.8.3 Distribution of gas in the torus

The Atacama Large Millimeter Array (ALMA) observations in the sub-mm band can probe the molecular gas distribution and kinematics of the torus. The first ALMA detection of AGN torus was for NGC 1068 (García-Burillo et al., 2016). Recently, cold molecular gas within the tori with diameters up to 50 pc in local AGN has been observed and studied (see. Aalto et al., 2019; Alonso-Herrero et al., 2021). In most cases, these tori are connected to reservoirs of molecular gas on scales of $\sim$100 pc (Alonso-Herrero et al., 2021; Combes et al., 2019). Further, these observations have revealed that gas accretion onto SMBHs and their hosts can be regulated via molecular outflows (Lutz et al., 2020). Atacama Large Millimeter Array (ALMA) observations of AGN have been able to detect and study some AGN torus such as NGC 1068 and IC 860 (Aalto et al., 2019; García-Burillo et al., 2016). Using the ALMA observations of one of our PSS source, NGC 3227, Alonso-Herrero et al. (2019) have studied its molecular gas morphology and kinematics in detail. They found nuclear molecular outflow over scales of $\sim$70 pc which appears to have excavated the molecular gas in regions close to the AGN creating a cavity-like structure. A range of molecular gas distributions and outflows has been found by the Galaxy Activity, Torus, and Outflow Survey (GATOS) project (Alonso-Herrero et al., 2021; García-Burillo et al., 2021).

In Section 4.8.1 from our sample of moderately-inclined Seyferts, we find that the torus structure and geometry as inferred from the X-ray and IR do not correlate with each other. This is not expected from the basic torus unification where the only difference between the Seyfert population is the orientation. Further in Section 4.8.2, we find that a significant portion of our sample is not consistent with the radiation-regulated unification model. Both of these results can be explained if the sources within our sample have varied distributions of molecular gas in the torus. For example, if our sources have different densities in the molecular gas of the torus, that would explain the lack of correlation between the X-ray column density and the total IR optical depth. This would also explain the difference in

observed X-ray and IR torus width. If the molecular gas is dense enough, it alone can mark the edge of the X-ray torus width irrespective of the height of the dusty clumps. Also depending on the gas distribution, significant amounts of energy from the radiation pressure can go towards heating the gas thus shielding the dusty structure which in turn can possibly explain the incongruity with the radiation-regulated unification model. However to confirm this, we need a detailed studies of the molecular gas structure and kinematics of these tori.

CHAPTER FIVE

CONCLUSION

There exists a complex interplay between the AGN feeding and feedback. Understanding this interaction between the central engine and its circumnuclear environment is vital in the context of galaxy evolution (Croton, 2006; Menci et al., 2008). My thesis studies this interaction in Compton-thin AGN using their broadband X-ray spectra with the aid of other emission bands whenever appropriate.

In Chapter 2, we study a local Compton-thin broad-line radio galaxy 3C 109. We find it to have a super-Eddington accretion from the SED analysis. However, its X-ray spectra does not show the typical features of super-Eddington accretion such as a strong reflection or a steep power law index. This puts the existing virial SMBH mass estimate of $2 \times 10^8\,M_\odot$ into question. We explore additional ways of estimating the Eddington ratio, some of which we find to be inconsistent with our initial SED estimate. We obtain a new black hole mass estimate of $9.3 \times 10^8 M_\odot$, which brings all Eddington ratio estimates into agreement and does not require 3C 109 to be super-Eddington. Additionally, we constrain the high-energy cutoff of 3C 109 ($E_{cut} = 49^{+7}_{-5}$ keV) for the first time. This low coronal temperature implies the mixing of non-thermal particles, likely related to the jet core, in the hot corona. This jet core, however, rolls over quickly after the radio band and doesn't affect the Optical/UV and X-ray bands. Thus, we conclude that 3C 109 is unlikely to possess a super-Eddington accretion. Future reliable black hole mass estimates using a reverberation mapping study of this source will be able to confirm our results.

In Chapter 3, we study a local Compton-thin Seyfert galaxy Mrk 926. We find that the multi-epoch broadband X-ray spectra of Mrk 926 show a variable soft excess, and distant reflection atop a thermally Comptonized primary continuum. The origin of the soft excess as

a thermally Comptonized emission from a optically-thick warm corona is slightly preferred but a reflection origin is also possible. To make a strong statement about the nature of the soft excess in this source, high quality data covering the 50-100 keV range would be needed. Additionally, using the archival radio data, we find an unresolved optically-thin radio component consistent with an small-scale radio jet. However, to confirm this, we need to resolve this jet with future high spatial resolution radio observations.

In Chapter 4, we study a sample of 12 moderately inclined Compton-thin AGN known as Polar-scattered Seyfert 1 galaxies (PSS). We investigate their torus structure using multi-epoch broadband X-ray spectra along with their infrared spectral/photometric data. We perform a joint multi-wavelength fit, and are able to constrain the various torus parameters. We find the X-ray torus parameters of the sample to be similar and consistent with the expectation from a PSS geometry (moderately inclined with the line-of-sight grazing the torus edge). The infrared torus structure, however, is found to be very diverse. We also find the covering factor, a proxy for the torus vertical extent, of some sources disagree with the radiation-regulated unification scheme. The interplay between AGN central engine and the torus might be more complicated than what the current AGN Unification schemes suggest. Further, our result points towards a complex and varied distribution of gas and dust in the circumnuclear environment of Compton-thin AGN. The study of the structure and kinematics of molecular gas present in their inner pc region using ALMA (Atacama Large Millimeter Array) should help us explore the origin of this gas/dust variation among AGN tori.

This work demonstrates the usefulness of broadband X-ray spectral analysis as a probe of the AGN feeding and feedback process. Future studies can further clarify some of the open questions. With future high spatial resolution radio observation from VLA and ALMA, the radio jet of Mrk 926 could be resolved. Further, next-gen X-ray telescopes with a higher quality hard X-ray (> 40 keV) spectra should be able to distinguish between the two proposed

origins of the soft-excess. The method of multi-wavelength analysis from Chapter 4 can be easily applied to other AGN. Even though the PSS sample size was too small to establish a clear trend among the torus structures, a significant increase in the sample size of the analysis could be able to achieve this. A lot of Seyferts already have archival X-ray and *Spitzer* data, which means this proposal is feasible in an immediate future without the need for a plethora of additional observations. The results of this study will have strong implications in updating the current view of AGN tori.

REFERENCES CITED

Aalto, S., Muller, S., König, S., et al. 2019, A&A, 627, A147, doi: 10.1051/0004-6361/201935480

Allen, S. W., Fabian, A. C., Idesawa, E., et al. 1997, MNRAS, 286, 765, doi: 10.1093/mnras/286.3.765

Alonso-Herrero, A., García-Burillo, S., Pereira-Santaella, M., et al. 2019, A&A, 628, A65, doi: 10.1051/0004-6361/201935431

Alonso-Herrero, A., García-Burillo, S., Hönig, S. F., et al. 2021, A&A, 652, A99, doi: 10.1051/0004-6361/202141219

Antonucci, R. 1993, ARA&A, 31, 473, doi: 10.1146/annurev.aa.31.090193.002353

Antonucci, R. R. J., & Barvainis, R. 1988, ApJL, 325, L21, doi: 10.1086/185101

Antonucci, R. R. J., & Miller, J. S. 1985, ApJ, 297, 621, doi: 10.1086/163559

Arévalo, P., Bauer, F. E., Puccetti, S., et al. 2014, ApJ, 791, 81, doi: 10.1088/0004-637X/791/2/81

Arnaud, & A., K. 1996, Astronomical Data Analysis Software and Systems V, 101, 17. https://ui.adsabs.harvard.edu/abs/1996ASPC..101...17A/abstract

Arnaud, K. A., Branduardi-Raymont, G., Culhane, J. L., et al. 1985, MNRAS, 217, 105, doi: 10.1093/mnras/217.1.105

Avni, Y., & Tananbaum, H. 1982, ApJL, 262, L17, doi: 10.1086/183903

Awaki, H., Koyama, K., Inoue, H., & Halpern, J. P. 1991, PASJ, 43, 195

Ballantyne, D. R. 2007, MPLA, 22, 2397, doi: 10.1142/S0217732307024322

—. 2020, MNRAS, 491, 3553, doi: 10.1093/mnras/stz3294

Ballantyne, D. R., & Xiang, X. 2020, MNRAS, 496, 4255, doi: 10.1093/mnras/staa1866

Ballantyne, D. R., Bollenbacher, J. M., Brenneman, L. W., et al. 2014, ApJ, 794, 62, doi: 10.1088/0004-637X/794/1/62

Baloković, M., Brightman, M., Harrison, F. A., et al. 2018, ApJ, 854, 42, doi: 10.3847/1538-4357/aaa7eb

Beckmann, V., & Shrader, C. R. 2012, Active Galactic Nuclei

Beloborodov, A. M. 1999, ApJL, 510, L123, doi: 10.1086/311810

Bernhard, E., Tadhunter, C., Mullaney, J. R., et al. 2021, MNRAS, 503, 2598, doi: 10.1093/mnras/stab419

Bianchi, S., Guainazzi, M., Matt, G., Fonseca Bonilla, N., & Ponti, G. 2009, A&A, 495, 421, doi: 10.1051/0004-6361:200810620

Bianchi, S., Matt, G., Balestra, I., Guainazzi, M., & Perola, G. C. 2004, A&A, 422, 65, doi: 10.1051/0004-6361:20047128

Blandford, R., Meier, D., & Readhead, A. 2019, ARA&A, 57, 467, doi: 10.1146/annurev-astro-081817-051948

Blandford, R. D., & Königl, A. 1979, ApJ, 232, 34, doi: 10.1086/157262

Blandford, R. D., & Znajek, R. L. 1977, MNRAS, 179, 433, doi: 10.1093/mnras/179.3.433

Buchner, J., Brightman, M., Nandra, K., Nikutta, R., & Bauer, F. E. 2019, A&A, 629, A16, doi: 10.1051/0004-6361/201834771

Cao, X. 2005, ApJL, 631, L101, doi: 10.1086/497397

Cappi, M., Panessa, F., Bassani, L., et al. 2006, A&A, 446, 459, doi: 10.1051/0004-6361:20053893

Chatterjee, R., Marscher, A. P., Jorstad, S. G., et al. 2011, ApJ, 734, 43, doi: 10.1088/0004-637X/734/1/43

Chiaberge, M., & Marconi, A. 2011, MNRAS, 416, 917, doi: 10.1111/j.1365-2966.2011.19079.x

Chini, R., Biermann, P. L., Kreysa, E., & Gemuend, H. P. 1989, A&A, 221, L3

Choi, C.-S., Dotani, T., Chang, H.-Y., & Yi, I. 2002, Journal of Korean Astronomical Society, 35, 1, doi: 10.5303/JKAS.2002.35.1.001

Choi, C.-S., Dotani, T., Yi, I., Fletcher, A., & Kim, C. 2001, Journal of Korean Astronomical Society, 34, 129, doi: 10.5303/JKAS.2001.34.3.129

Churazov, E., Forman, W., Jones, C., & Böhringer, H. 2000, A&A, 356, 788. https://arxiv.org/abs/astro-ph/0002375

Collaboration, H. I., Ben Bekhti, N., Flöer, L., et al. 2016, A&A, 594, A116, doi: 10.1051/0004-6361/201629178

Combes, F., García-Burillo, S., Audibert, A., et al. 2019, A&A, 623, A79, doi: 10.1051/0004-6361/201834560

Croton, D. J. 2006, MNRAS, 369, 1808, doi: 10.1111/j.1365-2966.2006.10429.x

De Rosa, G., Fausnaugh, M. M., Grier, C. J., et al. 2018, ApJ, 866, 133, doi: 10.3847/1538-4357/aadd11

Denney, K. D., Bentz, M. C., Peterson, B. M., et al. 2006, ApJ, 653, 152, doi: 10.1086/508533

Done, C., Davis, S. W., Jin, C., Blaes, O., & Ward, M. 2012, MNRAS, 420, 1848, doi: 10.1111/j.1365-2966.2011.19779.x

Eckart, A., Witzel, A., Biermann, P., et al. 1986, A&A, 168, 17

Ekers, R. D., Fanti, R., & Miley, G. K. 1983, A&A, 120, 297

Elitzur, M., & Ho, L. C. 2009, ApJL, 701, L91, doi: 10.1088/0004-637X/701/2/L91

Evans, P. A., Beardmore, A. P., Page, K. L., et al. 2009, MNRAS, 397, 1177, doi: 10.1111/j.1365-2966.2009.14913.x

Fabian, A. C. 1996, VA, 40, 197, doi: 10.1016/0083-6656(95)00126-3

Fabian, A. C. 1999, PNAS, 96, 4749, doi: 10.1073/pnas.96.9.4749

Fabian, A. C. 2012, ARA&A, 50, 455, doi: 10.1146/annurev-astro-081811-125521

Fabian, A. C., Lohfink, A., Belmont, R., Malzac, J., & Coppi, P. 2017, MNRAS, 467, 2566, doi: 10.1093/mnras/stx221

Fabian, A. C., Lohfink, A., Kara, E., et al. 2015, MNRAS, 451, 4375, doi: 10.1093/mnras/stv1218

Fabian, A. C., Nandra, K., Reynolds, C. S., et al. 1995, MNRAS, 277, L11, doi: 10.1093/mnras/277.1.L11

Fabian, A. C., Rees, M. J., Stella, L., & White, N. E. 1989, MNRAS, 238, 729, doi: 10.1093/mnras/238.3.729

Fanaroff, B. L., & Riley, J. M. 1974, MNRAS, 167, 31P, doi: 10.1093/mnras/167.1.31P

Foreman-Mackey, D., Hogg, D. W., Lang, D., & Goodman, J. 2013, PASP, 125, 306, doi: 10.1086/670067

Foster, A. R., Ji, L., Smith, R. K., & Brickhouse, N. S. 2012, ApJ, 756, 128, doi: 10.1088/0004-637X/756/2/128

Gandhi, P. 2005, AsJPh, 13, 90

Garcia, J., Dauser, T., Reynolds, C. S., et al. 2013, The Astrophysical Journal, 768, 146, doi: 10.1088/0004-637X/768/2/146

Garcia, J., Dauser, T., Lohfink, A., et al. 2014, The Astrophysical Journal, 782, 76, doi: 10.1088/0004-637X/782/2/76

García, J. A., Dauser, T., Steiner, J. F., et al. 2015, ApJL, 808, L37, doi: 10.1088/2041-8205/808/2/L37

García, J. A., Kara, E., Walton, D., et al. 2019, ApJ, 871, 88, doi: 10.3847/1538-4357/aaf739

García-Bernete, I., Ramos Almeida, C., Alonso-Herrero, A., et al. 2019, MNRAS, 486, 4917, doi: 10.1093/mnras/stz1003

García-Burillo, S., Combes, F., Ramos Almeida, C., et al. 2016, ApJL, 823, L12, doi: 10.3847/2041-8205/823/1/L12

García-Burillo, S., Alonso-Herrero, A., Ramos Almeida, C., et al. 2021, A&A, 652, A98, doi: 10.1051/0004-6361/202141075

Gebhardt, K., Bender, R., Bower, G., et al. 2000, ApJL, 539, L13, doi: 10.1086/312840

George, I. M., & Fabian, A. C. 1991, MNRAS, 249, 352, doi: 10.1093/mnras/249.2.352

Ghosh, K. K., & Soundararajaperumal, S. 1992, ApJ, 398, 501, doi: 10.1086/171873

Ghosh, R., Dewangan, G. C., & Raychaudhuri, B. 2016, MNRAS, 456, 554, doi: 10.1093/mnras/stv2682

Giacchè, S., Gilli, R., & Titarchuk, L. 2014, A&A, 562, A44, doi: 10.1051/0004-6361/201321904

Gierliński, M., & Done, C. 2004, MNRAS, 347, 885, doi: 10.1111/j.1365-2966.2004.07266.x

Gierliński, M., Zdziarski, A. A., Poutanen, J., et al. 1999, MNRAS, 309, 496, doi: 10.1046/j.1365-8711.1999.02875.x

Giovannini, G., Feretti, L., Venturi, T., et al. 1994, ApJ, 435, 116, doi: 10.1086/174799

Graham, A. W., & Driver, S. P. 2007, ApJ, 655, 77, doi: 10.1086/509758

Granato, G. L., De Zotti, G., Silva, L., Bressan, A., & Danese, L. 2004, ApJ, 600, 580, doi: 10.1086/379875

Grandi, P., Malaguti, G., & Fiocchi, M. 2006, ApJ, 642, 113, doi: 10.1086/500100

Green, P. J., Schartel, N., Anderson, S. F., et al. 1995, ApJ, 450, 51, doi: 10.1086/176118

Greene, J. E., Ho, L. C., & Ulvestad, J. S. 2006, ApJ, 636, 56, doi: 10.1086/497905

Grupe, D., Komossa, S., Leighly, K. M., & Page, K. L. 2010, ApJL, 187, 64, doi: 10.1088/0067-0049/187/1/64

Haardt, F., & Maraschi, L. 1991, ApJL, 380, L51, doi: 10.1086/186171

Haardt, F., Maraschi, L., & Ghisellini, G. 1994, ApJL, 432, L95, doi: 10.1086/187520

Harrison, F. A., Craig, W. W., Christensen, F. E., et al. 2013, The Astrophysical Journal, 770, 103, doi: 10.1088/0004-637X/770/2/103

Heckman, T. M., & Best, P. N. 2014, ARA&A, 52, 589, doi: 10.1146/annurev-astro-081913-035722

Hickox, R., Parker, J., Smith, S., & Ananna, T. T. 2022, in AAS/High Energy Astrophysics Division, Vol. 54, AAS/High Energy Astrophysics Division, 106.35

Hönig, S. F., Kishimoto, M., Antonucci, R., et al. 2012, ApJ, 755, 149, doi: 10.1088/0004-637X/755/2/149

Ikeda, S., Awaki, H., & Terashima, Y. 2009, ApJ, 692, 608, doi: 10.1088/0004-637X/692/1/608

Jiang, J., Fabian, A. C., Dauser, T., et al. 2019, MNRAS, 489, 3436, doi: 10.1093/mnras/stz2326

Kalberla, P. M. W., Burton, W. B., Hartmann, D., et al. 2005, Astronomy & Astrophysics, 440, 775, doi: 10.1051/0004-6361:20041864

Kallman, T., & Bautista, M. 2001, ApJS, 133, 221, doi: 10.1086/319184

Kamraj, N., Harrison, F. A., Baloković, M., Lohfink, A., & Brightman, M. 2018, ApJ, 866, 124, doi: 10.3847/1538-4357/aadd0d

Kamraj, N., Rivers, E., Harrison, F. A., Brightman, M., & Baloković, M. 2017, ApJ, 843, 89, doi: 10.3847/1538-4357/aa7563

Kara, E., García, J. A., Lohfink, A., et al. 2017, MNRAS, 468, 3489, doi: 10.1093/mnras/stx792

Kataoka, J., Stawarz, Ł., Takahashi, Y., et al. 2011, ApJ, 740, 29, doi: 10.1088/0004-637X/740/1/29

Katgert, P., Katgert-Merkelijn, J. K., Le Poole, R. S., & van der Laan, H. 1973, A&A, 23, 171

Kay, L. E., & Moran, E. C. 1998, PASP, 110, 1003, doi: 10.1086/316224

Kellermann, K. I., Condon, J. J., Kimball, A. E., Perley, R. A., & Ivezić, Ž. 2016, ApJ, 831, 168, doi: 10.3847/0004-637X/831/2/168

King, A. L., Lohfink, A., & Kara, E. 2017, ApJ, 835, 226, doi: 10.3847/1538-4357/835/2/226

Koljonen, K. I. I., Russell, D. M., Fernández-Ontiveros, J. A., et al. 2015, ApJ, 814, 139, doi: 10.1088/0004-637X/814/2/139

Kollatschny, W., Ochmann, M. W., Kaspi, S., et al. 2022, A&A, 657, A122, doi: 10.1051/0004-6361/202142007

Kormendy, J., & Ho, L. C. 2013, ARA&A, 51, 511, doi: 10.1146/annurev-astro-082708-101811

Kormendy, J., & Richstone, D. 1995, ARA&A, 33, 581, doi: 10.1146/annurev.aa.33.090195.003053

Koss, M., Trakhtenbrot, B., Ricci, C., et al. 2017, ApJ, 850, 74, doi: 10.3847/1538-4357/aa8ec9

Laha, S., & Ghosh, R. 2021, ApJ, 915, 93, doi: 10.3847/1538-4357/abfc56

Laha, S., Guainazzi, M., Dewangan, G. C., Chakravorty, S., & Kembhavi, A. K. 2014, MNRAS, 441, 2613, doi: 10.1093/mnras/stu669

Lauer, T. R., Faber, S. M., Richstone, D., et al. 2007, ApJ, 662, 808, doi: 10.1086/518223

Laurent, P., & Titarchuk, L. 2011, ApJ, 727, 34, doi: 10.1088/0004-637X/727/1/34

Lebouteiller, V., Barry, D. J., Goes, C., et al. 2015, ApJS, 218, 21, doi: 10.1088/0067-0049/218/2/21

Lira, P., Videla, L., Wu, Y., et al. 2013, ApJ, 764, 159, doi: 10.1088/0004-637X/764/2/159

Liu, H.-Y., Liu, W.-J., Dong, X.-B., et al. 2019, ApJS, 243, 21, doi: 10.3847/1538-4365/ab298b

Liu, J., Liu, Y., Li, X., et al. 2016, MNRAS, 459, L100, doi: 10.1093/mnrasl/slw042

Liu, Y., & Li, X. 2014, ApJ, 787, 52, doi: 10.1088/0004-637X/787/1/52

Lohfink, A. M., Reynolds, C. S., Jorstad, S. G., et al. 2013, ApJ, 772, 83, doi: 10.1088/0004-637X/772/2/83

Lohfink, A. M., Ogle, P., Tombesi, F., et al. 2015, ApJ, 814, 24, doi: 10.1088/0004-637X/814/1/24

López-Gonzaga, N., Burtscher, L., Tristram, K. R. W., Meisenheimer, K., & Schartmann, M. 2016, A&A, 591, A47, doi: 10.1051/0004-6361/201527590

Lusso, E., Comastri, A., Vignali, C., et al. 2010, A&A, 512, A34, doi: 10.1051/0004-6361/200913298

Lutz, D., Sturm, E., Janssen, A., et al. 2020, A&A, 633, A134, doi: 10.1051/0004-6361/201936803

Lyu, J., & Rieke, G. H. 2018, ApJ, 866, 92, doi: 10.3847/1538-4357/aae075

Magdziarz, P., Blaes, O. M., Zdziarski, A. A., Johnson, W. N., & Smith, D. A. 1998, MNRAS, 301, 179, doi: 10.1046/j.1365-8711.1998.02015.x

Mallick, L., Alston, W. N., Parker, M. L., et al. 2018, MNRAS, 479, 615, doi: 10.1093/mnras/sty1487

Marchesi, S., Ajello, M., Zhao, X., et al. 2019, ApJ, 872, 8, doi: 10.3847/1538-4357/aafbeb

Marconi, A., & Hunt, L. K. 2003, ApJL, 589, L21, doi: 10.1086/375804

Markoff, S., & Nowak, M. A. 2004, ApJ, 609, 972, doi: 10.1086/421099

Markoff, S., Nowak, M. A., & Wilms, J. 2005, ApJ, 635, 1203, doi: 10.1086/497628

Markowitz, A. G., Krumpe, M., & Nikutta, R. 2014, MNRAS, 439, 1403, doi: 10.1093/mnras/stt2492

Marscher, A. P., Jorstad, S. G., Gómez, J.-L., et al. 2002, Natur, 417, 625, doi: 10.1038/nature00772

Matt, G., Perola, G. C., & Piro, L. 1991, A&A, 247, 25

McHardy, I. 2010, in Lecture Notes in Physics, Berlin Springer Verlag, ed. T. Belloni, Vol. 794, 203, doi: 10.1007/978-3-540-76937-8_8

McHardy, I. M., Papadakis, I. E., & Uttley, P. 1999, NuPhS, 69, 509, doi: 10.1016/S0920-5632(98)00272-2

McKaig, J., Ricci, C., Paltani, S., & Satyapal, S. 2022, MNRAS, 512, 2961, doi: 10.1093/mnras/stab3178

McLure, R. J., Jarvis, M. J., Targett, T. A., Dunlop, J. S., & Best, P. N. 2006, MNRAS, 368, 1395, doi: 10.1111/j.1365-2966.2006.10228.x

Meier, D. L. 2012, Black Hole Astrophysics: The Engine Paradigm

Menci, N., Fiore, F., Puccetti, S., & Cavaliere, A. 2008, ApJ, 686, 219, doi: 10.1086/591438

Merloni, A., & Heinz, S. 2013, in Planets, Stars and Stellar Systems. Volume 6: Extragalactic Astronomy and Cosmology, ed. T. D. Oswalt & W. C. Keel, Vol. 6, 503, doi: 10.1007/978-94-007-5609-0_11

Middei, R., Petrucci, P. O., Bianchi, S., et al. 2020, A&A, 640, A99, doi: 10.1051/0004-6361/202038112

Miniutti, G., Ballantyne, D. R., Allen, S. W., Fabian, A. C., & Ross, R. R. 2006, MNRAS, 371, 283, doi: 10.1111/j.1365-2966.2006.10642.x

Miniutti, G., Sanfrutos, M., Beuchert, T., et al. 2014, MNRAS, 437, 1776, doi: 10.1093/mnras/stt2005

Mor, R., Netzer, H., & Elitzur, M. 2009, ApJ, 705, 298, doi: 10.1088/0004-637X/705/1/298

Moran, E. C., Barth, A. J., Kay, L. E., & Filippenko, A. V. 2000, ApJL, 540, L73, doi: 10.1086/312876

Mundell, C. G., Wilson, A. S., Ulvestad, J. S., & Roy, A. L. 2000, ApJ, 529, 816, doi: 10.1086/308318

Nasa High Energy Astrophysics Science Archive Research Center (Heasarc). 2014, HEAsoft: Unified Release of FTOOLS and XANADU, Astrophysics Source Code Library, record ascl:1408.004. http://ascl.net/1408.004

Nenkova, M., Sirocky, M. M., Ivezić, Ž., & Elitzur, M. 2008a, ApJ, 685, 147, doi: 10.1086/590482

Nenkova, M., Sirocky, M. M., Nikutta, R., Ivezić, Ž., & Elitzur, M. 2008b, ApJ, 685, 160, doi: 10.1086/590483

Netzer, H. 2015, ARA&A, 53, 365, doi: 10.1146/annurev-astro-082214-122302

Noda, H., Makishima, K., Nakazawa, K., et al. 2013, PASJ, 65, 4, doi: 10.1093/pasj/65.1.4

Ogawa, S., Ueda, Y., Tanimoto, A., & Yamada, S. 2021, ApJ, 906, 84, doi: 10.3847/1538-4357/abccce

Oh, K., Koss, M., Markwardt, C. B., et al. 2018, ApJS, 235, 4, doi: 10.3847/1538-4365/aaa7fd

Ohta, K., Aoki, K., Kawaguchi, T., & Kiuchi, G. 2007, ApJS, 169, 1, doi: 10.1086/510204

Padovani, P. 2016, A&ARv, 24, 13, doi: 10.1007/s00159-016-0098-6

Padovani, P., Alexander, D. M., Assef, R. J., et al. 2017, A&ARv, 25, 2, doi: 10.1007/s00159-017-0102-9

Panessa, F., Baldi, R. D., Laor, A., et al. 2019, Nature Astronomy, 3, 387, doi: 10.1038/s41550-019-0765-4

Parker, M. L., Wilkins, D. R., Fabian, A. C., et al. 2014, MNRAS, 443, 1723, doi: 10.1093/mnras/stu1246

Petrucci, P. O., Ursini, F., De Rosa, A., et al. 2018, A&A, 611, A59, doi: 10.1051/0004-6361/201731580

Petrucci, P. O., Haardt, F., Maraschi, L., et al. 2001, ApJ, 556, 716, doi: 10.1086/321629

Petrucci, P. O., Paltani, S., Malzac, J., et al. 2013, A&A, 549, A73, doi: 10.1051/0004-6361/201219956

Petrucci, P. O., Gronkiewicz, D., Rozanska, A., et al. 2020, A&A, 634, A85, doi: 10.1051/0004-6361/201937011

Puget, J. L., Leger, A., & Boulanger, F. 1985, A&A, 142, L19

Ramos Almeida, C., Alonso-Herrero, A., Levenson, N. A., et al. 2014, MNRAS, 439, 3847, doi: 10.1093/mnras/stu235

Ramos Almeida, C., & Ricci, C. 2017, NatAs, 1, 679, doi: 10.1038/s41550-017-0232-z

Ramos Almeida, C., Levenson, N. A., Rodríguez Espinosa, J. M., et al. 2009, ApJ, 702, 1127, doi: 10.1088/0004-637X/702/2/1127

Rani, P., & Stalin, C. S. 2018, ApJ, 856, 120, doi: 10.3847/1538-4357/aab356

Reeves, J., Done, C., Pounds, K., et al. 2008, MNRAS, 385, L108, doi: 10.1111/j.1745-3933.2008.00443.x

Reynolds, C. S. 2019, NatAs, 3, 41, doi: 10.1038/s41550-018-0665-z

Reynolds, C. S., & Fabian, A. C. 1995, MNRAS, 273, 1167, doi: 10.1093/mnras/273.4.1167

Ricci, C., Bauer, F. E., Arevalo, P., et al. 2016, ApJ, 820, 5, doi: 10.3847/0004-637X/820/1/5

Ricci, C., Trakhtenbrot, B., Koss, M. J., et al. 2017, Natur, 549, 488, doi: 10.1038/nature23906

Ricci, C., Trakhtenbrot, B., Koss, M. J., et al. 2017, ApJS, 233, 17, doi: 10.3847/1538-4365/aa96ad

Ricci, C., Ho, L. C., Fabian, A. C., et al. 2018, MNRAS, 480, 1819, doi: 10.1093/mnras/sty1879

Richstone, D., Ajhar, E. A., Bender, R., et al. 1998, Natur, 385, A14. https://arxiv.org/abs/astro-ph/9810378

Risaliti, G., & Elvis, M. 2004, in Astrophysics and Space Science Library, Vol. 308, Supermassive Black Holes in the Distant Universe, ed. A. J. Barger, 187, doi: 10.1007/978-1-4020-2471-9_6

Rivers, E., Markowitz, A., & Rothschild, R. 2011, ApJ, 732, 36, doi: 10.1088/0004-637X/732/1/36

Ross, R. R., Fabian, A. C., & Young, A. J. 1999, MNRAS, 306, 461, doi: 10.1046/j.1365-8711.1999.02528.x

Rudy, R. J., Puetter, R. C., & Mazuk, S. 1999, AJ, 118, 666, doi: 10.1086/300980

Sambruna, R. M., Reeves, J. N., Braito, V., et al. 2009, ApJ, 700, 1473, doi: 10.1088/0004-637X/700/2/1473

Sanders, J. 2018, xspec_emcee: XSPEC-friendly interface for the emcee package, Astrophysics Source Code Library, record ascl:1805.016. http://ascl.net/1805.016

Schlafly, E. F., & Finkbeiner, D. P. 2011, ApJ, 737, 103, doi: 10.1088/0004-637X/737/2/103

Schlegel, D. J., Finkbeiner, D. P., & Davis, M. 1998, ApJ, 500, 525, doi: 10.1086/305772

Schmitt, H. R., Donley, J. L., Antonucci, R. R. J., et al. 2003, ApJ, 597, 768, doi: 10.1086/381224

Seth, A. C., van den Bosch, R., Mieske, S., et al. 2014, Natur, 513, 398, doi: 10.1038/nature13762

Shimura, T., & Takahara, F. 1995, ApJ, 445, 780, doi: 10.1086/175740

Sikora, M., Stawarz, Ł., & Lasota, J.-P. 2007, ApJ, 658, 815, doi: 10.1086/511972

Smith, J. D. T., Draine, B. T., Dale, D. A., et al. 2007, ApJ, 656, 770, doi: 10.1086/510549

Smith, J. E., Robinson, A., Alexander, D. M., et al. 2004, MNRAS, 350, 140, doi: 10.1111/j.1365-2966.2004.07610.x

Smith, K. L., Mushotzky, R. F., Koss, M., et al. 2020, MNRAS, 492, 4216, doi: 10.1093/mnras/stz3608

Sobolewska, M. A., & Papadakis, I. E. 2009, MNRAS, 399, 1597, doi: 10.1111/j.1365-2966.2009.15382.x

Tanimoto, A., Ueda, Y., Odaka, H., et al. 2019, ApJ, 877, 95, doi: 10.3847/1538-4357/ab1b20

—. 2020, ApJ, 897, 2, doi: 10.3847/1538-4357/ab96bc

Tanimoto, A., Ueda, Y., Odaka, H., Yamada, S., & Ricci, C. 2022, arXiv, arXiv:2203.13266. https://arxiv.org/abs/2203.13266

Titarchuk, L. 1994, ApJ, 434, 570, doi: 10.1086/174760

Tombesi, F., Cappi, M., Reeves, J. N., & Braito, V. 2012, MNRAS, 422, L1, doi: 10.1111/j.1745-3933.2012.01221.x

Tristram, K. R. W., Meisenheimer, K., Jaffe, W., et al. 2007, A&A, 474, 837, doi: 10.1051/0004-6361:20078369

Trump, J. R., Impey, C. D., Kelly, B. C., et al. 2011, ApJ, 733, 60, doi: 10.1088/0004-637X/733/1/60

Turner, T. J., Reeves, J. N., Braito, V., et al. 2018, MNRAS, 481, 2470, doi: 10.1093/mnras/sty2447

Tyler, L., Page, K., Goad, M., & Osborne, J. 2006, in Astronomical Society of the Pacific Conference Series, Vol. 351, Astronomical Data Analysis Software and Systems XV, ed. C. Gabriel, C. Arviset, D. Ponz, & S. Enrique, 97

Ulvestad, J. S., & Wilson, A. S. 1984, ApJ, 278, 544, doi: 10.1086/161821

Urry, C. 2004, in Astronomical Society of the Pacific Conference Series, Vol. 311, AGN Physics with the Sloan Digital Sky Survey, ed. G. T. Richards & P. B. Hall, 49. https://arxiv.org/abs/astro-ph/0312545

Urry, C. M., & Padovani, P. 1995, PASP, 107, 803, doi: 10.1086/133630

Ursini, F., Petrucci, P. O., Matt, G., et al. 2018, MNRAS, 478, 2663, doi: 10.1093/mnras/sty1258

Vasudevan, R. V., & Fabian, A. C. 2007, MNRAS, 381, 1235, doi: 10.1111/j.1365-2966.2007.12328.x

Walter, R., & Fink, H. H. 1993, A&A, 274, 105

Wang, J.-M., & Zhang, E.-P. 2007, ApJ, 660, 1072, doi: 10.1086/513685

Weaver, K. A., Gelbord, J., & Yaqoob, T. 2001, ApJ, 550, 261, doi: 10.1086/319713

Weaver, K. A., Nousek, J., Yaqoob, T., Hayashida, K., & Murakami, S. 1995, ApJ, 451, 147, doi: 10.1086/176206

Wilms, J., Allen, A., & McCray, R. 2000, The Astrophysical Journal, 542, 914, doi: 10.1086/317016

Winter, L. M., Veilleux, S., McKernan, B., & Kallman, T. R. 2012, ApJ, 745, 107, doi: 10.1088/0004-637X/745/2/107

Wright, E. L., Eisenhardt, P. R. M., Mainzer, A. K., et al. 2010, AJ, 140, 1868, doi: 10.1088/0004-6256/140/6/1868

Yan, C.-S., Lu, Y., Dai, X., & Yu, Q. 2015, ApJ, 809, 117, doi: 10.1088/0004-637X/809/2/117

Zubovas, K., & King, A. 2012, ApJL, 745, L34, doi: 10.1088/2041-8205/745/2/L34

Życki, P. T., Done, C., & Smith, D. A. 1999, MNRAS, 309, 561, doi: 10.1046/j.1365-8711.1999.02885.x